Feasibility studies for triggering on delayed jets with the ATLAS experiment at the LHC

Machbarkeitsstudien eines Triggers für verzögerte Jets mit dem ATLAS-Experiment am LHC
Master thesis by Marcel Patzwahl
Date of submission: July 21, 2023

1. Review: Professor Dr. Joachim Enders
2. Review: Dr. Christian Ohm

Darmstadt

TECHNISCHE UNIVERSITÄT DARMSTADT

Physics Department
Institut für Kernphysik
AG Enders

Acknowledgement

I would like to express my gratitude to my supervisor Dr. Christian Ohm, for being open to work with a student abroad, giving me the opportunity to work together with the Royal Institute of Technology, always listening and providing me with useful insight on many occasions.

I further thank Prof. Dr. Joachim Enders who supported me and made it possible to work together with Dr. Christian Ohm.

I thank B. Sc. Ricardo Gioia Alvarez who supported me with helpful suggestions on how to improve my work.

I would finally like to thank the members of the ATLAS Jet Trigger group with whom I shared many interesting discussions on jet trigger related topics which improved the outcome of this work.

Contents

1. Introduction

The Standard Model of particle physics (SM) is a mathematically elegant theory describing fundamental physics. The predictions made by the SM are consistent with decades of experimental research. Nevertheless, various observations, such as neutrino masses, the existence of dark matter or the baryon asymmetry of the universe, have given rise to a need for physics beyond the SM (BSM). As a result of that, many theories have been developed in order to explain those shortcomings. [1]

Many BSM theories predict new particles, which generically could be produced and observed at particle colliders such as the Large Hadron Collider (LHC). Despite vigorous efforts to find evidence for BSM particles, none have been seen, leading to the development of new ideas and methods. [2]

Of special relevance for the research addressed here, is the prediction of heavy long-lived particles (LLPs). Such LLPs could be produced at the LHC giving rise to a wide range of experimental signatures inside collider experiments, such as CMS [3] and ATLAS [4].

If the LLP does not interact directly with the detector, it can only be identified by its decay products. Within the ATLAS experiment, good sensitivity to such BSM scenarios has been achieved by reconstructing displaced vertices. Reconstructing the origin of the tracks corresponding to the decay products, leads to a displaced vertex. Due to the ATLAS detector properties, this reconstruction is confined to vertices within R $< 300\,$mm of the primary proton-proton (pp) interaction point (IP) [5]. This limits the measurable LLP masses and lifetimes since many decays are expected to occur outside R$=300\,$mm. Therefore, in order to extend the lifetime and mass sensitivity, a different signature will be investigated in this work.

Contrary to the SM particles in the collisions, heavy LLPs are expected to move, due to their mass, with a velocity $v \ll c$. Therefore, decay products of LLPs, will be delayed wwith respect to SM particles, such as protons, originating from the primary IP [2].

As a consequence of such highly displaced decays, tracks from individual hadrons can not be reconstructed. Nonetheless, due to the calorimeter physics, those hadrons will be reconstructed as jets. Using the excellent timing resolution of the ATLAS calorimeters, the delays of the energy deposits can be measured, enabling an identification and separation of these delayed jets [4].

In this work, the performance of the time reconstruction of jets inside the ATLAS detector is studied. Based on the results, an algorithm is developed to select delayed jets based on their reconstructed times. Finally, a new selection rule will be implemented in the ATLAS trigger system, which selects the collisions that are saved for further analysis in real time during data taking.

Chapters 2 to 4 give introductions of the physics dealt with in this work, the ATLAS detector, and its triggering system. Chapter 5 and 6 investigate how the performance of jet-time determination depends on jet kinematics. Chapter 7 describes the changes made to the ATLAS triggering system. Chapter 8 summarizes this work and introduces possible upgrades and further study possibilities.

2. Theoretical motivation of long-lived-particles

This chapter gives an introduction into the fundamental theory of particle physics, building the theoretical base most of the modern collider experiments were built on.

A short description of the Standard Model of particle physics (SM) is given in section 2.1. Section 2.1.1 describes several problems, requiring physics beyond the SM (BSM). A promising theory, proposing solutions to shortcomings of the SM, is discussed in section 2.2. This theory suggests the existence of additional particles, and serves as an example motivation.

2.1. The Standard Model of particle physics

All information about the SM are taken from Refs. [1, 6].

One of the biggest achievements in modern physics is the description of fundamental particles and forces by the Standard Model of particle physics.

The SM is a quantum field theory, describing three of the four fundamental forces, excluding gravity, and classifies all known fundamental particles, also known as elementary particles. Such particles are not composed of any other particles.

The elementary particles can be divided into four different categories according to their intrinsic properties:

- the **quarks**,
- the **leptons**,
- the **force carriers**, also called **gauge bosons**

- and the **Higgs boson**.

Particles with half-integer spin, quarks and leptons, are called *fermions*. Particles with integer spin, the Higgs boson and force carriers, are called *bosons*. The different charges of each particle define how they interact by the fundamental forces. A summary of all SM particles is given in Table 2.1.

Table 2.1.: Collection of all SM particles and their properties.

Type	Particle	Electric Charge [e^-]	Mass	Couplings
Quarks (S = 1/2)	u	2/3	2.3 MeV	E, W, S, G
	d	-1/3	4.8 MeV	
	c	2/3	1.275 GeV	
	s	-1/3	95 MeV	
	t	2/3	173.07 GeV	
	b	-1/3	4.18 GeV	
Leptons (S = 1/2)	e	-1	511 keV	E, W
	μ	-1	105.66 MeV	
	τ	-1	1.777 GeV	
	ν	0	0	W
	ν_μ	0	0	
	ν_τ	0	0	
Bosons (S = 1)	gluon	0	0	S
	photon	0	0	E
	Z boson	0	91.2 GeV	W, G
	W boson	±1	80.4 GeV	
Boson (S = 0)	Higgs	0	126 GeV	Yukawa

The electromagnetic force

The most studied and best understood force is the electromagnetic interaction. Based on the theory of special relativity and the Maxwell equations, quantum electrodynamics was developed, being the first Lorentz invariant quantum field theory (QFT).

All electrically charged particles interact via the electromagnetic force. The photon is the force carrier. As in all QFTs, the interaction strength is defined by the coupling constant.

In case of the electromagnetic interaction, the coupling constant is

$$\alpha_{EM} \approx \frac{1}{137}.$$

The weak force

After decades of observing unexplained decays, the weak interaction was described as part of a single combined force, the *electroweak force*.

The force carriers of the weak interaction are the W-bosons (W^+ and W^-) and the Z-boson. Compared to the other fundamental forces, the weak force has some unique properties:

- It is the only force that can change the flavour of quarks and leptons.
- It violates the parity symmetry and the charge-parity symmetry.
- The force carriers have masses, that can be explained by the Higgs mechanism:

$$M_W = 80.40(3)\,\mathrm{GeV/c^2},$$
$$M_Z = 91.188(2)\,\mathrm{GeV/c^2}.$$

  Because of the masses of the force carriers, particle decays via the weak force are suppressed, creating long lifetimes of the decaying particles.

With a coupling constant of $\alpha_W = 10^{-6}$, the weak force is about 1000 times weaker than the electromagnetic force.

The strong force

A first indicator of the strong force was the atomic nucleus and the question of how it sticks together, since electromagnetic repulsion between the protons suggests the opposite.

The strong force affects particles with color charge. Gluons are the massless and color charged force carriers. As in the case of the weak force, the strong force has very unique properties:

- The force carriers can interact with themselves.

- On short distances, as in the nucleus, the force increases with increasing distance.

With a coupling constant of $\alpha_{QCD} \sim 1$, the strong force has the largest coupling constant.

2.1.1. Shortcomings of the SM

Despite a wide range of different phenomena explained, there are several problems that cannot be explained by the SM. A more detailed motivation for physics beyond the SM is given in Refs. [1, 7, 8]. In the following, three examples are explained in more detail.

Unification of forces

Since the electromagnetic and gravitational forces showed the same underlying mathematical structure, it is a goal to unify the forces into one bigger theory. Studies of the SM at short distances, or high energies, showed that the fundamental forces approach one another in strength, but never actually meet. Some theories trying to solve this problem suggest partners to all of the known particles. Those theories are summarized as Supersymmetry (SUSY). A more detailed explanation is given in section 2.2. By including supersymmetric partners into the calculations, the fundamental forces come together at an energy of approximately $E \approx 2 \times 10^{16}$ GeV [1]. Due to inaccurate values of coupling constants, there was no distinction between the SM model and supersymmetric models in the beginning. With improved data and calculations, it was shown, that supersymmetry leads to a significantly better unification.

The hierarchy problem

Another problem showing the limits of the SM, are loop corrections to the Higgs boson mass in the SM. The calculations result in the theory being undefined, because of diverging integrals. This problem also appears by including new physics. By parameterizing new physics, a correction of order Λ^2/M_h^2 is found, with Λ being the scale of the new physics and M_h the mass of the Higgs boson. This makes the SM an unsatisfactory theory.

Supersymmetry (SUSY) particles could provide a solution. Loop corrections of fermions and bosons have opposite signs for quantum field theories. In the case of SUSY, particles and their supersymmetric partners enter the loop corrections. Since fermions have bosonic and bosons fermionic SUSY partners, the divergent factor Λ^2/M_h^2 is replaced by approximately $g^2(\bar{m}^2 - m^2)/M_h^2$, where $\bar{m}$ is the mass of the SUSY-partner and m the mass of the SM particle. For a small value of $\bar{m}$, there is no hierarchy problem. This suggests SUSY masses below or around 1 TeV.

Dark matter

Many astrophysical phenomena indicate that the SM particles only make up a small fraction of the total mass of the universe. For a star orbiting a galaxy at a radius R, with a total mass M_{tot} within that radius, the velocity v is given by Newton's second law

$$v^2 = \frac{G \cdot M_{tot}}{R}.$$

For large radii, M_{tot} is approximately constant, suggesting a correlation of $v \sim R^{-1/2}$. Observations found a constant velocity at larger radii, suggesting extra mass. Since this mass is not visible, it is referred to as **dark matter**. Measurements of the anisotropy of the cosmic microwave background suggest a mass distribution of 85% dark matter and 15% visible matter [6].

No SM particle matches the properties of dark matter. One particle that could explain dark matter is the lightest SUSY particle (LSP).

2.2. Supersymmetry

As pointed out in section 2.1.1, the SM has certain limitations. A well studied theory proposing solutions to those problems is the suggestion of symmetric partners relating fermions and bosons, called **supersymmetry**. The information summarized in the following are taken from Refs. [9, 10, 11].

A supersymmetric transformation can be expressed by a generating operator Q turning a bosonic state into a fermionic state and vice versa. Such an operator must be an anti-commuting spinor with

$$Q\,|Boson\rangle = |Fermion\rangle\,.$$

Table 2.2.: Chiral supermultiplets of MSSM.

Particles		spin 0	spin 1/2
squarks, quarks	Q	$(\tilde{u}_L \tilde{d}_L)$	$(u_L d_L)$
	$\bar{u}$	$\tilde{u}^*_R$	$u^\dagger_R$
	$\bar{d}$	$\tilde{d}^*_R$	$d^\dagger_R$
sleptons, leptons	L	$(\tilde{\nu} \tilde{e}_L)$	(νe_L)
	$\bar{e}$	$\tilde{e}^*_R$	$e^\dagger_R$
Higgs, higgsino	H_u	$(H^+_u H^0_u)$	$(\tilde{H}^+_u \tilde{H}^0_u)$
	H_d	$(H^0_d H^-_d)$	$(\tilde{H}^0_d \tilde{H}^-_d)$

This transformation indicates that the hermitian conjugate of Q, $Q^\dagger$ is also a symmetric generator. By carrying a spin $S = 1/2$, the fermionic operators Q and $Q^\dagger$, make SUSY a spacetime symmetry.

Single-particle states of SUSY are collected in so-called *supermultiplets*. Members of supermultiplets are called *superpartners*. There are many possible combinations of particles that can create supermultiplets. All of them can be reduced to two types of supermultiplets:

- **chiral** or **matter** or **scalar** supermultiplet and
- **gauge** or **vector** supermultiplet.

Due to differences between left-handed and right-handed parts, fermions can only be members of chiral supermultiplets and hence, the superpartners are scalar spin-0 bosons. The scalar bosons are called **squarks** or **sleptons** where the **s** stands for ”scalar”. Their symbols are equivalent to their partners, just with an added tilde $(\tilde{q}, \tilde{l})$.

As in the case of all bosons, the supersymmetric partner of the Higgs boson ends on **-ino** and is therefore called **higgsino**. All chiral supermultiplet particles are listed in Table 2.2.

The vector bosons of the SM can only be part of the gauge supermultiplets and hence have spin-1/2 superpartners. The superpartners are called gluinos. An overview of all gauge supermultiplet particles is given in Table 2.3.

The previous discussed supermultiplets are the minimal needed supermultiplets to describe known particles and are referred to as MSSM. The most important consequences of MSSM is the fact that all superpartners must have the same mass as the ordinary particles. Since none of them have been observed yet, *supersymmetry must be a broken symmetry*.

Table 2.3.: Gauge supermultiplets of MSSM.

Particles	spin 1	spin 1/2
gluino, gluon	$\tilde{g}$	g
winos, W boson	$\tilde{W}^{\pm}$ $\tilde{W}^{0}$	$W^{\pm}$ W^{0}
binos, B boson	$\tilde{B}^{0}$	B^{0}

From a mathematical perspective, there are terms that could possibly be included in the mathematical description of MSSM. They aren't included, since they violate the conservation of baryon number (B) or total lepton number (L). This would allow decays such as the decay of a proton by

$$p^{+} \to e^{+}\pi^{0}, \mu^{+}\pi^{0}, \bar{\nu}\pi^{+}, \bar{\nu}K^{+}.$$

Since proton decays haven't been observed yet, a new symmetry is added to the MSSM, eliminating the possibility of L or B violating terms. This parity is called **R-parity** or **matter parity**. For each particle, it can be defined as

$$P_R = (-1)^{3(B-L)+2s},$$

where s is the spin of the particle.

All SM particles, including the Higgs boson, have positive R-parity ($P_R = +1$), all squarks, sleptons, gauginos and higgsinos have negative R-parity ($P_R = -1$). The particles with negative R-parity are often referred to as **supersymmetric particles** or **sparticles**. The introduction of R-parity has three important consequences:

1. The LSP must be stable. If electrically uncharged, it only interacts via weak interaction with matter and would therefore be a good candidate for dark matter (2.1.1). Such a particle would be called **neutralino**.
2. Each sparticle must decay into a state containing an odd number of LSPs (mostly one).
3. Colliders can only produce an even number of sparticles (mostly two).

2.2.1. Split-supersymmetry

Main sources of the following section are Refs. [12, 13].

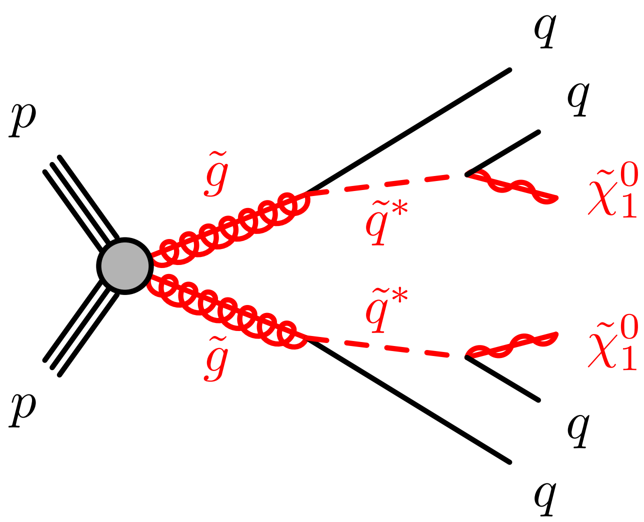

Figure 2.1.: Decay of long-lived gluinos into two quarks and a neutralino.

Split-supersymmetry is a specific case of SUSY, suggesting a supersymmetry-breaking at very high scales ($\Lambda \gg 1000\,\text{TeV}$). All scalar particles, except the Higgs boson, have masses at this high scale. Fermions keep weak-scale masses similar to the Higgs boson. This special case provides useful solutions to several problems:

- The weak-scale fermions preserve gauge coupling unification.
- The lightest neutralino provides a good dark matter candidate.
- The proton decay being suppressed is in agreement with observations.

Another interesting feature of split supersymmetry is the long lifetime of the gluino. Every possible decay of the gluino includes a virtual squark. The large squark mass suppresses the decay, implying a long gluino lifetime. The lifetime is approximately given by

$$\tau \simeq 8 \left(\frac{\Lambda}{10^9\,\text{GeV}} \right)^4 \left(\frac{1\,\text{TeV}}{m_{\tilde{g}}} \right)^5 s,$$

where $m_{\tilde{g}}$ is the gluino mass. With a mass scale of $\Lambda \approx 10^7\,\text{GeV}$ the gluino lifetime can vary between picoseconds up to $\sim 100\,\text{s}$ [14]. Due to the long lifetimes, the gluino will hadronize, forming a so called R-hadron. A possible decay of gluinos is shown in Figure 2.1. Since only even numbers of gluinos can be produced in collider experiments, two gluinos are created in this example. The gluinos will decay into a squark and a quark. The former will further decay into a quark and the lightest neutralino $\tilde{\chi}_1^0$.

3. Large Hadron Collider and the ATLAS detector

This chapter gives an overview of the experimental facilities and methods relevant for this work. The main sources of this section are Refs. [1, 4, 6].

3.1. Introduction to accelerators

The search for new particles and new physics pushed experiments to constantly increasing energies. There are two different types of accelerators:

- Colliders, with two beams of particles being accelerated and colliding head on, and
- Fixed-target colliders, colliding an accelerated particle beam with a fixed target.

Due to the kinetic energy of two moving particles, colliders can typically reach higher collision energies than fixed target colliders. Therefore, many modern accelerators, such as the LHC, are colliders. To increase the probability of a collision, particles are accelerated in groups, called bunches.

A typical way to express the energy in a collider experiment is by using the center of mass (CoM) frame and the corresponding CoM energy, defined by

$$E_{CoM} = \sqrt{s},$$

where s is the Mandelstam variable.

The efficiency and performance of a collider can be measured by a quantity called *luminosity*. The *instantaneous luminosity* quantifies the collision rate at a certain point in time. For N_b Gaussian shaped bunches, with a transverse width defined by σ_x and σ_y, colliding at a frequency ν, containing N_1 and N_2 particles, the instantaneous luminosity is given by

$$\mathcal{L} = \nu \frac{N_1 N_2 N_b}{4\pi\sigma_x\sigma_y}.$$

A better understanding of luminosity can be gained by connecting the luminosity to the expected number of events N of a process with cross section σ:

$$N = \sigma \cdot L,$$

where L is the *total luminosity*, also called *integrated luminosity*, given by the time integral of the instantaneous luminosity

$$L = \int \mathcal{L} dt.$$

3.2. Large Hadron Collider

The largest facility of experimental particle physics is the Large Hadron Collider (LHC) situated in Geneva in Switzerland. It was built by the European Organization of Nuclear research, CERN. It has been operated in multiple runs since 2008, and is planned to run until 2040.

With $26.7\,\mathrm{km}$ in length, the LHC is the largest two-ring-superconducting accelerator and collider of the CERN accelerator complex and the world. By accelerating bunches of protons in both directions, proton collisions occur every $25\,\mathrm{ns}$. During run 2 (2015 - 2018), it was operated at a center-of-mass energy of $\sqrt{s} = 13\,\mathrm{TeV}$ and produced an integrated luminosity of $L \approx 140\,\mathrm{fb}^{-1}$ [15]. For run 3 (from 2022), the center-of-mass energy was upgraded to $\sqrt{s} = 13.6\,\mathrm{TeV}$.

Along its circumference, four collision points are implemented, where the beams share a common pipe [16]. Particle detectors are built around those collisions points, such as CMS (**C**ompact **M**uon **S**olenoid) [3] or ATLAS (**A T**oroidal **L**HC **A**pparatu**S**) [4]. A more detailed description can be found in Ref. [17].

3.3. ATLAS detector

Consisting out of multiple subdetectors, the ATLAS detector is one of the most complex detectors in particle physics. The conceptual layout of the detector is shown in Figure 3.1. It was built to search for SM particles by probing p-p and A-A collisions. With an overall length of $44\,\mathrm{m}$, a radius of $25\,\mathrm{m}$ and a weight of about $7000\,\mathrm{t}$, the ATLAS detector is bigger, but lighter, than the detector of the CMS experiment.

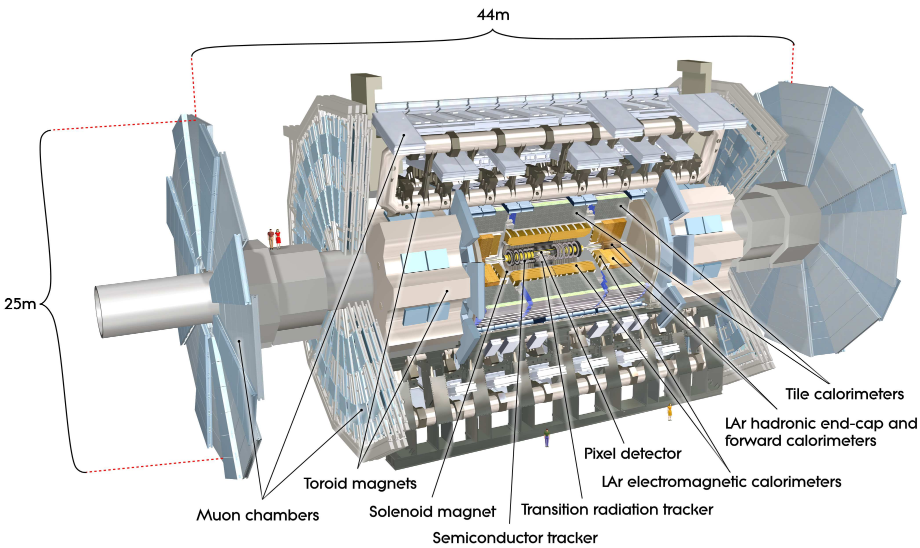

Figure 3.1.: ATLAS detector at CERN. Pixel detector, Semiconductor tracker and Transition radiation tracker build the inner tracking detector, embedded into the magnetic field created by the solenoid magnet. The LAr electromagnetic calorimeters surround the inner detectors, followed by the hadronic calorimeter (Tile calorimeters and the LAr hadronic end-caps). The outermost part are muon chambers placed inside the magnetic field of the toroid magnets [4].

Its subdetectors are placed symmetrically around the beam pipe. The innermost detector is the inner tracking detector, followed by calorimeters. The calorimeters are made of two different subcalorimeters, with the electromagnetic calorimeter being closer to the beam pipe than the hadronic calorimeter. The muon tracker is the outermost subdetector and surrounds the other parts. The magnetic fields used in the inner tracking detector and the muon tracker are created by a complex magnetic system. With this variety of detectors, the ATLAS detector is able to measure and identify nearly all types of SM particles. A more detailed description is given in the article ”The ATLAS Experiment at the CERN Large Hadron Collider” [4].

3.3.1. Coordinate system

ATLAS is approximately cylindrical and symmetric around the beam axis. Therefore, cylindrical coordinates are used to specify positions and express vectors. For ATLAS, the most commonmly used coordinates are:

- The azimuthal angle ϕ, which is the angle around the beam axis.
- The z-axis, defined along the beam pipe.
- The pseudo rapidity η, being related to the polar angle θ, is a measure for the angle between the transverse direction $\hat{p_z}$ and the z-axis. The pseudo rapidity η is defined as:

  $$\eta = -\ln\left(\tan\left(\frac{\theta}{2}\right)\right).$$

  An illustration is given in Figure 3.2. Along the z-axis, the pseudo rapidity reaches the value $\pm\infty$ and 0 along $p_\perp$. For massless particles, the pseudo rapidity is an approximation of the rapidity y itself, which is defined as

  $$y = \frac{1}{2}\ln\left(\frac{E+p_z}{E-p_z}\right),$$

  where E is the energy of the particle and p_z the momentum along the z-axis.
- The transverse momentum $p_\perp$, which describes the momentum orthogonal to the beam direction $\hat{z}$ and is therefore given by

  $$p_\perp = \sqrt{p_x^2 + p_y^2}.$$

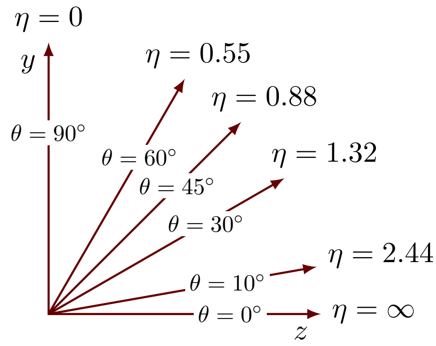

Figure 3.2.: Relation between pseudo rapiditiy η and polar angle θ. It varies between $\pm\infty$ and 0 on a range of $90°$.

3.3.2. Inner tracking detector

Placed in a $2\,\mathrm{T}$ solenoidal field, the inner tracking detector forms the first layers of the ATLAS detector. The inner part of the volume consists out of high-resolution semiconductor pixel and strip detectors, while straw-tube tracking detectors fill the outer part.

When hit by an electrically charged particle, the detector materials will be ionized and produce a measurable signal. Electrically uncharged particles, such as neutrons, will not interact with the detector, leaving no signal. Using the high granularity of the detector, trajectories and vertices can be reconstructed, enabling a direct determination and categorization into charged particles. In combination with the magnetic field, it is possible to gain information about the transverse momentum p_T, by measuring the curvature of the trajectory. The relation between the radius of curvature of the the path R, the magnetic field B and the electric charge of the particle is given by

$$R \simeq 3 \frac{p_T(GeV)}{Q|\vec{B}|(T)}.$$

Due to an increasing uncertainty, the curvature measurement gets more challenging with increasing p_T.

This detector choice enables excellent momentum resolution, pattern recognition and primary and secondary vertex measurements for charged particles within $|\eta| < 2.5$ $(\theta = 10°)$ and with a transverse momentum of $0.5\,\mathrm{GeV} > p_T$.

3.3.3. Calorimeters

Covering a total range of $|\eta| < 4.9$, two types of calorimeters, an electromagnetic and a hadronic calorimeter, are installed. They are designed to stop particles by having them lose all of their energy in the individual cells of the calorimeters. By arranging the detector cells into towers, segmented in ϕ and η, the direction of particles can be measured.

Electromagnetic calorimetry

Electromagnetic (EM) high-granularity liquid-argon (LAr) calorimeters together with lead sheds with high stopping power, cover a region of $|\eta| < 3.2$, with a central barrel ($|\eta| < 1.475$) and two end-caps ($1.375 < |\eta| < 3.2$). With excellent energy and position resolution, they are ideally suited for precision measurements of electrons and photons.

Hadronic calorimetry

The hadronic calorimeter is based on the same basic principles as the electromagnetic calorimeter, but instead of losing the energy by electromagnetic interactions, particles lose their energy through collisions with atomic nuclei. The collision rate can be characterized by the nuclear interaction length λ_I. Because of its small interaction length, iron plates are used as stopping material. With a depth of $7\lambda_I$, the hadronic calorimeter captures nearly all energy of hadrons.

The hadronic calorimeter is divided into multiple parts, covering different regions of the total range. Covering the central directly outside the EM calorimeter, a sampling calorimeter, with scintillating tiles as active and lead as the absorber material, is installed. It divides into a central barrel covering $|\eta| < 1.0$ and extension barrels covering $0.8 < |\eta| < 1.7$. Azimuthally, the barrels are divided into 64 modules, extending from radius $r = 2.28\,\mathrm{m}$ to $r = 4.25\,\mathrm{m}$.

The Hadronic End-cap Calorimeters (HEC) are made of the same detector material as the EM calorimeter, namely liquid-argon. With the intention of creating a better density transition between tile calorimeter and end-caps, the HECs cover a range of $1.5 \leq |\eta| \leq 3.2$, while the tile calorimeter ends at $|\eta| = 1.7$, creating a slight overlap.

3.3.4. Muon Spectrometer

Besides having the same quantum numbers as electrons, muons are 200 times heavier and will therefore not be stopped in the calorimeters. Thus, a muon detection system is built outside the calorimeters. Based on the same concept as the inner tracking detector, the muon tracking system uses a magnetic field perpendicular to the inner magnetic field to deflect muons. This enables the measurement of the 3-D momentum.

High precision tracking chambers are used to measure the curvature of the particle trajectories. Despite the huge dimensions, most muons are not stopped and will leave ATLAS.

3.3.5. Magnet system

The magnetic fields in ATLAS are produced by a hybrid system of four large superconducting magnets. The whole structure has a diameter of $22\,\mathrm{m}$, is $26\,\mathrm{m}$ in length and splits up into two main parts:

- A solenoid, aligned to the beam axis, providing a $2\,\mathrm{T}$ axial magnetic field for the inner detector.
- A barrel toroid and two end-cap magnets creating the magnetic field of the muon detector. The electromagnetic field splits up into three areas. For $|\eta| < 1.4$, magnetic bending is provided by the large superconducting air-core toroid magnets. Over the range $1.6 < |\eta| < 2.7$, the magnetic field is created by the two smaller end-cap magnets. Between $|\eta| = 1.4$ and $|\eta| = 1.6$, the magnetic field is an overlap between the different magnetic fields.

3.4. ATLAS trigger and data acquisition system

The ATLAS trigger and data acquisition (TDAQ) system is responsible for multiple tasks within the data readout of the ATLAS detector, such as:

- online processing of events,
- selection of events, and
- storing events of interest for offline analysis.

The TDAQ system can be split up into a hardware based Level-1 (L1) Trigger and a software based High-Level Trigger (HLT). A more detailed description is given in [18].

3.4.1. Level-1 Trigger

The L1 Trigger consists of custom electronics, designed to trigger on information coming from the calorimeters and the muon detectors. Typically, it is differentiated between the subsystems analyzing calorimeter data (L1Calo), the electronics detecting muons (L1Muon) and the decision-making Central Trigger Processor (CTP). A schematic representation is given in Figure 3.3.

- **L1Calo:** The L1 Calorimeter Trigger uses calorimeter signals as input. The analog input signals are first digitized, calibrated by a preprocessor and then fed into the Cluster Processor (CP) and the Jet/Energy-sum Processor (JEP). The identification of electrons, photons and τ-leptons is handled by the CP, jet candidates are identified by the JEP. In addition, the JEP produces a global sum of total and missing transverse energy.

  Another challenge tackled by a dedicated correction algorithm within the L1Calo is out-of-time pile-up, since the LAr calorimeter signals span over multiple bunch crossings.

- **L1Muon:** By using hits from the Resistive Plate Chambers (RPCs) in the barrel and the Thin Gap Chambers (TGCs) in the endcaps, the L1 muon trigger looks for hit patters consistent with muons with a transverse momentum of several GeV or more. Coincidence requirements are used to reduce background created by particles not originating from the interaction point.

- **Central Trigger Processor:** The CTP is responsible for forming L1-Trigger decisions based on information provided by the L1Calo trigger, the L1Muon trigger, the L1 topological (L1Topo) trigger. L1Topo applies topological requirements on L1Muon and L1Calo objects and other subsystems. In addition, the CTP applies deadtime. Deadtime is used to limit the number of L1 accepts to match the capabilities of the readout electronics. Two different types of deadtime are applied:

  - *Simple deadtime*: Minimum time between two accepted events of the L1-Trigger. The Run 2 setting of 4 bunch crossings lead to an inefficiency of approximately 1% for a L1 rate of $90\,\mathrm{kHz}$.

- *Complex deadtime*: Maximum number of L1 accepted events within a certain amount of bunch crossings. Applied via different leaky bucket algorithms, the Run 2 settings lead to an additional inefficiency of 1% for a L1 rate of $90kHz$.

The L1 Trigger can accept events based on the event-level-quantities (total energy of calorimeter), the multiplicity of objects (transverse momentum of muons) or topological requirements (invariant mass, angular distances). In addition, Regions-of-Interest (RoIs) are identified based on those quantities and objects, used by the HLT. The Level 1 Trigger reduces the LHC event rate from 40 MHz down to approximately 100 kHz.

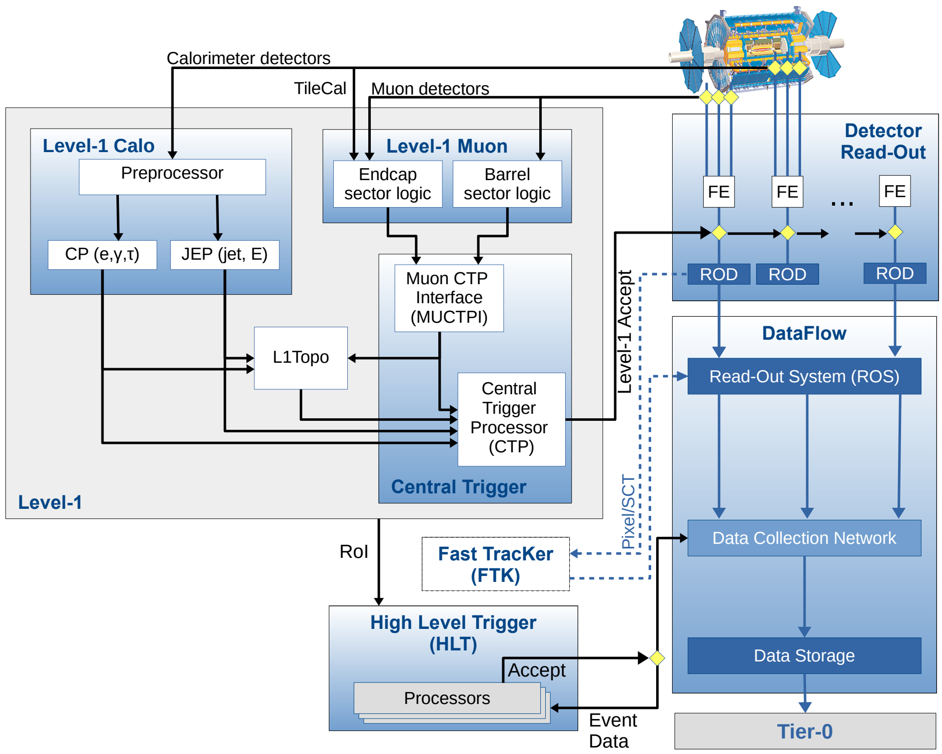

Figure 3.3.: Relevant components for triggering and read-out electronics of the ATLAS TDAQ system in Run 2. Fast TracKer wasn't included in the triggering process [18].

For L1 accepted events, the event data is read out by Front-End (FE) detector electronics, sent to ReadOut Drivers (RODs), from the RODs forwarded to the ReadOut system (ROS) and, in a last step, sent to the second stage High-Level Trigger, if requested.

3.4.2. High-Level Trigger

As for the L1 trigger, the software-based HLT is limited by the electronics and CPU available. Thus, typically fast algorithms for early rejection are applied first, followed by CPU intensive algorithms, based on the offline software Athena [19], for final decisions. Processing units (PUs) in large computing farms (40000 PUs), are used to execute the selection algorithms. Based on the RoIs determined by the L1 Trigger, the PUs request event information. Using the reconstructed features, a hypothesis algorithm decides whether to keep the event or reject it.

HLT accepted events are stored permanently for offline reconstruction and analysis. The out-take of the HLT is on average $1.2\,\mathrm{kHz}$, which corresponds to approximately $1.2\,\mathrm{GB/s}$.

3.4.3. Trigger menu

A L1 item and a series of HLT algorithms form a *trigger chain*, used to select events. The decision is based on kinematic selections applied to reconstructed physics objects. Each chain is designed to target a specific physics signature, such as photons, missing transverse momentum, or jets. The entirety of all *trigger chains* is called trigger menu. By applying prescales $n \geq 1$ to a a chain at L1 or HLT level, the probability of event accepts can be lowered by $\frac{1}{n}$. This allows controlling the rate of accepted events and, thus, making optimal use of L1 and HLT resources.

Driven by physics priorities, the trigger menu configuration covers a broad range of signatures. Due to significantly different signatures compared to pp-collisions, heavy ion collisions have an own trigger menu. The trigger menus are designed based on the expected luminosity. Looser selections can be used during low luminosity running periods.

This section summarizes different, for this work relevant, parts of the ATLAS software. Most information is taken from [4, 18, 20].

3.5. Jet reconstruction

The high lateral granularity of the calorimeters provides enough information to reconstruct jets. In ATLAS, two different algorithms can be used to reconstruct jets. Due to better performance, only a successive recombination algorithm, useful for a wide range of inputs, is used. To identify jet, a spatial measure is used. This measure is given by the distance parameter

$$\Delta R = \sqrt{\Delta\eta^2 + \Delta\phi^2}.$$

The threshold on the distance parameter is $\Delta R = 0.4$ for narrow jets and $\Delta R = 0.6$ for wide jets. For jets kinematics, a complete four-momentum reconstruction is used. At the ATLAS experiment, the anti-k_t algorithm is used to reconstruct jets. A detailed description is given in Ref. [21].

3.5.1. Input to jet reconstruction

In the case of calorimeter jets, two different signals from the calorimeters are used for jet identification by the algorithms:

- **Towers:**
  The cells of the calorimeters are summed up into towers of a $\Delta\eta \times \Delta\phi = 0.1 \times 0.1$ grid. The tower signal is the sum of all individual cell signals. It should be noted, that all cells in a tower are used, independent of their signal strength. Towers with a negative signal strength are dominated by noise and not of use. Thus, they are combined with positive towers around until they create a group with a positive overall signal. This method can be understood as noise cancellation. The results can be used in jet selections.

- **Topological cell clusters:**
  Topological cell clustering is the attempt of a three-dimensional energy deposition reconstruction. To be seen as a seed cell, the measured cell energy E_{cell} has to pass the threshold

  $$|E_{\text{cell}}| > 4\sigma_{\text{cell}},$$

  where σ_{cell} is a measure of the noise distribution inside each cell. In a next step, all nearest neighbors are summed up to a cluster. If this cluster passes a second level threshold

  $$|E_{\text{cluster}}| > 2\sigma_{\text{cluster}},$$

  they are seen as secondary seeds and also the direct neighbors of the cluster are included. By weighting the cell times t_{cell} of all cells assigned to a cluster, with the square of the corresponding E_{cell} and the geometric cell properties $w^{\text{geo}}_{\text{cell},i}$, the cluster time is given by [22]

$$t_{\text{cluster}} = \frac{\sum_i^{N_{\text{cell}}} \left(w^{\text{geo}}_{\text{cell},i} E_{\text{cell},i}\right)^2 t_{\text{cell},i}}{\sum_i^{N_{\text{cell}}} \left(w^{\text{geo}}_{\text{cell},i} E_{\text{cell},i}\right)^2}.$$

The geometric cell property is equal to 1, if a cell is only assigned to one cluster. If a cell is assigned to multiple clusters, the geometric cell property assigns the cell energy partial to the different clusters, based on the total cluster energies [22]. All cells assigned to the cluster are labeled by the index i.

Topological cell clustering achieves active noise suppression, since no-signal cells are most likely to not be included. This leads to less noise and an overall better performance than the tower approach. Nonetheless, the tower approach is faster and, therefore, is used in trigger reconstructions, in particular for Level-1 jets, in hardware.

The proto jets are passed to the trigger algorithm, deciding whether to keep a jet or not. In a next step, jets passing the algorithms are reconstructed by weighting the cells depending on their signal density $\rho_i = E_i/V_i$, where V_i is the cell volume and $E_i = |\vec{p_i}|$ the corresponding energy. With the cell location $\vec{X}_i$, the new four-momentum is given by

$$(E_{\text{rec}}, \vec{p}^{\,\text{jet}}_{\text{rec}}) = \left(\sum_i^{N_{\text{cell}}} W(\rho_i, \vec{X}_i)E_i, \sum_i^{N_{\text{cell}}} W(\rho_i, \vec{X}_i)\vec{p_i}\right).$$

Similarly, by averaging the cluster times weighted by the square of the cluster energy and the geometric cluster properties, the jet time is calculated as [23]

$$t_{\text{jet}} = \frac{\sum_i^{N_{\text{cluster}}} \left(w^{\text{geo}}_{\text{cluster},i} E_{\text{cluster},i}\right)^2 t_{\text{cluster},i}}{\sum_i^{N_{\text{cluster}}} \left(w^{\text{geo}}_{\text{cluster},i} E_{\text{cluster},i}\right)^2}.$$

Following an energy calibration, further corrections are applied, improving the precision by taking into account multiple other effects. An overview is given in Figure 3.4.

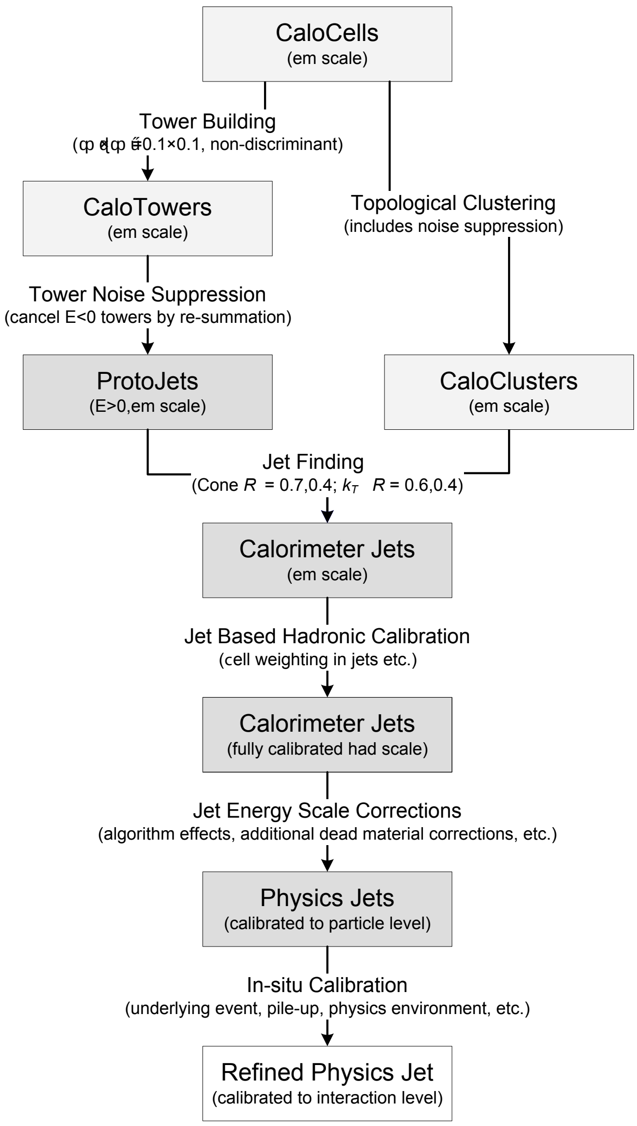

Figure 3.4.: Flow of calorimeter jet reconstruction [4].

3.6. Production of Monte Carlo samples

The production of Monte Carlo (MC) samples at ATLAS can be divided into four steps [20]. Figure 3.5 shows the sample production process step by step.

- **Event Generation** sets the base by calculating the collision physics. Independent of detector physics, the kinematics of a collision with specific decay products, chosen before simulating, are calculated. The final results only depend on collision specific parameters, such as the particle type, their distribution and the center-of-mass energy. An MC generator example is PYTHIA [24], which was used, together with MadGraph [25], for the production of the samples used in this work.

- The **detector simulation** adds the detector properties to the collision physics. While propagating the final state particles through the detector, interactions with the detector material, i.e. the energy deposits, are simulated. This simulation strongly depends on the detector properties, such as its geometry, and conditions. GEANT4 is almost always used for such simulations.

- Read-out signals of the detector, which are used for further processing, are calculated from the energy deposits. This process is called **digitization** and depends on multiple parameters describing the trigger and detector conditions, such as threshold settings. In this step, the interference of multiple bunch crossings, known as pile-up, is included. Pile-up can be divided into 2 catergories:

  - **In-time pile-up:** overlapping proton-proton collisions occurring in the same bunch-crossing as the collision of interest, and

  - **Out-of-time pile-up:** overlapping proton-proton collisions occurring in bunch-crossing just before or after the collision of interest.

  The final output is similar to the actual detector output.

- As for real detector signals, **reconstruction** algorithms calculate calibrated physics objects as particles, jets and vertices. Two formats can be used to store the data:

  - Complete Event Summary Data (ESD),

  - and the less detailed Analysis Object Data (AOD).

  A AOD subgroup called AOD derivations (DAOD) [26] is used in this work. Compared to AOD, some information is filtered and other is added (reconstructed jet collections, flavour tagging information).

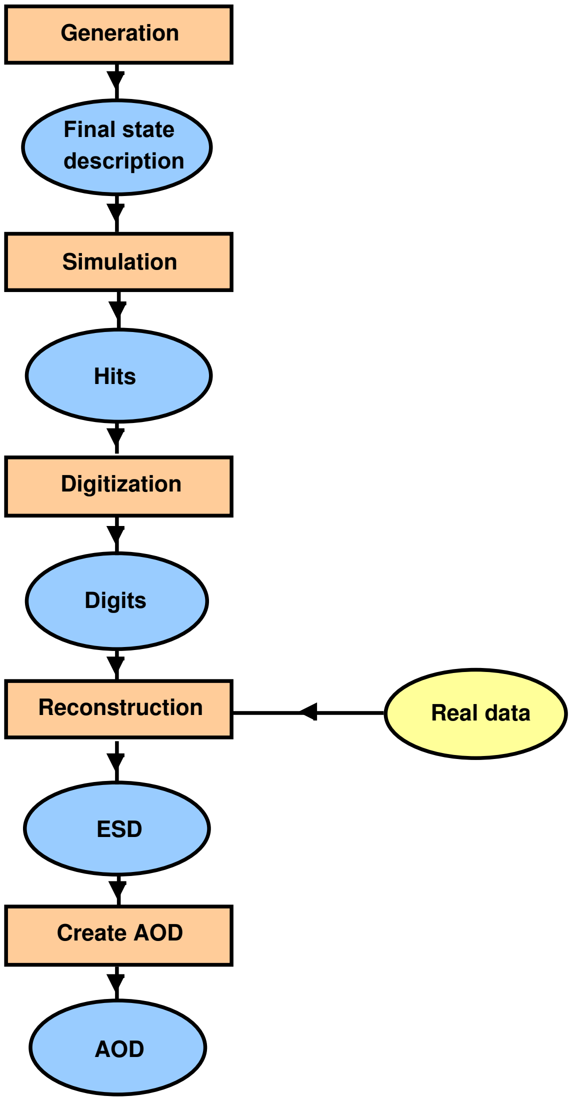

Figure 3.5.: Steps of event simulation. The detector signals are calculated within the first three steps. All further steps are equal to those applied to real detector signals [20].

4. Experimental signatures of long-lived particles

This chapter introduces long-lived particles (section 4.1) and how they are expected to interact with particle detectors (4.1.1). Section 4.3 discusses previous searches for LLPs. The idea this work is based on, is presented in section 4.2. A more detailed discussion on LLPs, their signatures in collider detectors and previous studies on this topic can be found in the article ”Collider searches for Long-Lived Particles Beyond the Standard Model” [2].

4.1. Long-lived particles

Multiple theories describing physics beyond the Standard Model predict a variety of new particles, with some of them being metastable or even stable on a scale of typical detectors. Those are also known as long-lived particles (LLPs).

Supersymmetry theories that either violate or conserve R-parity, allow the existence of LLPs. R-hadrons would be formed by hadronizing colored sparticles (e.g. squarks $\tilde{q}$ and gluinos $\tilde{g}$) as already mentioned in section 2.2.1. With the ability of changing to a state with a different electric charge, R-hadrons can create unique tracks inside magnetic fields.

4.1.1. Signatures in particle detectors

LLPs can leave signatures inside a detector in two ways:

1. Direct interactions:
   The LLP directly interacts with the detector material through electromagnetic or hadronic interactions. In this case, the LLP could be identified through the direct measurement of its interactions.

2. Indirect interactions:
   The lifetime and mass of the LLP lead to a decay of the LLP before it can interact significantly enough with the detector to be detected directly, or the LLP itself has neither color nor electric charge, so that it does not interact with the detector material. Nonetheless, the decay products can interact with the detector material, leaving unique patterns in reconstructed tracks and energy deposits.

With the task of exploring and testing physics predicted by the Standard Model of particle physics, most particle detectors are based on the assumption that heavy particles decay promptly (prompt: inside a radius smaller or comparable to the detector resolution with no measureable displacement). Therefore, detecting particles with significantly displaced decay vertices is a huge challenge. A more detailed discussion of direct and indirect interaction methods is given in [2].

Of special interest for this work are signatures of LLPs interacting indirectly with detectors such as ATLAS, specifically those giving rise to delayed detector signals.

Delayed detector signals

LLPs with high masses will travel slower compared to a SM particle of the same momentum. Hence, it will take an LLP longer to cover the same distance. The LLP will therefore leave a signal in the detector which is delayed compared to the SM signals.

With bunch crossings every $25\,\mathrm{ns}$, several subsystems have timing resolutions of $\mathcal{O}(1\,\mathrm{ns})$. This resolution could be enough to detect such delayed signals. "Delayed signal" has to be understood as a delay compared to the expected time of a signal. The expected time is defined such that a particle traveling at the speed of light from the collision point would arrive at time zero.

It should be noted that an LLP must not interact directly with the detector. Its delay can also be measured by identifying the corresponding delayed decay products.

4.2. Delayed jets

A candidate for a heavy LLP could be the gluino, discussed in section 2.2.1. As described in section 4.1.1, a displaced decay of a slow-moving LLP would cause a delayed signal. By looking closer at the gluino decay, it can be noted that the decay products are a neutralino, leaving no signal in the detector, and quarks. If the gluino properties are such that it decays before or inside the calorimeters, the quarks will hadronize and give rise to jets with a delay corresponding to the properties of the gluino and LLP.

The sensitivity of this signature is limited by the jet reconstruction limit, the detector timing resolution and the collision frequency. An example of a search using this signature is discussed in section 4.3.

4.3. Previous studies

As the theories vary, the possible combinations of masses and lifetimes do. Thus, an LLP with sufficient mass and lifetime could pass parts or even the whole detector. Depending on the specific LLP parameters, such as mass, lifetime, electric charge and hadronic charge, as well as the kinematics, such as its momentum, many possible interaction patterns could be created. Hence, a variety of ideas have been looked at, assuming direct as well as indirect interaction of the LLP with the detector. A more detailed summary is given in [2].

4.3.1. Search for LLPs using nonprompt jets at CMS

This search reported in Ref. [5] is based on predictions of gauge-mediated SUSY breaking (GMSB). In this model, delayed and displaced jets are formed by gluons, originating from the decay of a long-lived gluino. This decay includes a gravitino causing significant missing transverse momentum p_T^{miss}. A diagram of the decay is shown in Figure 4.1.

For a mass scale of TeV and a traveling range of approximately 1 m before decaying, several ns of delay are expected. Those nonprompt or delayed jets can then be identified by the timing capabilities of the CMS electromagnetic calorimeter (ECAL).

Used for this analysis are data samples of proton-proton collisions with a total luminosity of $L = 137\,\mathrm{fb}^{-1}$ at a center-of-mass energy of $E_{CoM} = 13\,\mathrm{TeV}$, collected by the CMS experiment between 2016 and 2018.

The used objects are tower jets, clustered by the anti-k_T algorithm with $\Delta R = 0.4$. Since nonprompt jets could leave no signal in the inner tracker, the CMS particle flow (PF) algorithm is not used.

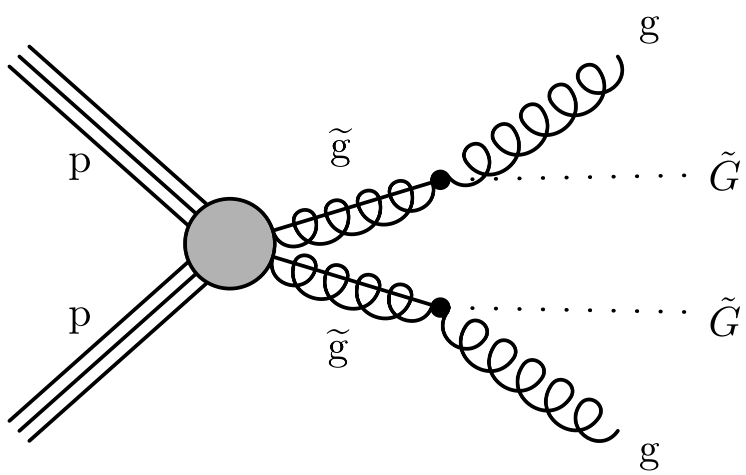

Figure 4.1.: GMSB signal Model. A gluino decays into a gluon and a gravitino [5].

The median of all times of ECAL cells within $\Delta R < 0.4$ of the jet axis and an energy of $E_{cell} > 0.5$ GeV, was defined as the jet time. Due to the spacing of 25 ns between bunch crossings, all cells outside -20 ns $< t_{cell} < 20$ ns were rejected.

In order to improve the signal quality, cuts were applied, reducing known background sources such as:

- ECAL time resolution tails,
- Electronic noise,
- In-time pileup,
- Out-of-time pileup,
- Satellite bunches,
- Beam halo,
- Cosmic ray muon hits.

Detailed descriptions can be found in the original paper [5]. After consideration of all effects, multiple selection rules (SR) have been applied. The baseline jet selections are listed in table 4.1.

Table 4.1.: Most important selections for this work.

$\lvert\eta\rvert < 1.48$
$p_T > 30\,\text{GeV}$
$t > 3\,\text{ns}$

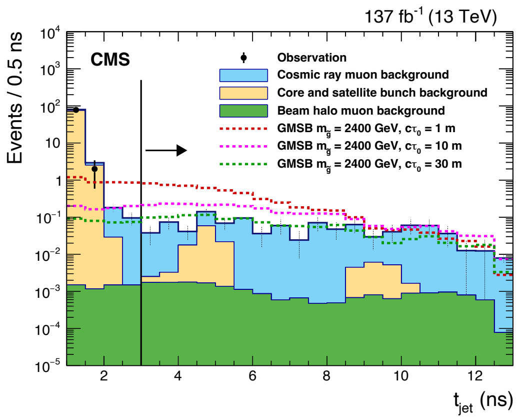

(a) Theory predictions of background and signal (colored) compared to data points (black). There are no events observed above a threshold of $t_{jet} > 3\,\text{ns}$.

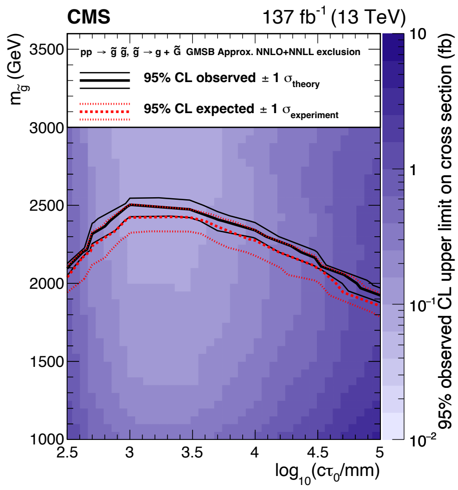

(b) Gluino masses up to 2100, 2500, and $1900\,\text{GeV}$ are excluded at 95% confidence level for proper decay lengths of 0.3, 1, and 100m.

Figure 4.2.: Study of delayed jets at the CMS experiment [5].

A comparison between the final events remaining and the theory of background and signal events is shown in Figure 4.2a. The observed data of 0 events is consistent with the predicted background of $1.1^{+2.5}_{-1.1}$ events.

The expected and observed yields are low, due to the tight construction of the selection. As shown in Figure 4.2b, based on this study, gluino masses up to 2100, 2500, and $1900\,\text{GeV}$ are excluded at 95% confidence level for proper decay lengths of 0.3, 1, and 100m.

5. Studies of jet time measurements

As discussed in section 4.3, studies looking for delayed jets used fixed selection values, such as $t_{\text{reconstructed}} > t_{\text{selection}} = 3\,\text{ns}$ [5]. This cut is chosen in order to minimize the background of fluctuating jet times, caused by detector dependent background sources. To optimize this selection, a detailed study of jet time measurements, using Monte Carlo (MC) simulated samples and measured data, is given in this chapter. All calculations and plots in this chapter were created using python 3.9.12 and ROOT 6.22.08 [27].

5.1. Jet time analysis of MC simulated samples

As described in section 3.5, the reconstructed jet times used for analysis do not represent the true jet times. The jet times contained in the analysis files are the true jet times overlaid with uncertainties of the detection and reconstruction algorithms. In this section, an understanding of the contribution of the detector, i.e. the impact of detection and reconstruction on the jet times produced, is gained. In the SM, events containing jet pairs, also known as dijet events, are primarily produced via $2 \to 2$ parton scattering processes. For energies far above the confinement scale of Quantum chromodynamics (QCD), jets with large transverse momenta emerge perpendicular to the direction of the incident partons. Such jets are likely to have a small to no delay [28]. Thus, jets in dijet events are expected to have no delay ($t_{delay} = 0\,\text{ns}$). Therefore, an observed spread of jet times can be assigned to the detector resolution and the reconstruction algorithms. An event includes the reconstructed objects of one bunch crossing. Simulated samples are identified by a dataset ID number (DSID). The DSID of the used djet sample is 364704.

To get a first indication of the jet time spread, all jets of the dijet sample are collected in bins (width $\Delta t = 0.2\,\text{ns}$) and plotted as a function of their time, as shown in Figure 5.1a.

Despite the expectation of jets with $0\,\text{ns}$ delay, the jet times spread over an interval bigger than the bunch separation of $25\,\text{ns}$. Nonetheless, a peak can be observed at approximately

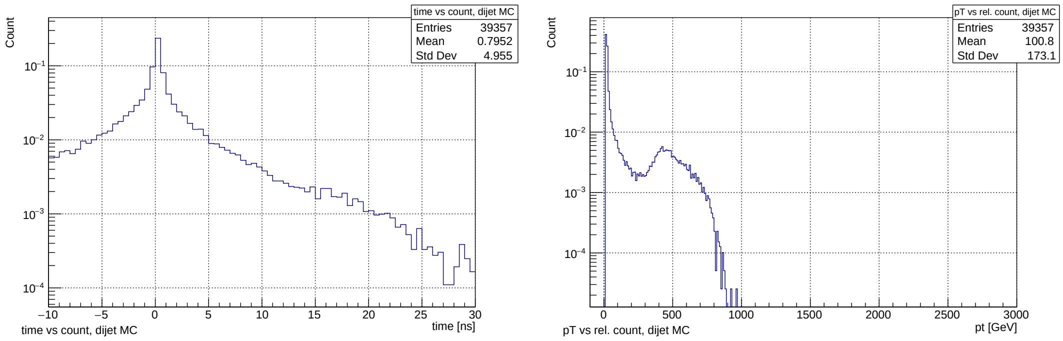

(a) Histogram with bin width of $\Delta t = 0.5\,\mathrm{ns}$. Other than expected from the physics, the jets spread over a wide range.

(b) Pile-up peak at low transverse momentum. A peak caused by the dijet physics process can be seen around $p_T \approx 500\,\mathrm{GeV}$.

Figure 5.1.: p_T and time values of dijet sample. The y-axes are shown with logarithmic scale.

0 nanoseconds. The distribution of the transverse momenta (p_T) is shown in Figure 5.1b. At low p_T, a peak, caused by pile-up jets, can be seen. As a result of the preselection applied in the investigated dijet sample, a second peak forms at $p_T \approx 450\,\mathrm{GeV}$. To limit the size of the output files, the results of the dijet simulation are stored in different datasets based on transverse momentum. In order to study the limits of the time reconstruction, the interval of transverse momenta, containing the upper p_T limit of pile-up jets, is investigated. Thus, no jets above $p_T = 1000\,\mathrm{GeV}$ are observed. As out-of-time pile-up jets are incorrectly assigned to the investigated event, their jet times can spread over a wide range. An indicator of the contribution of the pile-up jets to the jet time spread, is the time spread at low transverse momenta, as most pile-up jets have $p_T < 100\,\mathrm{GeV}$. To gain deeper insight, the jet time as a function of the transverse momentum p_T for each jet inside the dijet sample is shown in Figure 5.2.

As expected from pile-up jets, the widest spread of jet times can be observed at low transverse momentum ($p_T < 100\,\mathrm{GeV}$). Due to a spread bigger than the bunch separation for such low momenta, it will be nearly impossible to identify truly delayed jets. Thus, in a selection rule, jets with $p_T < 100\,\mathrm{GeV}$ should be rejected.

With increasing transverse momentum, the accuracy of jet time measurements improves. Nonetheless, for all p_T a spread around approximately $0\,\mathrm{ns}$ can be observed. This spread is caused by the limitations of the detector and can be used as a measure for the accuracy

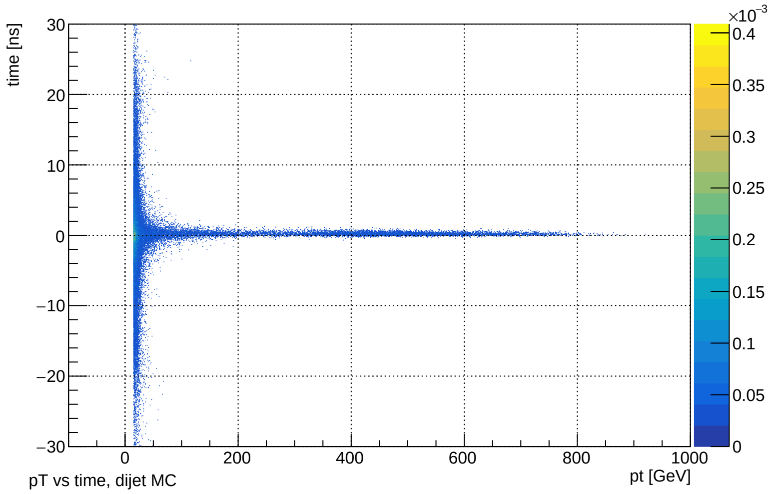

Figure 5.2.: Time vs. p_T for dijet sample jets. The color scheme represents the density of jets in different areas.

Table 5.1.: DSIDs and decay specific parameters of LLP samples.

DSID	Gluino mass [GeV]	Neutralino mass [GeV]	Gluino lifetime [ns]
449539	2400	100	0.01
449501	2400	100	3
449314	2400	100	10
449432	2400	100	30

of the jet time reconstruction of the detector.

As described in section 4.2, the reconstructed jet times are investigated in order to identify delayed jets, caused by LLPs. A representative for the various possibilities that can cause delayed jets, are simulated samples, produced by simulating decays as described in section 4.1. Next, such LLP samples are investigated. The DSIDs of the used samples, along with the gluino mass, the gluino lifetime and the gravitino mass used in the decay simulation, are listed in Table 5.1.

In the following, I will differentiate between the LLP samples by stating the used gluino lifetime, since this is the only parameter that varies between the different files. It should also be noted, that the stated lifetime does not directly correspond to an expected delay.

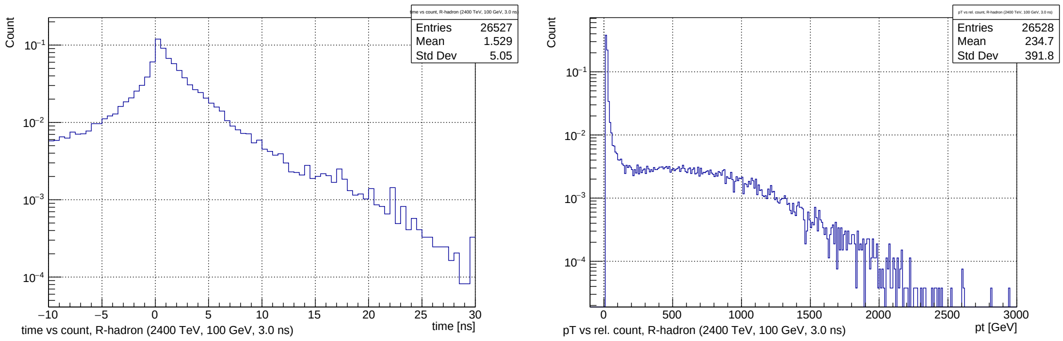

(a) Histogram with bin width of $\Delta t = 0.5\,\mathrm{ns}$. Despite LLP physics simulated, background events create a peak at at $0\,\mathrm{ns}$

(b) Pile-up peak at low transverse momentum. Slowly decreasing amount of jets, for transverse momenta above $p_T \approx 200\,\mathrm{GeV}$.

Figure 5.3.: p_T and time values of LLP ($3\,\mathrm{ns}$) sample jets.The y-axes are shown with logarithmic scale.

The observed true delay depends on many different parameters, such as the momentum of the gluino. Nonetheless, observed differences in the time and momentum distributions can be assumed to be caused by the physics used in the simulations, as only the decay and not the detector simulation differs.

As the main example, the $3\,\mathrm{ns}$ LLP sample will be investigated in the following. The jet time distribution is shown in Figure 5.3a, the transverse momentum distribution is shown in Figure 5.3b. Similar plots for the other LLP samples are listed in Appendix A.1.

Despite the fact that delayed jets were used in the sample production for the jet time distribution, approximately the same shape as for the dijet sample is observed. For the transverse momentum distribution, a clear peak of pile-up jets at low momenta can be seen. For higher momenta ($p_T > 100\,\mathrm{GeV}$), the distribution stays constant up to $p_T \approx 1000\,\mathrm{GeV}$ and then decreases approximately exponentially.

Because of the LLP decay in the samples, multiple delayed jets with $p_T > 100\,\mathrm{GeV}$ per event are expected. Thus, they are distinguishable from pile-up jets with poorly measured times.

Figure 5.4 shows the jet time plotted as a function of jet transverse momentum. The color scheme indicates the density of jets within a certain area. At low p_T, the pile-up spread dominates. For $p_T > 100\,\mathrm{GeV}$, a clear difference to the dijet sample can be seen.

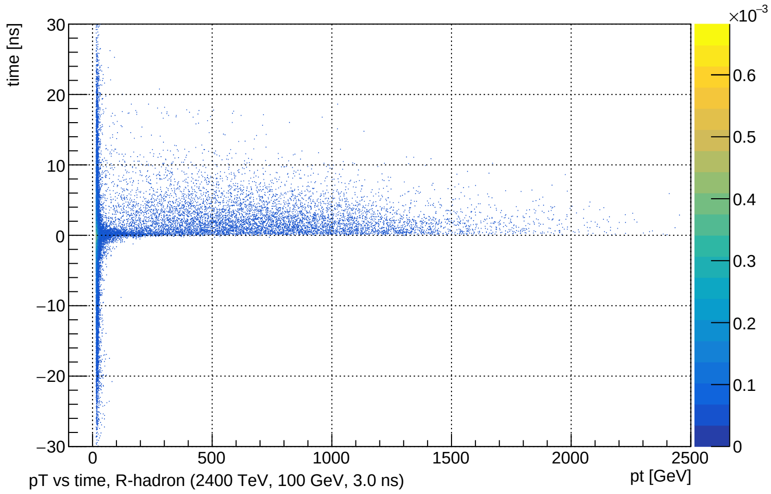

Figure 5.4.: Time vs. p_T for LLP ($3\,\mathrm{ns}$) sample jets. The color scheme represents the density of jets in different areas.

As expected, the delays observed are distributed uniformly between 0 ns and 25 ns for momenta up to p_T of several TeV. The fact that the delays are only positive, supports the hypothesis that those delays are caused by physics and not by the detector or the reconstruction algorithms.

This is a first indication that the resolution of jet times is good enough to identify a variety of delayed jets. A similar structure can be observed for the samples with LLP lifetimes of 10 ns and 30 ns. It should be mentioned that it is difficult to measure delays of approximately 30 ns with sufficient precision, since the bunch spacing is mostly 25 ns. The distributions of the 0.01 ns sample looks nearly identical to the dijet distributions. This is expected, since the time reconstruction resolution is larger than the expected delays, as later shown in section 6.1.1.

Pile-up influence on jet time distributions

As discussed before, the spread of pile-up jet times dominates the time spectra for all samples. Thus, an investigation of the total time distribution does not add much discrimination power. To reduce pile-up effects in this section, only jets with $p_T > 100$ GeV are

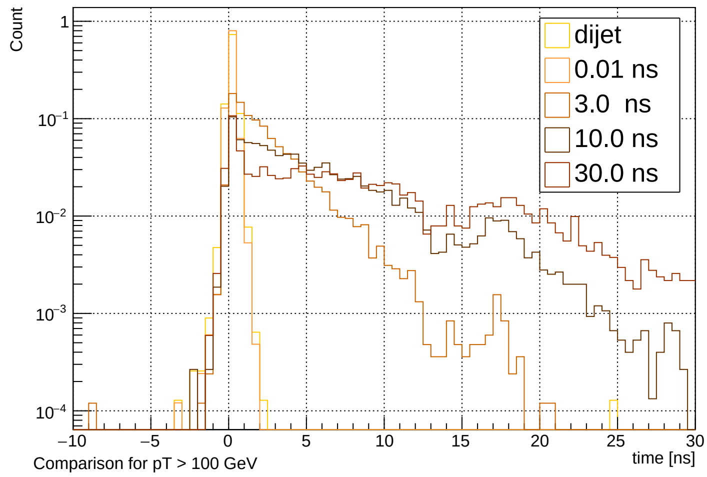

Figure 5.5.: Comparison of jet times for jets with $p_T > 100$ GeV from simulated samples. The dijet sample and the 0.01 ns sample show the same structure. For all other lifetimes, large delays can be seen.

taken into account. A comparison of all simulated samples is shown in Figure 5.5. One can clearly differentiate between the LLP samples and the dijet sample, if the lifetime of the gluino is long enough to create significant delays. Here, significant means that the delay is larger than the detector resolution. Thus, the distribution of the 0.01 ns sample does not differ significantly from the dijet distribution. Detailed studies will be discussed in chapter 6.

With increasing lifetime of the gluino, the jet time distribution flattens out and the average delay shifts to larger times. As a consequence, the jet times shift increasingly to delays overlapping with the next bunch crossing. Rejection methods for out-of-time pile-up jets, like an upper time limit for jets times, will lead to a loss of those jets. This is a first indication of the limits of this detection method.

It should be mentioned, that jets with delays larger than 25 ns can be assigned to the wrong bunch crossing. Consequently, such jets can be identified with a delay of $t^{\text{jet}}_{\text{recon}} \approx t^{\text{jet}}_{true} - 25$ ns, creating an additional background source for the correct identification of delayed jets.

5.2. Jet time analysis of measured data

Since not all effects can be simulated, simulations are only up to a certain level capable of reflecting the real world. Thus, measured data is investigated, which can be reconstructed offline using plenty of CPU resources or online, on the fly, with strictly limited access to CPU capacities. Due to the limited computing power for online reconstruction, a simplified version of the reconstruction code used offline is used online. The CPU power and algorithms used lead to the expectation of higher accuracy for offline reconstructed data than for online reconstructed data.

Table 5.2.: Run numbers and luminosity blocks of measured data.

Reconstruction	run number	luminosity block
offline	305543	000001
online	438235	0586
		0802
		0865
		0887
		0898

The measured data used is stored in DAOD files, as described in section 3.5, and labeled by the run number. To reduce the file size, the data of a single run is split up into multiple files, depending on luminosity block during which they were measured. Thus, a file can be identified by its run number and luminosity block. The files used for this analysis are listed in Table 5.2.

5.2.1. Offline reconstructed samples

The full complexity of all effects accruing in the detector cannot be simulated. Thus, for measured data, the resolution is expected to decrease compared to simulated data.

From the jet time spread, shown in Figure 5.6a, the expected decrease in resolution can not be seen directly. The shape looks similar to the simulated data. Pile-up jets also appear for measured and offline reconstructed jets as a peak at low p_T is visible in Figure 5.6b. The transverse momenta follow an exponential decay. This is caused by the variety of different processes the measured data contains.

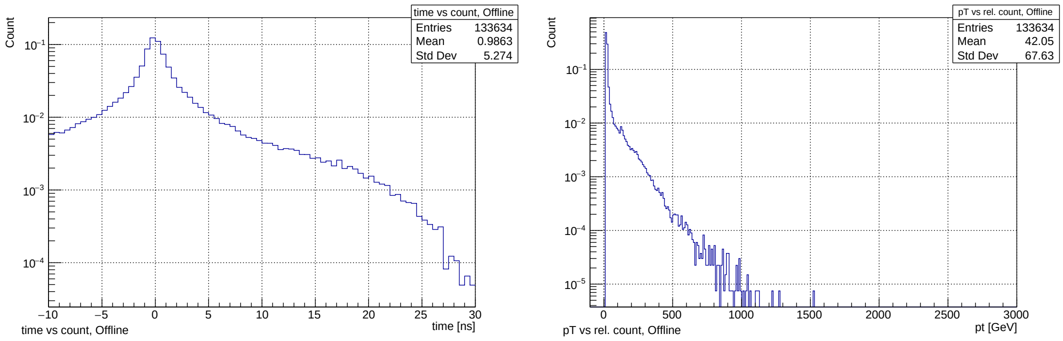

(a) Histogram with bin width of $\Delta t = 0.5\,\text{ns}$. Time values spread over the complete range of one bunch crossing.

(b) Pile-up peak at low transverse momentum. With increasing transverse momentum, the amount of jets decreases exponentially.

Figure 5.6.: p_T and time values of measured and offline reconstructed jets. The y-axes are shown with logarithmic scale.

As discussed in section 5.1, jet times as a function of transverse momentum give an indication of the time reconstruction accuracy. For the offline reconstructed measured data, this relation is plotted in Figure 5.7.

Clearly, the region of low momenta ($p_T < 100\,\text{GeV}$) is dominated by pile-up jets. At $\pm 25\,\text{ns}$, the jets spread over a larger range of momenta compared to the other pile-up jets with delays smaller than $25\,\text{ns}$. This is caused by jets assigned to the wrong bunch crossing, also known as out-of-time pile-up. The core structure is similar to the simulated dijet behavior. Nevertheless, the jet time reconstruction accuracy is worse. Single jets with times $|t_{\text{jet}}| > 5\,\text{ns}$ spread over a broad range of transverse momenta. Due to the fact that those jet times are distributed equally over positive and negative values, they most likely are caused by the reconstruction process.

5.2.2. Online reconstructed samples

With less computing time and power compared to offline reconstruction, the online reconstruction algorithms are expected to have worse accuracy. Note that the online reconstruction algorithm assigns the value $t_{jet} = 0\,\text{ns}$ to all jet time calculations that exceed a certain computing time. This occurs approximately 1 out of 500 times ($0.174\,\%$).

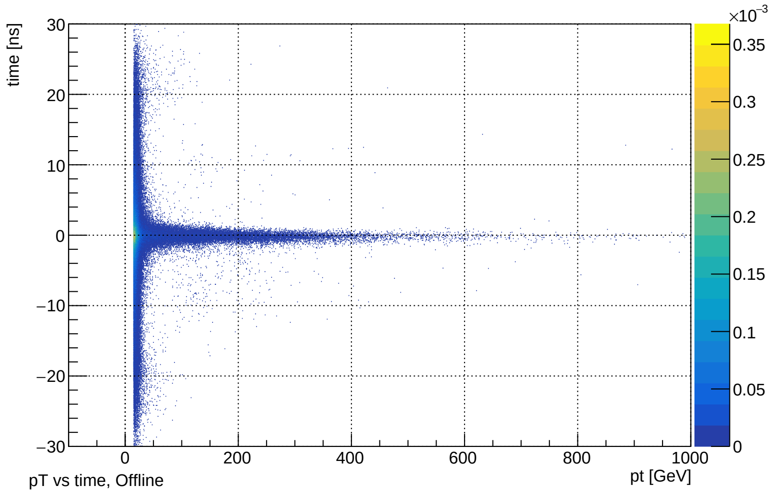

Figure 5.7.: Time vs. p_T for measured and offline reconstructed jets. The color scheme represents the density of jets in different areas.

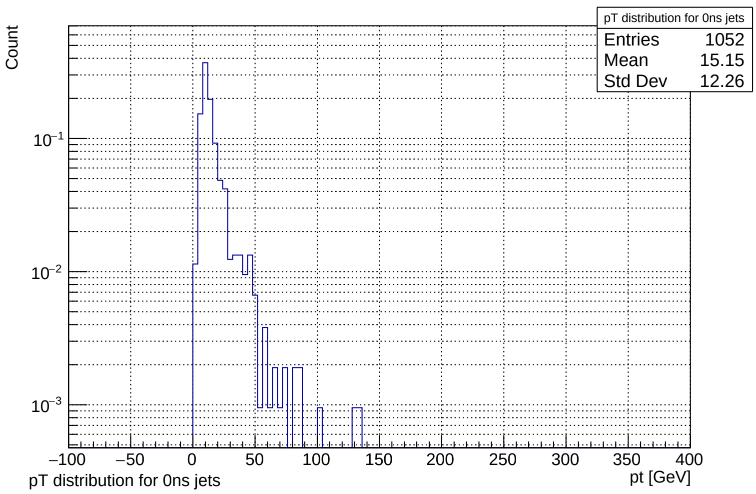

Figure 5.8.: Online jets with failed time reconstruction. The y-axes is shown with logarithmic scale.

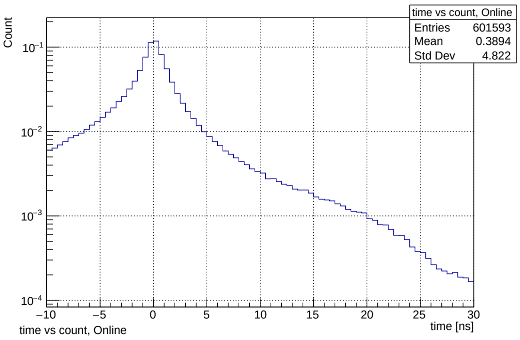

(a) Histogram with bin width of $\Delta t = 0.5\,\mathrm{ns}$. Little bump caused by out-of-time pile-up at $2.5\,\mathrm{ns}$

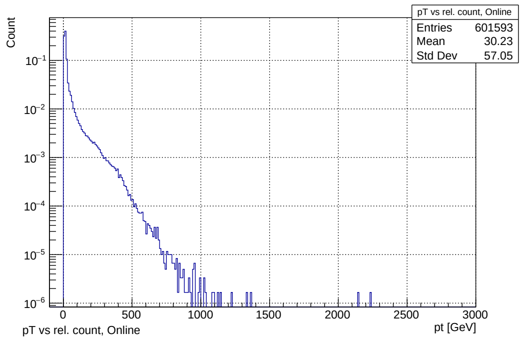

(b) Pile-up peak at low transverse momentum. With increasing transverse momentum, the amount of jets decreases exponentially.

Figure 5.9.: p_T and time values of measured and online reconstructed jets. The y-axes are shown with logarithmic scale.

By looking at the p_T distribution of jets with $t_{jet} = 0\,\mathrm{ns}$, shown in Figure 5.8, it can be seen that only a tiny fraction of those jets ($\sim 2\,‰$) has a momentum larger than $100\,\mathrm{GeV}$. Due to pile-up jets, as discussed in section 5.1, jets below $100\,\mathrm{GeV}$ will be rejected in further analysis. Therefore, no useful information will be lost by excluding those jets from the following overview plots.

The time and momentum distributions of the online sample, shown in Figure 5.9, behave as expected. Pile-up jets create a peak at low momenta as for offline reconstructed data. Nonetheless, the pile-up jets have more impact on the shape of the p_T-distribution and, thus, compared to the lower end, less high momentum jets are observed.

As shown in Figure 5.10, online reconstructed jet times spread widely compared to offline jet times. The times are distributed uniformly across positive and negative values and, thus, are most likely also caused by the reconstruction algorithm and imperfections in the detector or its calibration. Nevertheless, since the shown data has been measured, the exact physics processes included are not known. Therefore, there is a possibility that some of the measured delays are caused by LLPs. Note that the effects of out-of-time pile-up create the small bump at $t = \pm 25\,\mathrm{ns}$. Those jets can have momenta larger than $100\,\mathrm{GeV}$, resulting in LLP like data points.

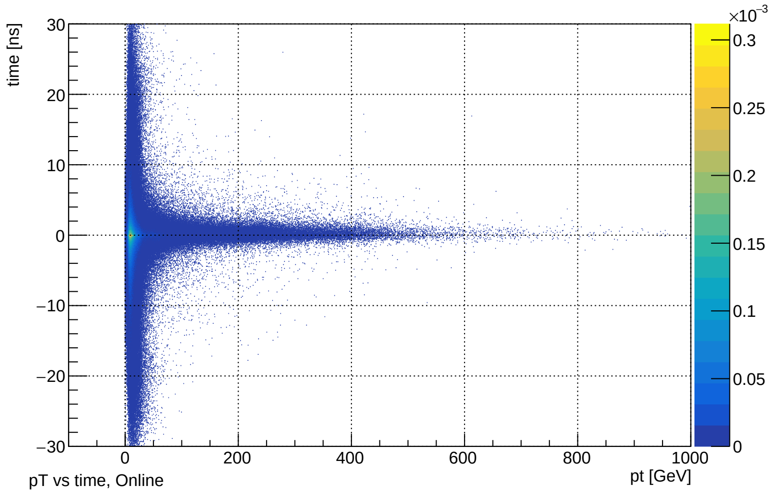

Figure 5.10.: Time vs. p_T for measured and online reconstructed jets.

6. Designing a trigger algorithm based on jet timing

Until today, fixed values are implemented as a selection rule (SR) for jet times when identifying LLP events. As shown in chapter 5, the accuracy of jet times is dependent on p_T. This suggests a dynamic selection rule for jet times could have benefits. By using a p_T dependent time selection rule, background events can be rejected with nearly the same efficiency, while the rejection of LLPs can be minimized. In this chapter, the relation between the jet time and the corresponding p_T value is studied and quantified in section 6.1. Different possibilities for selection rules, which are making use of this relation, are discussed in section 6.2. Section 6.3 analyses the performance of different approaches. All calculations and plots in this chapter were created using python 3.9.12 and ROOT 6.22.08 [27].

6.1. Correlation between transverse momentum and timing

Section 5 shows that the precision of the reconstructed time is correlated to the transverse momentum of the same jet. By comparing the figures, showing the jet time as a function of transverse momentum, a huge difference in the time distribution between the LLP samples and the dijet sample can be observed. This indicates that, based on the jet time and the p_T value, a delayed LLP jet can be identified. For this purpose, the relation between jet time and p_T values needs to be understood and quantified.

Section 6.1.1 discusses a possible parameterization, based on the simulated dijet sample. This parameterization is translated to measured offline and online data in 6.1.2 and 6.1.3.

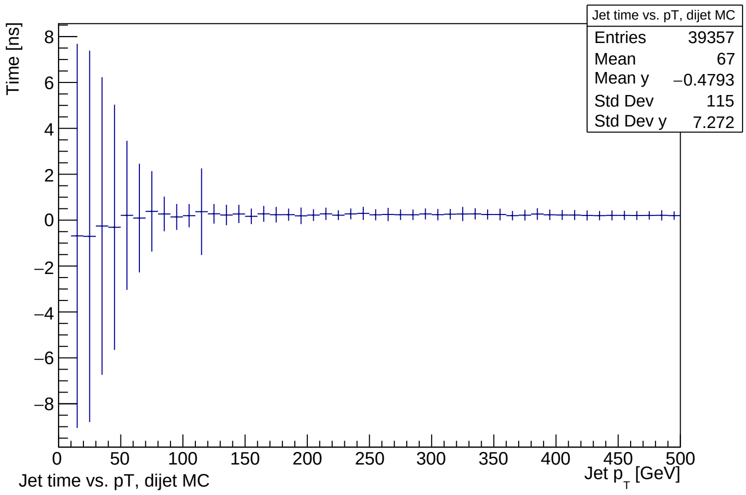

Figure 6.1.: Jet times of dijet sample shown as a function of p_T. Shown are the mean values and the standard deviation of each bin. Caused by lack of statistics, a relatively larger uncertainty can be seen at $p_T = 125\,\text{GeV}$.

6.1.1. MC simulated and offline reconstructed jets

As already discussed, the 2D plots shown in chapter 5 indicate a relation between jet time and jet transverse momentum. Figure 6.1 plots the average jet time as a function of p_T, separated into bins of width $\Delta p_T = 10\,\text{GeV}$. The uncertainties shown represent a measure (i.e. the standard deviation) of the distribution in each bin. The values are calculated by the plot object TProfile itself, which is part of the ROOT library.

The distributions of transverse momenta, shown in chapter 5, imply an imbalance of statistics between high and low transverse momenta. Consequently, for low transverse momenta ($p_T < 100\,\text{GeV}$), smaller statistical uncertainties are expected compared to higher transverse momenta.

As expected, the mean time value of each bin is approximately $0\,\text{ns}$. A mentionable characteristic is the decreasing standard deviation with increasing p_T. As mentioned in section 5.1, the time spreads below $100\,\text{GeV}$ are too large to justify the assumption an LLP is identified.

For $p_T \approx 125\,\text{GeV}$, the standard deviation seems to increase again. By looking at the jet

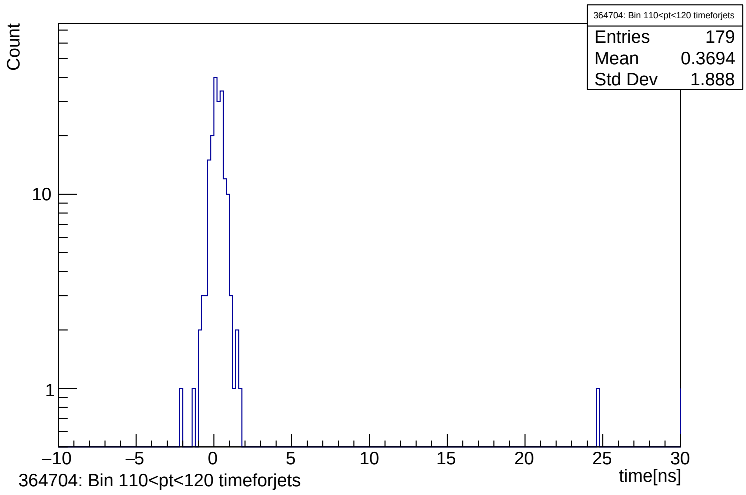

Figure 6.2.: Jets of dijet sample within the Interval $110\,\text{GeV} < p_T^{jet} < 120\,\text{GeV}$. Most jet times are centered around $0\,\text{ns}$, with one exception at $\sim 25\,\text{ns}$. This exception causes a non representative standard deviation.

time distribution of this bin $(120\,\text{GeV} < p_T < 130\,\text{GeV})$ separately (Figure 6.2), it can be seen that one jet, with a time of $t_{jet} \approx 25\,\text{ns}$, causes this larger standard deviation value. Most likely, this jet is cause by out-of-time pile-up. Such cases could be avoided in further investigations by only taking jets within small $|t_{jet}|$ into account. A specific interval will be defined later in this section.

By looking at the time distributions of all bins separately (Appendix B.1.1), it can be seen that, as expected, most jets are forming a Gaussian like distribution, located around $0\,\text{ns}$. As already mentioned, background events, such as pile-up, can cause the calculation of misleading values. This can be avoided, by assuming a Gaussian behavior around approximately $0\,\text{ns}$ for each p_T interval. Hence, for each interval, a Gaussian function

$$f(x) = p_0 \cdot e^{-0.5 \cdot \left(\frac{x-p_1}{p_2}\right)^2}, \tag{6.1}$$

is fitted to the jet time distributions for $|t_{jet}| < 3\,\text{ns}$ (Appendix B.1.1). Due to the simulated dijet physics, it can be assumed that the jet time distributions are caused by detector limits and imperfections within the reconstruction algorithms. Thus, the fitted Gaussian functions are a measure of the jet time reconstruction accuracy at a certain transverse momentum.

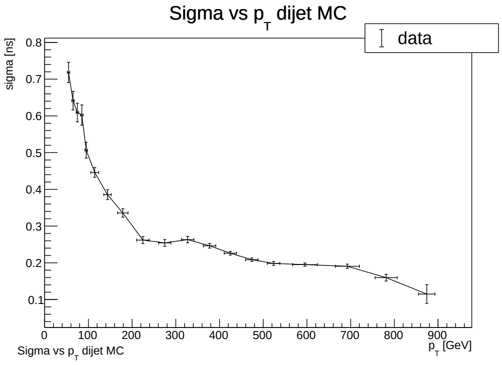

(a) Standard deviation of p_T intervals. An overall decreasing standard deviation with increasing p_T trend can be seen.

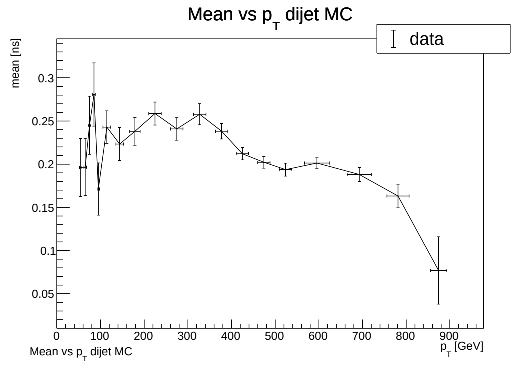

(b) Mean value of p_T intervals. An overall constant value can be seen.

Figure 6.3.: p_T and time values of dijet sample. The y-axis are shown with a logarithmic scale.

Shown in Figure 6.3a and Figure 6.3b are the mean values and the standard deviations as a function of transverse momentum. The corresponding p_T values represent the mean transverse momentum of the investigated interval (Appendix B.1.1). By optimizing the trade-off between maximal interval size for better statistics and minimal interval size to not miss small features the used p_T intervals were chosen.

The standard deviations follow an exponential decay, converging to a constant value of approximately $t_{const} \approx 0.2$ ns. At this level of timing measurements, effects, such as detector noise and imperfect timing calibration of the cells, have a non-negligible influence on the measured jet time. Therefore, this constant value can be seen as an indicator of the detector resolution and the experimental limits.

In order to create a dynamic selection rule, the relation between the jet time and the transverse momentum must be quantified. As mentioned before, the standard deviation, measuring the distribution of jet times at a certain transverse momentum p_T, seems to decrease exponentially with increasing transverse momentum . Therefore, an exponential function given by

$$f(x) = e^{p_0 + p_1 \cdot x} + C, \tag{6.2}$$

is fitted to the standard deviations plotted in Figure 6.3a.

Table 6.1.: Parameter values from exponential fit to standard deviations of the jet timing distributions of the dijet sample.

Parameter	Value	Uncertainty
p_0	-3.21×10^{-1}	$\pm 4.80 \times 10^{-2}$
p_1	$-7.80 \times 10^{-3}\,\mathrm{GeV}^{-1}$	$\pm 4.75 \times 10^{-4}\,\mathrm{GeV}^{-1}$
C	$1.88 \times 10^{-1}\,\mathrm{ns}$	$\pm 3.94 \times 10^{-3}\,\mathrm{ns}$

The fit values are listed in Table 6.1, the fit result is shown in Figure 6.4a. The exponential function does describe the main trend. Hence, the fit result can be seen as the desired parameterization of the relation between jet time and transverse momentum.

For the mean value, a nearly linear behavior can be observed. As a consequence, a linear function, given by

$$g(x) = a \cdot x + b, \tag{6.3}$$

is fitted to the mean values and plotted in Figure 6.4b. The fit values are listed in Table 6.2.

Table 6.2.: Parameter values from linear fit to mean values of the jet timing distributions of the dijet sample.

Parameter	Value	Uncertainty
a	$-1.39 \times 10^{-4}\,\frac{\mathrm{ns}}{\mathrm{GeV}}$	$\pm 1.78 \times 10^{-5}\,\frac{\mathrm{ns}}{\mathrm{GeV}}$
b	$2.76 \times 10^{-1}\,\mathrm{ns}$	$\pm 8.69 \times 10^{-3}\,\mathrm{ns}$

It should be noted that the fitted functions represent the overall behavior. The following assumptions could have lead to inaccuracies:

- Assumption of Gaussian distribution of jet times.
- Assumption of exponential decay of standard deviations.
- Assumption of linear behavior of mean values. Note that a linear model is not the perfect choice, but since the values are small, the achieved parameterization is sufficient enough for the purposes if this work.
- Overlap of multiple distributions, caused by p_T intervals.
- Limited statistics.

Section 6.3 will show that this parameterization is sufficient to define a significance based selection rule, justifying the assumptions made.

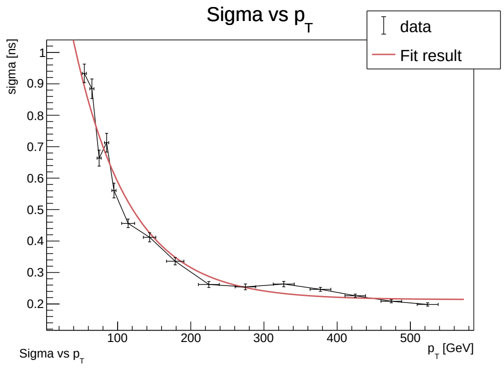

(a) Standard deviation of p_T intervals for the dijet sample. Exponential function, shown in red, is fitted.

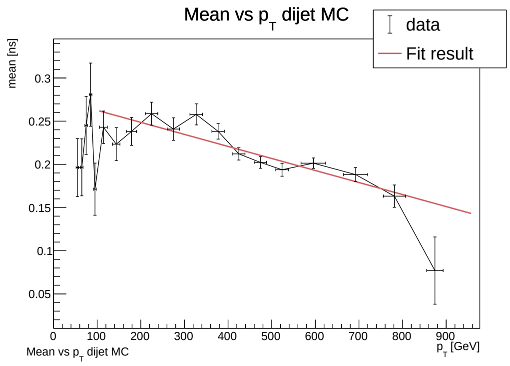

(b) Mean value of p_T intervals. An overall constant value can be seen.

Figure 6.4.: p_T and time values of dijet sample. The y-axis are shown with a logarithmic scale.

6.1.2. Measured and offline reconstructed jets

In section 6.1.1, the relation between jet time and transverse momentum is parameterized by an exponential function. As discussed in chapter 5, not all effects are simulated and, thus, simulated samples can be used as indicators, but do not represent the behavior of measured data. Therefore, this section will parameterize the relation between jet time and transverse momentum for measured and offline reconstructed data.

For the measured and offline reconstructed data, the distribution of jet times as a function of transverse momentum, shown in Figure 6.5, is similar to the structure observed for the simulated values, discussed in section 6.1.1. Thus, the Gaussian fits to each p_T interval, as well as the exponential and linear fits to the obtained standard deviations and mean values are repeated. All figures corresponding to those steps are shown in Appendix B.1.2. The fitted values for the exponential function are listed in Table 6.3. The fitted values for the linear function are listed in Table 6.4.

The standard deviation values and the fitted exponential function are shown in Figure 6.6a. The constant value C of the exponential function is with $t_{const} \approx 0.47\,\text{ns}$ approximately

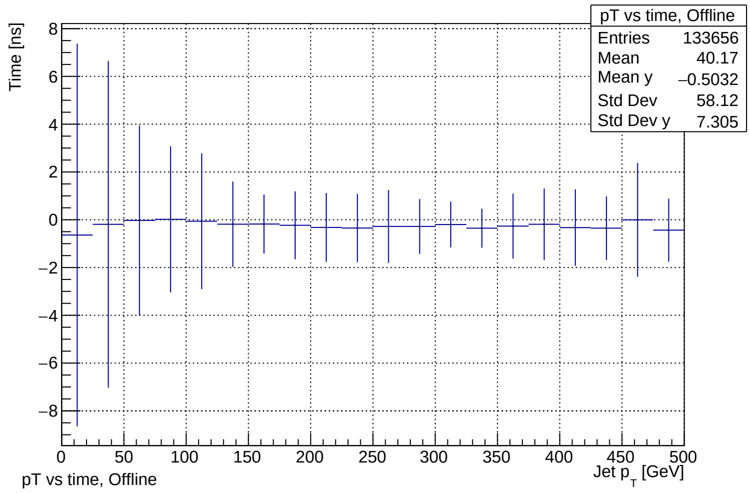

Figure 6.5.: Observed mean and spread of offline jet times in bins of p_T.

Table 6.3.: Parameter values from exponential fit to standard deviations of the jet timing distributions of measured and offline reconstructed data.

Parameter	Value	Uncertainty
p_0	-4.89×10^{-1}	$\pm 9.58 \times 10^{-2}$
p_1	$-1.24 \times 10^{-2}\,\mathrm{GeV}^{-1}$	$\pm 1.54 \times 10^{-3}\,\mathrm{GeV}^{-1}$
C	$4.53 \times 10^{-1}\,\mathrm{ns}$	$\pm 9.69 \times 10^{-3}\,\mathrm{ns}$

double the value observed for simulated data. Since the constant value represents the detector and reconstruction limits, the difference in C can be explained by experimental effects, not included in the simulations.

Nonetheless, the method of parameterization is translatable to measured data. Note that the same assumptions as for simulated data were made. Section 6.3 will justify these assumptions also in the case of measured data.

6.1.3. Measured and online reconstructed jets

For the design of a new dynamic trigger algorithm, the relation between jet times and transverse momentum must be understood and parameterized for online reconstructed

Table 6.4.: Parameter values from linear fit to mean values of the jet timing distributions of the measured and offline reconstructed sample.

Parameter	Value	Uncertainty
a	$-5.95 \times 10^{-4}\,\frac{\text{ns}}{\text{GeV}}$	$\pm 5.24 \times 10^{-5}\,\frac{\text{ns}}{\text{GeV}}$
b	$-2.19 \times 10^{-2}\,\text{ns}$	$\pm 1.31 \times 10^{-2}\,\text{ns}$

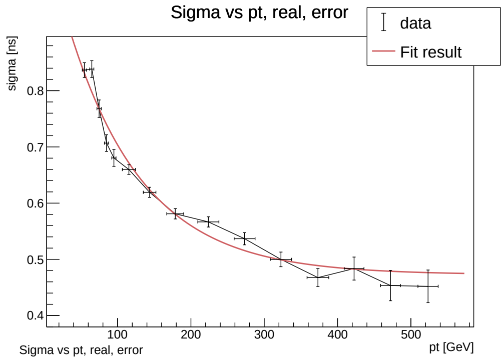

(a) Standard deviation of p_T intervals of measured data. Exponential function, shown in red, is fitted.

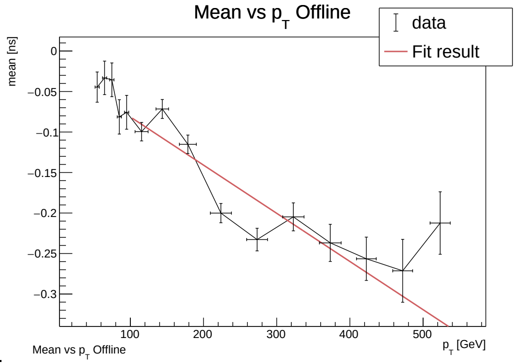

(b) Mean value of p_T intervals. An overall constant value can be seen.

Figure 6.6.: p_T and time values of offline sample. The y-axis are shown with a logarithmic scale.

data. The time spread of the jets is much wider for online reconstruction than for offline reconstruction, as shown in chapter 5. As a consequence, this section derives a parameterization at the online reconstruction level.

The wide spreads observed in section 5.2.2 reflect the relation between jet time and transverse momentum shown in Figure 6.7. Nonetheless, a decreasing trend of the time spreads as function of p_T is observable.

Note, the derived parameterization of online reconstructed data is used as a foundation for a trigger selection rule, used in the ATLAS detector. Therefore, in order to decrease the influence of statistical effects, more events were used for this analysis.

A parameterization is derived by fitting Gaussian functions to the timing distributions of p_T intervals and a linear and exponential function to the results of the Gaussian fits. The results of the linear and exponential fit are listed in the Tables 6.5 and 6.6.

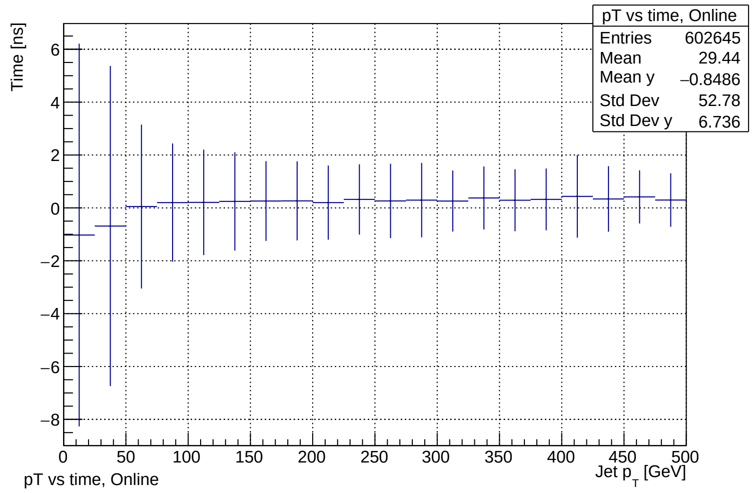

Figure 6.7.: Observed mean and spread of online jet times in bins of p_T.

Table 6.5.: Parameter values from linear fit to mean values of the jet timing distributions of the measured and online reconstructed sample.

Parameter	Value	Uncertainty
a	$1.81 \times 10^{-4}\,\frac{\mathrm{ns}}{\mathrm{GeV}}$	$\pm 4.26 \times 10^{-5}\,\frac{\mathrm{ns}}{\mathrm{GeV}}$
b	$1.60 \times 10^{-1}\,\mathrm{ns}$	$\pm 1.01 \times 10^{-2}\,\mathrm{ns}$

Appendix B.1.3 shows all Gaussian fits. The exponential and linear fit are shown in Figure 6.8a and 6.8b.

Despite the wide spreads, a parameterization of the jet time as a function of transverse momentum can be derived for online reconstructed data. Nevertheless, the wide spreads are reflected in the fit parameters. The constant value C, describing the detector and reconstruction limits, is noticeably larger than for offline reconstructed data. For low transverse momenta, the resolutions is approximately equivalent, leading to a less steep decrease of the exponential function. Note that the assumptions discussed in section 6.1.1 also apply to the parameterization of online reconstructed data. As for simulated and offline reconstructed data, the sufficiency of all assumptions is justified in section 6.3.

Table 6.6.: Parameter values from exponential fit to standard deviations of the jet timing distributions of measured and online reconstructed data.

Parameter	Value	Uncertainty
p_0	-8.11×10^{-1}	$\pm 1.22 \times 10^{-1}$
p_1	$-1.43 \times 10^{-2}\,\mathrm{GeV}^{-1}$	$\pm 1.98 \times 10^{-3}\,\mathrm{GeV}^{-1}$
C	$6.82 \times 10^{-1}\,\mathrm{ns}$	$\pm 7.04 \times 10^{-3}\,\mathrm{ns}$

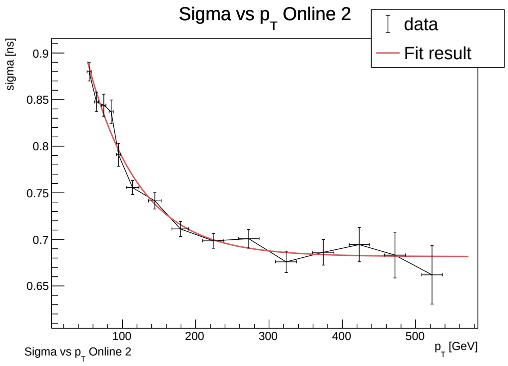

(a) Standard deviation of p_T intervals of measured data. Exponential function, shown in red, is fitted.

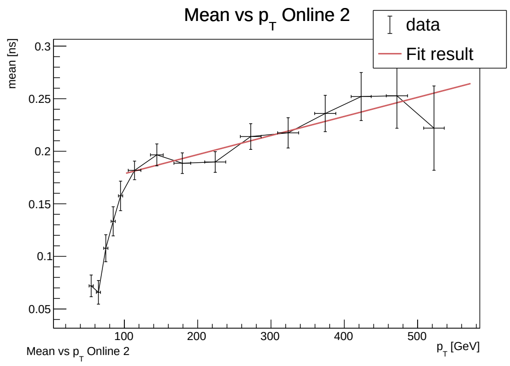

(b) Mean value of p_T intervals. An overall constant value can be seen.

Figure 6.8.: p_T and time values of online sample. The y-axis are shown with a logarithmic scale.

6.2. Significance based selection rules

Section 3.4 discusses the ATLAS Trigger System and its capabilities in detail. As mentioned, the computing resources for event reconstruction are extremely limited. Thus, for selection rules, not only the signal to noise ratio must be optimized, but also the number of accepted events must be within the available range. In the following, different approaches of selection rules are based on the parameterization of section 6.1.3.

To reduce background events caused by pile-up, all selection rules share a requirement. The common requirement and, thus, requirement number one for each selection rule is, that each jet further considered must exceed a transverse momentum of $p_T = 100\,\mathrm{GeV}$.

This condition can be combined with different requirements on the time values, based on the parameterization of section 6.1.3.

Recall, the exponential function calculates the standard deviation of a Gaussian function, corresponding to a specific transverse momentum. This standard deviation is a measure of the time distribution at this specific transverse momentum. This information can then be used to assign a significance to the corresponding jet time. Significance is here defined as

$$\text{sig} = \frac{t_{jet}}{\sigma_t(p_{\mathrm{T}}^{\mathrm{jet}})}. \tag{6.4}$$

To improve the trustworthiness of the calculated significance, the mean value (μ_t) of the Gaussian distribution is taken into account as a shift of the measured jet time, resulting in

$$\text{sig} = \frac{t_{jet} - \mu_t}{\sigma_t(p_{\mathrm{T}}^{\mathrm{jet}})}. \tag{6.5}$$

By rearranging equation 6.5, the requirement of a minimal significance ($\text{sig}_{jet} > \text{sig}_{min}$ can be translated into a minimal delay a jet time must exceed:

$$t_{jet} > \text{sig}_{min} \cdot \sigma_t(p_{\mathrm{T}}^{\mathrm{jet}}) + \mu_t. \tag{6.6}$$

Based on this relation, the following selection rules can be defined:

(a) One jet with a significance of 3:
Each jet is analyzed individually. If a jet exceeds a significance of 3 and has a transverse momentum greater that $100\,\mathrm{GeV}$, the complete event is saved.

(b) One jet with a significance of 2:
Each jet is analyzed individually. If a jet exceeds a significance of 2 and has a transverse momentum greater that $100\,\mathrm{GeV}$, the complete event is saved.

(c) 2 jets per event with a significance of 2:
As descussed in section 4.1, decays of LLPs can give rise to multiple delayed jets. Therefore, one LLP event most likely contains 2 delayed jets. For an event to be considered as relevant, 2 jets of the event must exceed a significance of 2 and have a transverse momentum greater than $100\,\mathrm{GeV}$. Coincidence requirements are a useful tool to reduce background to a minimum, as shown in section 6.3,

(d) 2 jets per event with a significance of 3:
This selection rule is as described in c), just with a more strict significance requirement of 3.

(e) Constant minimum time of $t_{min} = 3$ ns:
For comparison, a constant minimal time requirement of $t_{min} = 3$ ns, in combination with the $p_T > 100$ GeV requirement is included in the analysis.

Note, no upper limits are investigated in this study. Upper time limits might be used as a tool to diminish pile-up background further. At the same time, maximum time requirements will limit the range of measurable delays from LLPs, resulting in decrease of measured signal events.

6.3. Evaluation of selection rule performances

Recall that the exponential function describes the standard deviations σ of Gaussian functions, quantifying the jet time distributions at a certain p_T. For Gaussian shaped timing distributions, as it is the case for background events, we expect a randomly chosen time to be smaller than 2σ with a probability of $p(2\sigma) \approx 99.86\%$. For 3σ the expected probability is $p(3\sigma) \approx 99.95\%$. Based on those values, probabilities for one, two or three randomly chosen jets passing the selection rules described in section 6.2 are calculated and listed in Table 6.7.

Table 6.7.: Probabilities for one, two and three jets to have times exceeding two or three sigma.

Number of jets	Number of sigma	Probability to be selected [%]
1	2	2.3
	3	0.14
2	2	0.05
	3	$1.96 \cdot 10^{-4}$
3	2	$1.22 \cdot 10^{-3}$
	3	$2.744 \cdot 10^{-7}$

Note that the listed values are calculated for only one, two or three jets per event and since events mostly contain more than three jets, the values listed in Table 6.7 represent a theoretical minimal selection efficiency.

The selection efficiencies of the rules defined in section 6.2 can be studied by applying the selection rules to the samples introduced in chapter 5. The selection efficiency describes how many percent of all events in a sample are selected. Note that the achievable selection

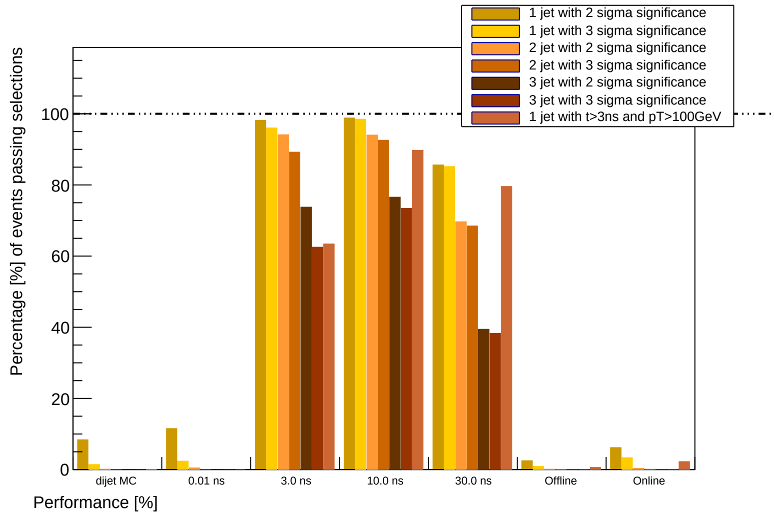

Figure 6.9.: Selection efficiencies of multiple selection rules, compared for different samples.

efficiencies for measured data are most likely worse than the selection efficiencies observed for simulated data. The selection efficiencies for all samples are listed in Tables 6.8, 6.9 and 6.10 and are shown in Figure 6.9.

Selection efficiencies for Monte Carlo samples

Since only the decay simulations and not the detector simulation differ, the selection rule, based on the parameterization derived by the dijet sample, can directly be applied to the LLP samples. Since the LLP samples represent possible signal, comparing the selection efficiencies with the dijet sample gives a first indication of the signal to noise ratio that can be expected. The selection efficiencies are listed in Table 6.8. Note, the simulated samples are the only indicators for the signal to noise ratio available.

For lifetimes of $\tau = 3\,\mathrm{ns}, 10\,\mathrm{ns}, 30\,\mathrm{ns}$, the selection efficiencies are noticeably higher than for the dijet sample. This is expected, since the lifetimes, causing the delays, are clearly higher than the time selection (for $200\,\mathrm{GeV} < p_T \Rightarrow t_{selection} < 1\,\mathrm{ns}$) applied. Plots showing the most significant jet of each event passing the different selection rules, are shown in Appendix B.2.1.

Table 6.8.: Selection efficiencies for simulated samples.

Significance	Number of jets passing	Events passed [%]	Sample
2	1	8.42	dijet MC
	2	0.13	
	3	0.00	
3	1	1.44	
	2	0.00	
	3	0.00	
2	1	11.56	0.01 ns
	2	0.50	
	3	0.00	
3	1	2.40	
	2	0.00	
	3	0.00	
2	1	98.20	3.0 ns
	2	94.15	
	3	73.793	
3	1	96.05	
	2	89.24	
	3	62.53	
2	1	98.85	10.0 ns
	2	94.05	
	3	76.59	
3	1	98.50	
	2	92.60	
	3	73.44	
2	1	85.64	30.0 ns
	2	69.68	
	3	39.47	
3	1	85.19	
	2	68.48	
	3	38.32	

For a lifetime of $\tau = 0.01$ ns, the selection efficiency is even worse than the selection efficiency of the dijet sample. As discussed in section 6.1.1, the parameterization, describing the standard deviations used for the selection, approaches a constant value of approximately $0.2\,\mathrm{ns}$. Therefore, delays of $\mathcal{O}(0.01\,\mathrm{ns})$ are not expected to be noticed, being in great agreement with the observations.

Based on the gluino decay simulated in the LLP samples, two jets with similar delays are expected. Therefore, for all events within the LLP samples, two jets with similar delays are expected. Based on this unique property of LLP samples, the signal (LLP sample) to background (dijet sample) ratio is expected to improve by requiring an event to contain two significant delayed jets. Selection rules of this kind will further be referred to as multiple-jet event selections.

The rejection of dijet events further improves by applying multiple-jets event selections. Since within the dijet sample, significant delayed jets occur randomly, multiple significant delayed jets occurring in one event are even more unlikely. Thus, most events do not pass a multiple-jets event selection, resulting in a nearly perfect event rejection. As expected, the selection efficiency of the $0.01\,\mathrm{ns}$-LLP sample is similar to the selection efficiency of the dijet sample.

Better selection efficiencies are observed for the LLP samples with longer lifetimes. The additional requirement of multiple jets being significantly delayed, caused a loss of events, compared to requirements of single jets being delayed by the same significance. For a lifetime of $30\,\mathrm{ns}$, the performance decreases the most. With a bunch spacing of $25\,\mathrm{ns}$, extremely delayed jets ($t^{\mathrm{jet}}_{\mathrm{true}} = \mathcal{O}(25\,\mathrm{ns})$) can cause difficulties assigning the observed signals to the correct bunch crossing. This results in worse selection efficiencies.

Selection efficiencies for measured and offline reconstructed sample

Up to this analysis, the TDAQ system of the ATLAS detector (section 3.4) does not include any active selections triggering on jet times. As a consequence, all measured and analyzed events passed a selection criterium unrelated to jet times. Therefore, the investigated samples are not biased with regard to jet times and consequently represent the expected background. In order to reject most of the unwanted events, small selection efficiencies are desirable for background processes. Note that, if existing, events containing LLPs or LLP decay products could already be contained in the measured data. The selection efficiencies for applying the selection rules discussed in section 6.2 to the offline reconstructed data are listed in Table 6.9.

Table 6.9.: Selection efficiencies for measured and offline reconstructed data.

Significance	Number of Jets passing	Events passed [%]
2	1	2.53
2	2	0.14
2	3	0.03
3	1	0.91
3	2	0.08
3	3	0.02

With nearly perfect rejection, approximately the same performance as for the dijet sample can be achieved for the offline reconstructed data. This was expected, since the selection rule was determined by the data it was applied to. Nonetheless, the results indicate that the parameterization used is sufficient enough to achieve the desired rejection of the offline reconstructed data. This justifies the assumptions made in section 6.1.2.

Selection efficiencies for measured and online reconstructed sample

As discussed previously, the TDAQ system does not contain any selection rules triggering on delayed jets. Thus, all measured samples investigated in this work are not biased with respect to jet times. As a consequence, for the online data, the time distributions shown in section 5.2.1 represent the complete time spectrum expected during the triggering process. For that reason, the selection efficiencies give an indication of the expected increase in accepted events. The selection efficiencies for the online sample are listed in Table 6.10.

Table 6.10.: Selection efficiencies for measured and online reconstructed data.

Significance	Number of Jets passing	Events passed [%]
2	1	6.21
2	2	0.39
2	3	0.01
3	1	3.36
3	2	0.12
3	3	0.01

Caused by wider jet time distributions and fluctuations of single jet times, the selection efficiencies for the online reconstructed samples are slightly higher than for the offline reconstructed samples. Nonetheless, the selection rules are sufficient to reject most of the events.

7. Implementation of Significance based timing selection

The High-Level Trigger of the ATLAS detector is implemented in the ATLAS software framework Athena. The trigger menu is written in C++ and is set up by using python. As described in section 3.4, selection rules are implemented as hypotheses, deciding whether to keep an event or not. Those decisions are based on reconstructed features, such as the jet times discussed in section 5.2.1 and 6.1.3. The implementation of a hypothesis into a chain is done via a unique string.

In the scope of this work, a new hypothesis is implemented. The new selection rule is based on the outcomes of chapter 6. Specifically, the selection rule requiring one jet exceeding a significance of 3 is implemented. This means that each event passing this selection rule must contain at least one jet with

$$p_T > 100\,\text{GeV}, \tag{7.1}$$

$$\frac{t_{jet}}{\text{ns}} > 3 \cdot e^{-(8.11 \cdot 10^{-1} + 1.43 \cdot 10^{-2} \cdot \frac{p_T}{\text{GeV}})} + 1.81 \cdot 10^{-4} \cdot \frac{p_T}{\text{GeV}} + 8.42 \cdot 10^{-1}. \tag{7.2}$$

This new hypothesis provides sensitivity to new signatures and motivate further investigations of delayed jets.

To add the hypothesis to a Chain, **xtimeSigy** must be included in the string describing a new Chain. **x** stands for the required significance, **y** stands for an upper time limit. By not defining **y**, no upper limit is applied, **x** must be defined.

8. Conclusions and outlook

This work showed that it is possible to create a selection rule based on time significance. Section 6.2 discussed a variety of possibilities with different performances and justifications to be implemented, as described in section 6.3. Based on those results, a new hypothesis was implemented into the Athena framework of the ATLAS trigger system. The studies in this thesis and the new hypothesis allow the development of new selection rules triggering on delayed jets. While there is still room for improvement, the new hypothesis works as intended and will be used in future runs to trigger on delayed jets, laying the foundation for a new signature for LLP searches.

Outlook

This study has proven the feasibility of a significance-based trigger selection rule. At the same time, it showed its limits, giving rise to many possible improvements. Already chapter 5 indicates that the resolution of online reconstruction has room for improvement. The way of calculating jet times could be improved to minimize the spread. Also, a more detailed study of pile-up jet times could improve the discrimination between those and delayed jets caused by LLPs.

As discussed in chapter 6, the parameterization is based on assumptions that the time distributions can be described by Gaussian functions and that their standard deviations depend exponentially on p_T. Those assumptions could be refind, leading to an improved parameterization and better selection efficiencies. It is possible that the time reconstruction accuracy is not only dependent on the transverse momentum, but also on other parameters, such as the pseudo rapidity. The dependence on different parameters could be studied.

To get a better indication of the lifetime and mass combinations the selection rules are sensitive to, more simulated LLP samples could be studied. Also, samples with a different process producing LLPs could be investigated. This would prevent the selection rule from being tailored to decay specific properties and model parameters.

As discussed in sections 6.2 and 6.3, a variety of different combinations of significance and transverse momentum requirements can be used to trigger on delayed jets. A more detailed study comparing different significance-based selection rules could improve the signal-to-noise ratio and help to better match the hardware limitations.

As mentioned in chapter 7, an upper time limit can be added to the new time significance hypothesis. A further study could investigate the influence of such an upper time limit.

A variation in the characteristics of the jet time reconstruction, such as the observed exponential function, could cause a significant variation in the event acceptance rate. To limit the influence of varying parameters, online monitoring and adjustments based on its results could be implemented.

Bibliography

[1] Andrew J. Larkoski. *Elementary particle physics: An intuitive introduction*. Cambridge University Press, 2019.

[2] Lawrence Lee et al. "Collider searches for long-lived particles beyond the Standard Model". In: *Progress in Particle and Nuclear Physics* 106 (May 2019), pp. 210–255. DOI: 10.1016/j.ppnp.2019.02.006. URL: https://doi.org/10.1016%5C%2Fj.ppnp.2019.02.006.

[3] "The CMS experiment at the CERN LHC. The Compact Muon Solenoid experiment". In: *JINST* 3 (2008). Also published by CERN Geneva in 2010, S08004. 361 p. DOI: 10.1088/1748-0221/3/08/S08004. URL: https://cds.cern.ch/record/1129810.

[4] "The ATLAS Experiment at the CERN Large Hadron Collider". In: *JINST* 3 (2008). Also published by CERN Geneva in 2010, S08003. 437 p. DOI: 10.1088/1748-0221/3/08/S08003. URL: https://cds.cern.ch/record/1129811.

[5] "Search for long-lived particles using nonprompt jets and missing transverse momentum with proton-proton collisions at $\sqrt{s} = 13\,\mathrm{TeV}$". In: *Physics Letters B* 797 (Oct. 2019), p. 134876. DOI: 10.1016/j.physletb.2019.134876. URL: https://doi.org/10.1016%5C%2Fj.physletb.2019.134876.

[6] David J. Griffiths. *Introduction to elementary particles*. Wiley-VCH, 2017.

[7] Gordon L. Kane. "Supersymmetry: What? why? when?" In: *Contemporary Physics* 41.6 (2000), pp. 359–367. DOI: 10.1080/00107510010001644. eprint: https://doi.org/10.1080/00107510010001644. URL: https://doi.org/10.1080/00107510010001644.

[8] Adel Bilal. *Introduction to Supersymmetry*. 2001. arXiv: hep-th/0101055 [hep-th].

[9] CSABA CSÁKI. "THE MINIMAL SUPERSYMMETRIC STANDARD MODEL". In: *Modern Physics Letters A* 11.08 (Mar. 1996), pp. 599–613. DOI: 10.1142/s021773239600062x. URL: https://doi.org/10.1142%5C%2Fs021773239600062x.

[10] STEPHEN P. MARTIN. “A SUPERSYMMETRY PRIMER”. In: *Perspectives on Supersymmetry*. WORLD SCIENTIFIC, July 1998, pp. 1–98. DOI: 10.1142/9789812839657_0001. URL: https://doi.org/10.1142%5C%2F9789812839657_0001.

[11] Luc Pape and Daniel Treille. “Supersymmetry facing experiment: much ado (already) about nothing (yet)”. In: *Reports on Progress in Physics* 69.11 (Nov. 2006), R01. DOI: 10.1088/0034-4885/69/11/R01. URL: https://dx.doi.org/10.1088/0034-4885/69/11/R01.

[12] G.F. Giudice and A. Romanino. “Erratum to: “Split supersymmetry” [Nucl. Phys. B 699 (2004) 65]”. In: *Nuclear Physics B* 706.1-2 (Jan. 2005), p. 487. DOI: 10.1016/j.nuclphysb.2004.11.048. URL: https://doi.org/10.1016%5C%2Fj.nuclphysb.2004.11.048.

[13] JoAnne L. Hewett et al. “Signatures of long-lived gluinos in split supersymmetry”. In: *Journal of High Energy Physics* 2004.09 (Oct. 2004), p. 070. DOI: 10.1088/1126-6708/2004/09/070. URL: https://dx.doi.org/10.1088/1126-6708/2004/09/070.

[14] Asimina Arvanitaki et al. “Limits on split supersymmetry from gluino cosmology”. In: *Physical Review D* (Oct. 2005). DOI: 10.1103/physrevd.72.075011. URL: https://doi.org/10.1103%5C%2Fphysrevd.72.075011.

[15] J. T. Boyd. *LHC Run-2 and Future Prospects*. 2020. DOI: 10.48550/ARXIV.2001.04370. URL: https://arxiv.org/abs/2001.04370.

[16] R Calaga et al. *Long Range Beam-beam Effects in the LHC*. en. 2014. DOI: 10.5170/CERN-2014-004.87. URL: http://cds.cern.ch/record/1953724.

[17] Lyndon Evans and Philip Bryant. “LHC Machine”. In: *Journal of Instrumentation* 3.08 (Aug. 2008), S08001–S08001. DOI: 10.1088/1748-0221/3/08/s08001. URL: https://doi.org/10.1088/1748-0221/3/08/s08001.

[18] The ATLAS collaboration. “Operation of the ATLAS trigger system in Run 2”. In: *Journal of Instrumentation* 15.10 (Oct. 2020), P10004–P10004. DOI: 10.1088/1748-0221/15/10/p10004. URL: https://doi.org/10.1088%5C%2F1748-0221%5C%2F15%5C%2F10%5C%2Fp10004.

[19] ATLAS Collaboration. *Athena*. Version 22.0.1. Apr. 2019. DOI: 10.5281/zenodo.2641997. URL: https://doi.org/10.5281/zenodo.2641997.

[20] Christian Ohm. “Searches for exotic stable massive particles with the ATLAS experiment”. Presented 04 Nov 2011. 2011. URL: https://cds.cern.ch/record/1397376.

[21] Matteo Cacciari, Gavin P Salam, and Gregory Soyez. “The anti-ik/isubit/i/subjet clustering algorithm”. In: *Journal of High Energy Physics* 2008.04 (Apr. 2008), pp. 063–063. DOI: 10.1088/1126-6708/2008/04/063. URL: https://doi.org/10.1088%5C%2F1126-6708%5C%2F2008%5C%2F04%5C%2F063.

[22] “Topological cell clustering in the ATLAS calorimeters and its performance in LHC Run 1”. In: *The European Physical Journal C* 77.7 (July 2017). DOI: 10.1140/epjc/s10052-017-5004-5. URL: https://doi.org/10.1140%5C%2Fepjc%5C%2Fs10052-017-5004-5.

[23] “Jet energy measurement with the ATLAS detector in proton-proton collisions at $\sqrt{s} = 7$ TeV”. In: *The European Physical Journal C* 73.3 (Mar. 2013). DOI: 10.1140/epjc/s10052-013-2304-2. URL: https://doi.org/10.1140%5C%2Fepjc%5C%2Fs10052-013-2304-2.

[24] Torbjörn Sjöstrand, Stephen Mrenna, and Peter Skands. “PYTHIA 6.4 physics and manual”. In: *Journal of High Energy Physics* 2006.05 (May 2006), pp. 026–026. DOI: 10.1088/1126-6708/2006/05/026. URL: https://doi.org/10.1088%5C%2F1126-6708%5C%2F2006%5C%2F05%5C%2F026.

[25] Johan Alwall et al. “MadGraph 5: going beyond”. In: *Journal of High Energy Physics* 2011.6 (June 2011). DOI: 10.1007/jhep06(2011)128. URL: https://doi.org/10.1007%5C%2Fjhep06%5C%282011%5C%29128.

[26] Hartmann, Nikolai et al. “Columnar data analysis with ATLAS analysis formats”. In: *EPJ Web Conf.* 251 (2021), p. 03001. DOI: 10.1051/epjconf/202125103001. URL: https://doi.org/10.1051/epjconf/202125103001.

[27] Rene Brun et al. *root-project/root: v6.18/02*. Version v6-18-02. Aug. 2019. DOI: 10.5281/zenodo.3895860. URL: https://doi.org/10.5281/zenodo.3895860.

[28] “Search for new phenomena in dijet mass and angular distributions from pp collisions at $\sqrt{s} = 13$ TeV with the ATLAS detector”. In: *Physics Letters B* 754 (Mar. 2016), pp. 302–322. DOI: 10.1016/j.physletb.2016.01.032. URL: https://doi.org/10.1016%5C%2Fj.physletb.2016.01.032.

A. Studies of jet time measurements

A.1. Jet time analysis of MC simulated samples

A.1.1. LLP 0.01ns sample

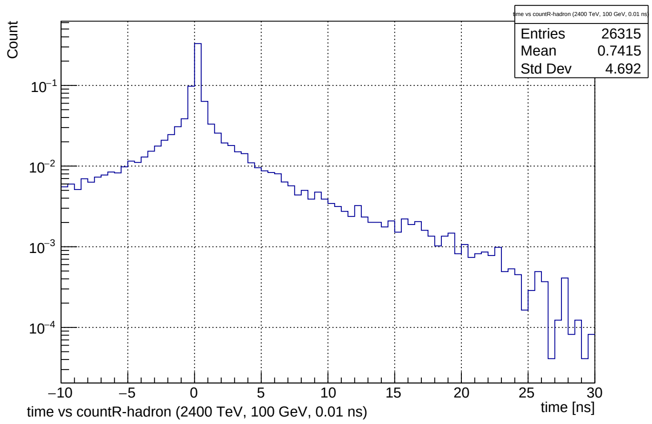

Figure A.1.: Histogram with bin width of $\Delta t = 0.5\,\mathrm{ns}$. Despite LLP physics simulated, background events create a peak at at $0\,\mathrm{ns}$

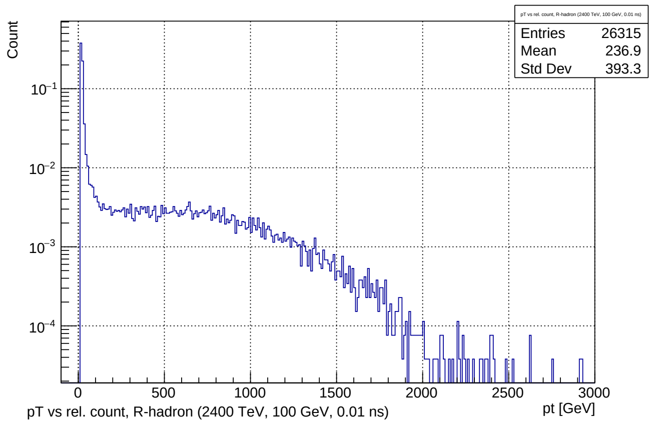

Figure A.2.: Pile-up peak at low transverse momentum. Slowly decreasing amount of jets, for transverse momenta above $p_T \approx 200\,\mathrm{GeV}$.

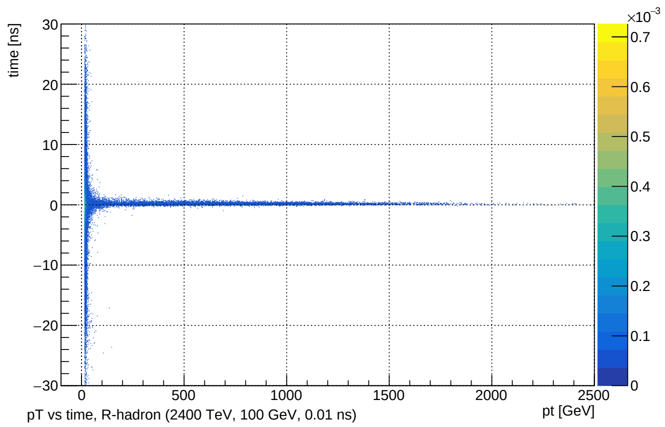

Figure A.3.: Time vs. p_T for LLP ($0.01\,\mathrm{ns}$) sample jets. The color scheme represents the density of jets in different areas.

A.1.2. LLP 10ns sample

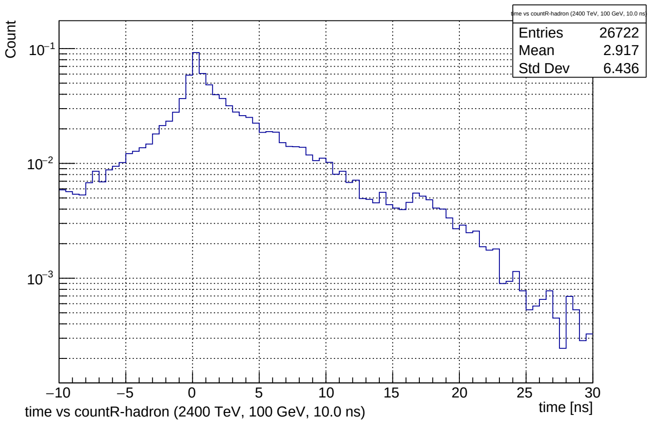

Figure A.4.: Histogram with bin width of $\Delta t = 0.5\,\mathrm{ns}$. Despite LLP physics simulated, background events create a peak at at $0\,\mathrm{ns}$

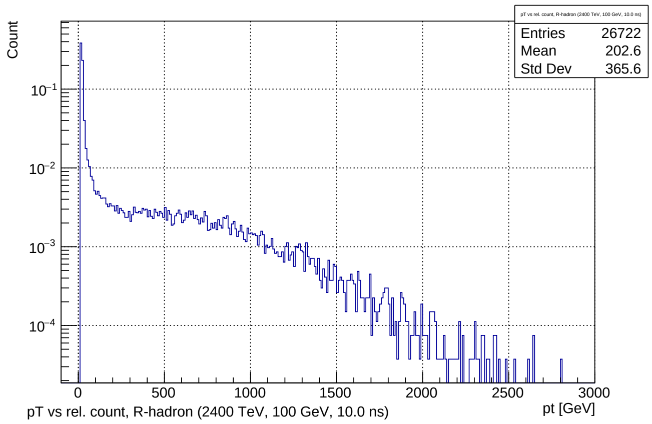

Figure A.5.: Pile-up peak at low transverse momentum. Slowly decreasing amount of jets, for transverse momenta above $p_T \approx 200\,\mathrm{GeV}$.

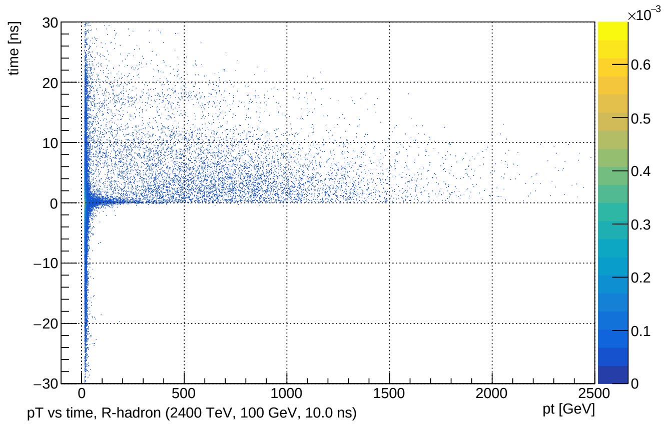

Figure A.6.: Time vs. p_T for LLP ($10\,\mathrm{ns}$) sample jets. The color scheme represents the density of jets in different areas.

A.1.3. LLP 30ns sample

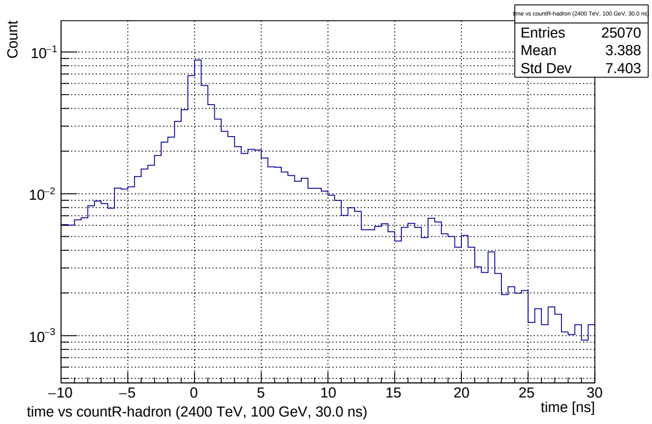

Figure A.7.: Histogram with bin width of $\Delta t = 0.5\,\mathrm{ns}$. Despite LLP physics simulated, background events create a peak at at $0\,\mathrm{ns}$

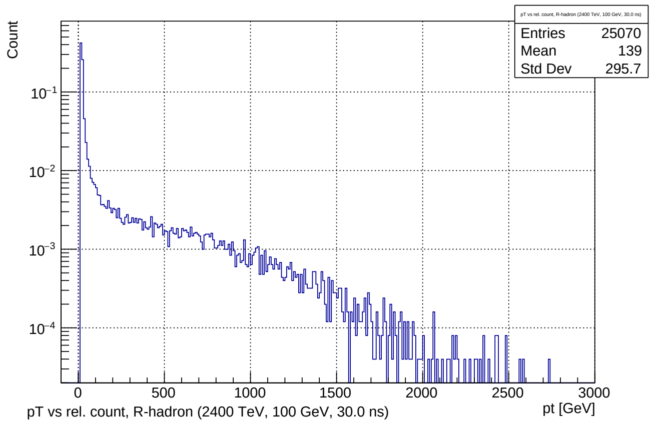

Figure A.8.: Pile-up peak at low transverse momentum. Slowly decreasing amount of jets, for transverse momenta above $p_T \approx 200\,\mathrm{GeV}$.

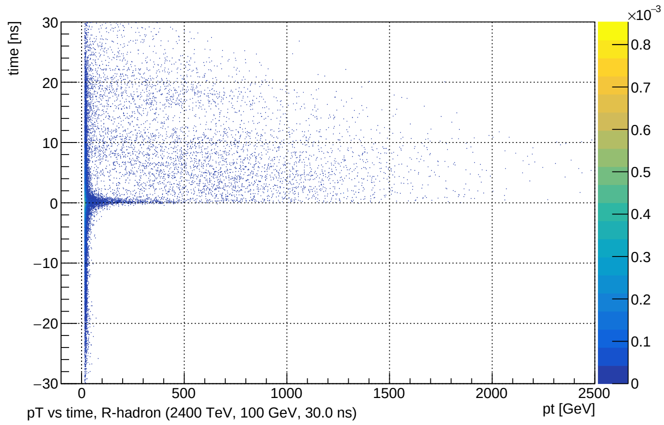

Figure A.9.: Time vs. p_T for LLP ($30\,\mathrm{ns}$) sample jets. The color scheme represents the density of jets in different areas.

B. Designing a trigger algorithm based on jet timing

B.1. Correlation between transverse momentum and timing

B.1.1. MC simulated and offline reconstructed jets

Time distributions

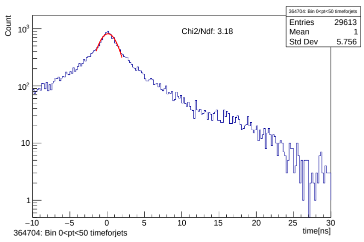

(a) Time distribution of bin $0\,\text{GeV} < p_T < 50\,\text{GeV}$ for dijet sample.

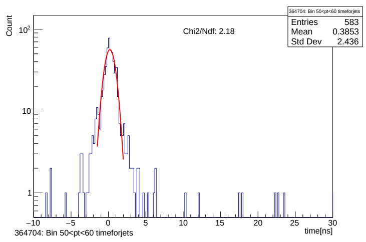

(b) Time distribution of bin $50\,\text{GeV} < p_T < 60\,\text{GeV}$ for dijet sample.

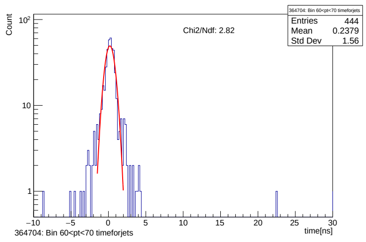

(c) Time distribution of bin $60\,\text{GeV} < p_T < 70\,\text{GeV}$ for dijet sample.

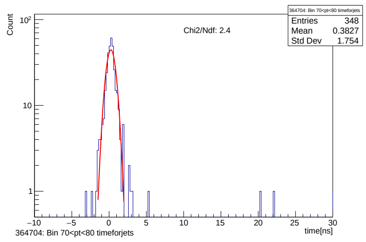

(d) Time distribution of bin $70\,\text{GeV} < p_T < 80\,\text{GeV}$ for dijet sample.

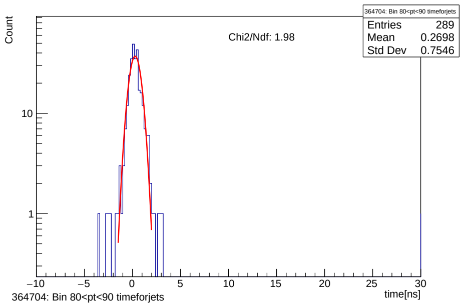

(a) Time distribution of bin $80\,\text{GeV} < p_T < 90\,\text{GeV}$ for dijet sample.

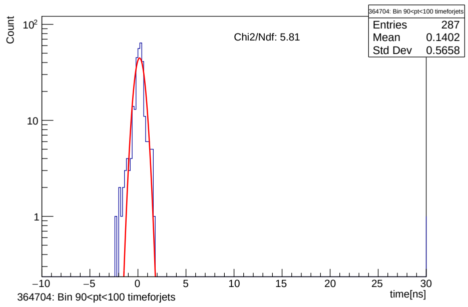

(b) Time distribution of bin $90\,\text{GeV} < p_T < 100\,\text{GeV}$ for dijet sample.

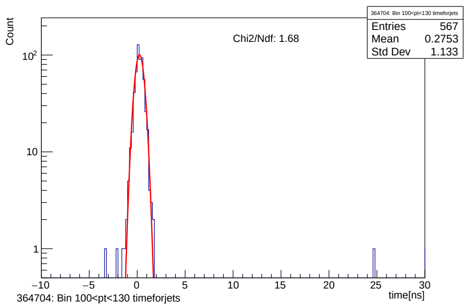

(c) Time distribution of bin $100\,\text{GeV} < p_T < 130\,\text{GeV}$ for dijet sample.

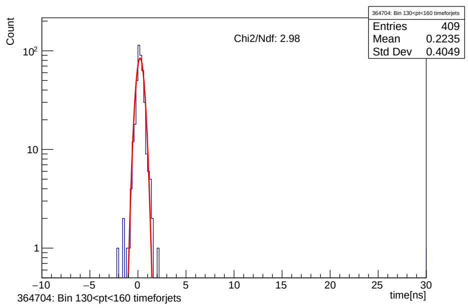

(d) Time distribution of bin $130\,\text{GeV} < p_T < 160\,\text{GeV}$ for dijet sample.

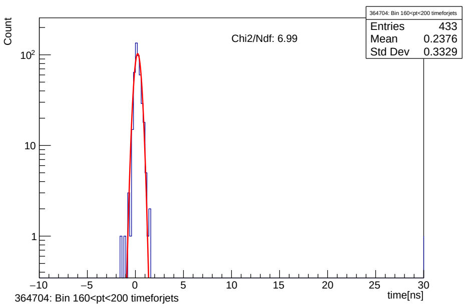

(e) Time distribution of bin $160\,\text{GeV} < p_T < 200\,\text{GeV}$ for dijet sample.

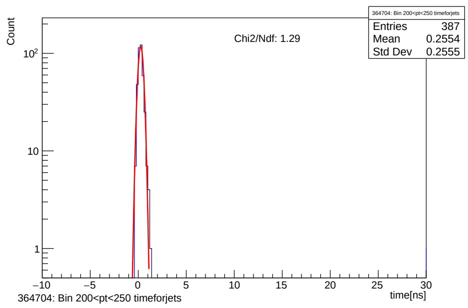

(f) Time distribution of bin $200\,\text{GeV} < p_T < 250\,\text{GeV}$ for dijet sample.

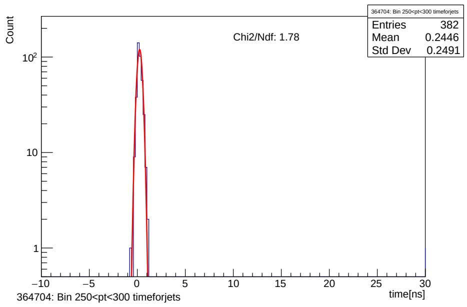

(a) Time distribution of bin $250\,\text{GeV} < p_T < 300\,\text{GeV}$ for dijet sample.

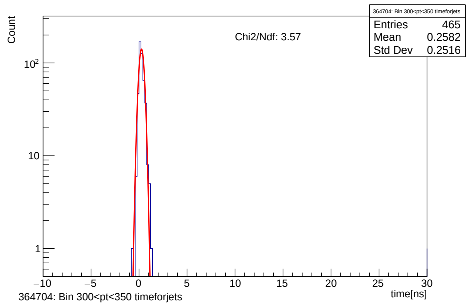

(b) Time distribution of bin $300\,\text{GeV} < p_T < 350\,\text{GeV}$ for dijet sample.

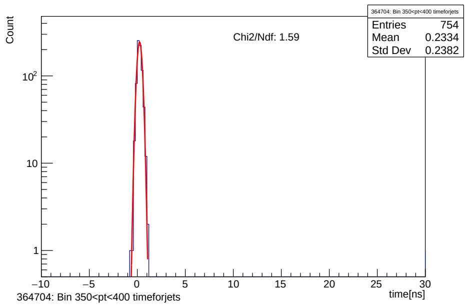

(c) Time distribution of bin $350\,\text{GeV} < p_T < 400\,\text{GeV}$ for dijet sample.

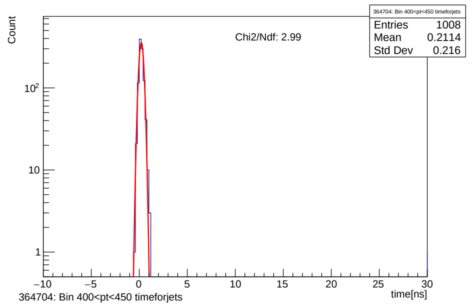

(d) Time distribution of bin $400\,\text{GeV} < p_T < 450\,\text{GeV}$ for dijet sample.

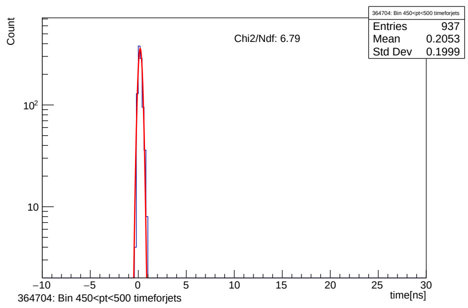

(e) Time distribution of bin $450\,\text{GeV} < p_T < 500\,\text{GeV}$ for dijet sample.

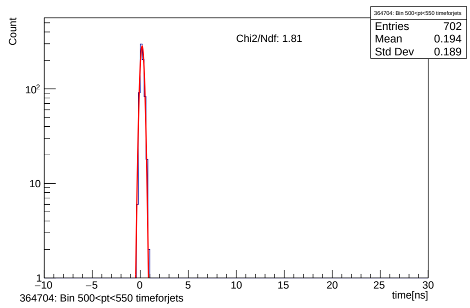

(f) Time distribution of bin $500\,\text{GeV} < p_T < 550\,\text{GeV}$ for dijet sample.

Transverse momentum distributions

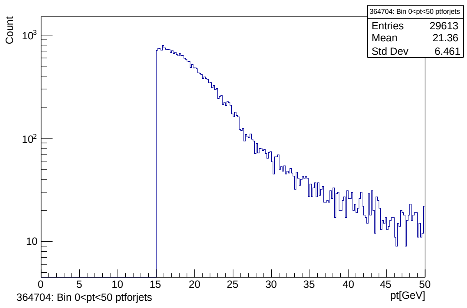

(a) p_T distribution of bin $0\,\mathrm{GeV} < p_T < 50\,\mathrm{GeV}$ for dijet sample.

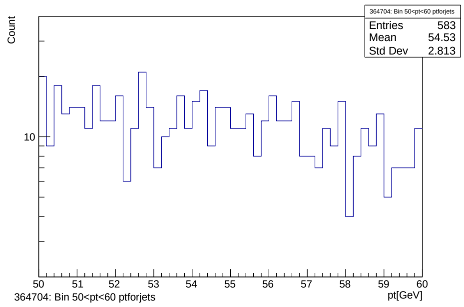

(b) p_T distribution of bin $50\,\mathrm{GeV} < p_T < 60\,\mathrm{GeV}$ for dijet sample.

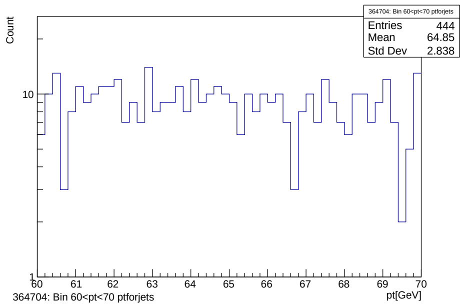

(c) p_T distribution of bin $60\,\mathrm{GeV} < p_T < 70\,\mathrm{GeV}$ for dijet sample.

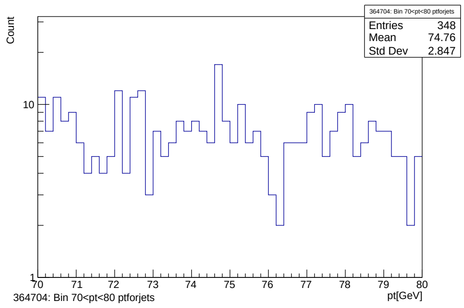

(d) p_T distribution of bin $70\,\mathrm{GeV} < p_T < 80\,\mathrm{GeV}$ for dijet sample.

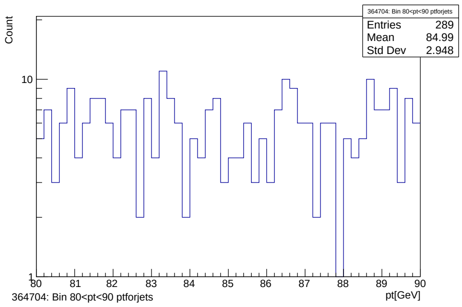

(a) p_T distribution of bin $80\,\text{GeV} < p_T < 90\,\text{GeV}$ for dijet sample.

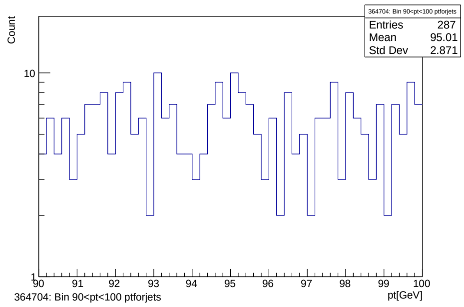

(b) p_T distribution of bin $90\,\text{GeV} < p_T < 100\,\text{GeV}$ for dijet sample.

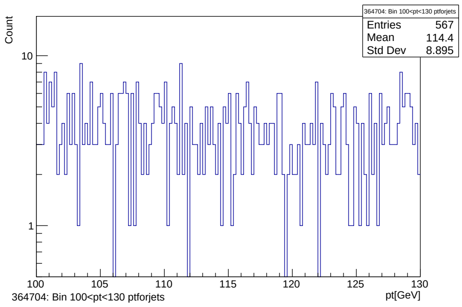

(c) p_T distribution of bin $100\,\text{GeV} < p_T < 130\,\text{GeV}$ for dijet sample.

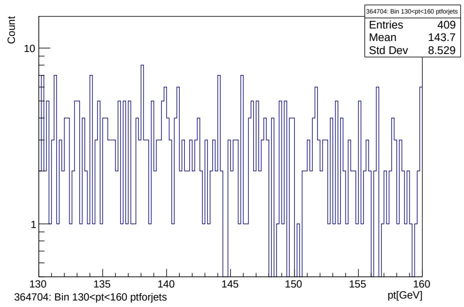

(d) p_T distribution of bin $130\,\text{GeV} < p_T < 160\,\text{GeV}$ for dijet sample.

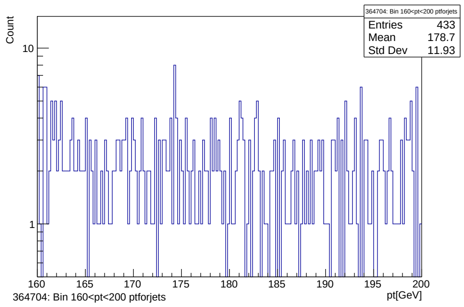

(e) p_T distribution of bin $160\,\text{GeV} < p_T < 200\,\text{GeV}$ for dijet sample.

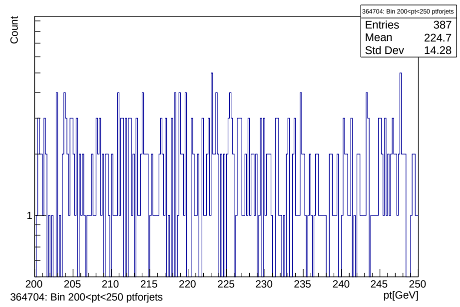

(f) p_T distribution of bin $200\,\text{GeV} < p_T < 250\,\text{GeV}$ for dijet sample.

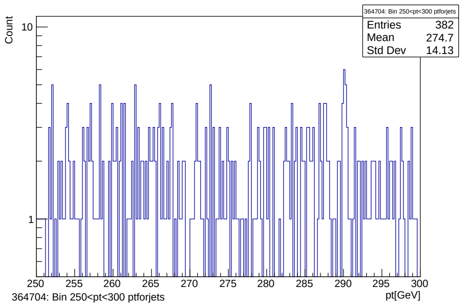

(a) p_T distribution of bin $250\,\text{GeV} < p_T < 300\,\text{GeV}$ for dijet sample.

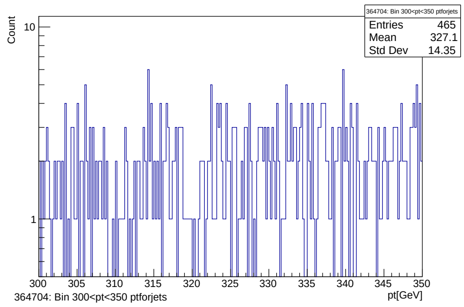

(b) p_T distribution of bin $300\,\text{GeV} < p_T < 350\,\text{GeV}$ for dijet sample.

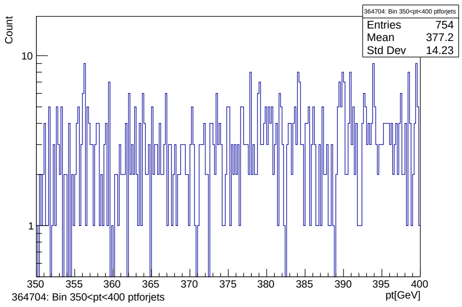

(c) p_T distribution of bin $350\,\text{GeV} < p_T < 400\,\text{GeV}$ for dijet sample.

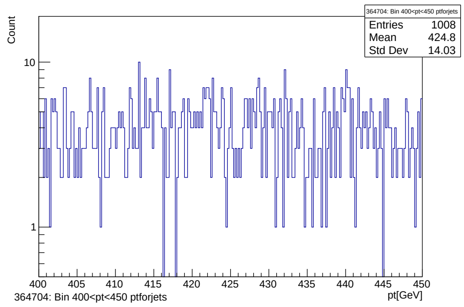

(d) p_T distribution of bin $400\,\text{GeV} < p_T < 450\,\text{GeV}$ for dijet sample.

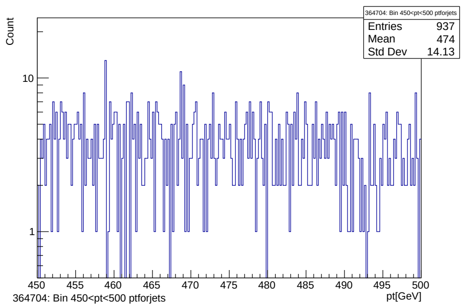

(e) p_T distribution of bin $450\,\text{GeV} < p_T < 500\,\text{GeV}$ for dijet sample.

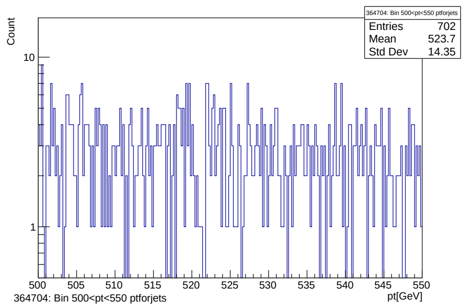

(f) p_T distribution of bin $500\,\text{GeV} < p_T < 550\,\text{GeV}$ for dijet sample.

B.1.2. Measured and offline reconstructed jets

Time distributions

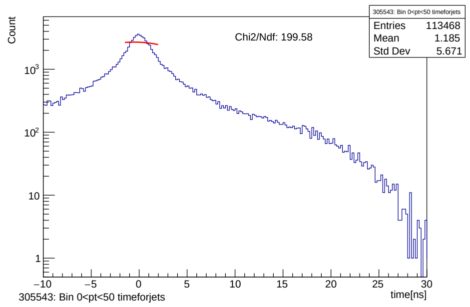

(a) Time distribution of bin $0\,\mathrm{GeV} < p_T < 50\,\mathrm{GeV}$ for offline sample.

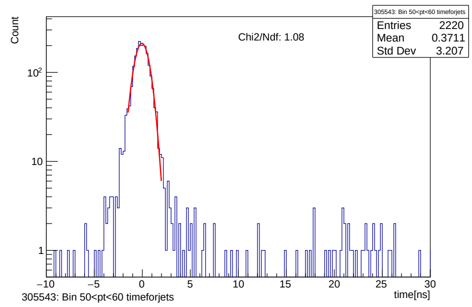

(b) Time distribution of bin $50\,\mathrm{GeV} < p_T < 60\,\mathrm{GeV}$ for offline sample.

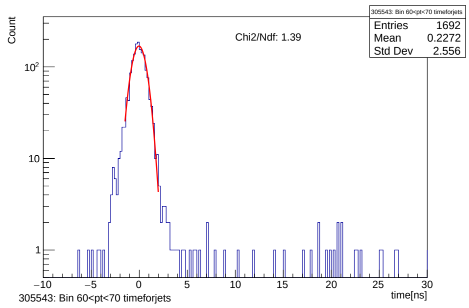

(c) Time distribution of bin $60\,\mathrm{GeV} < p_T < 70\,\mathrm{GeV}$ for offline sample.

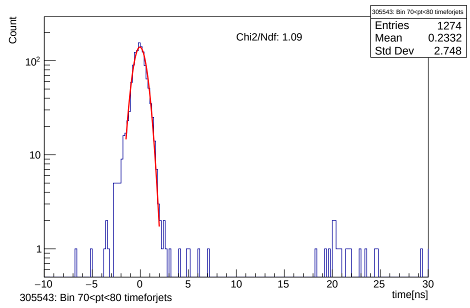

(d) Time distribution of bin $70\,\mathrm{GeV} < p_T < 80\,\mathrm{GeV}$ for offline sample.

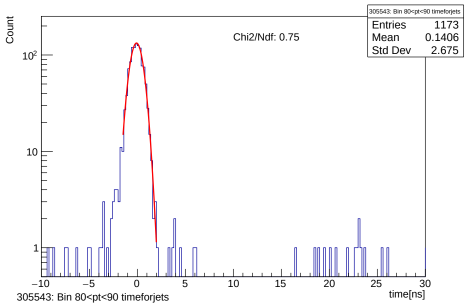

(a) Time distribution of bin $80\,\mathrm{GeV} < p_T < 90\,\mathrm{GeV}$ for offline sample.

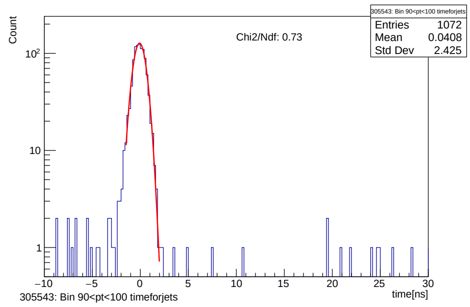

(b) Time distribution of bin $90\,\mathrm{GeV} < p_T < 100\,\mathrm{GeV}$ for offline sample.

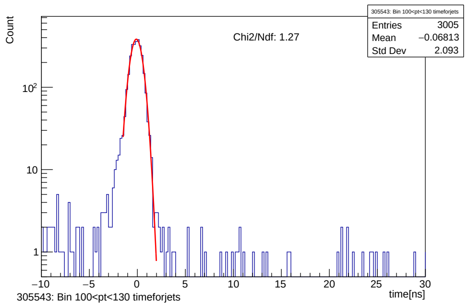

(c) Time distribution of bin $100\,\mathrm{GeV} < p_T < 130\,\mathrm{GeV}$ for offline sample.

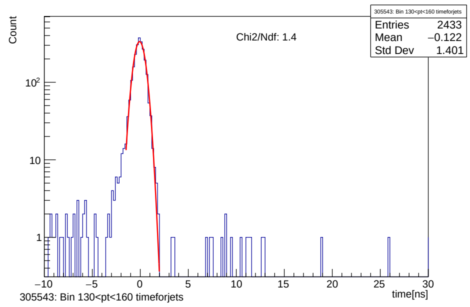

(d) Time distribution of bin $130\,\mathrm{GeV} < p_T < 160\,\mathrm{GeV}$ for offline sample.

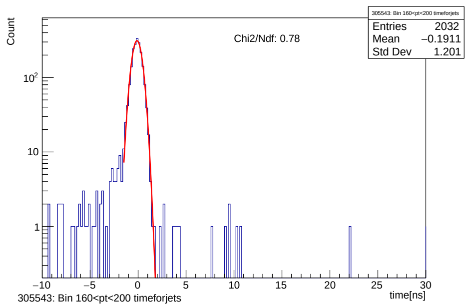

(e) Time distribution of bin $160\,\mathrm{GeV} < p_T < 200\,\mathrm{GeV}$ for offline sample.

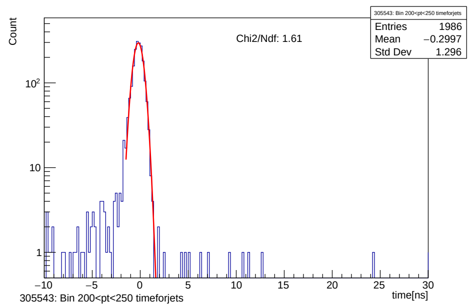

(f) Time distribution of bin $200\,\mathrm{GeV} < p_T < 250\,\mathrm{GeV}$ for offline sample.

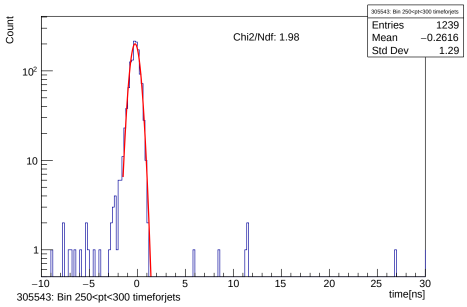

(a) Time distribution of bin $250\,\text{GeV} < p_T < 300\,\text{GeV}$ for offline sample.

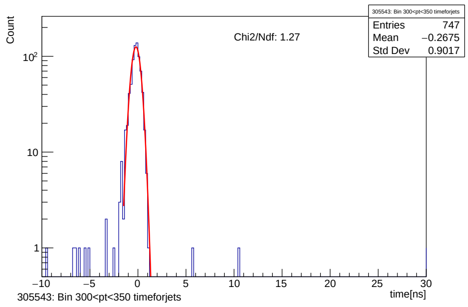

(b) Time distribution of bin $300\,\text{GeV} < p_T < 350\,\text{GeV}$ for offline sample.

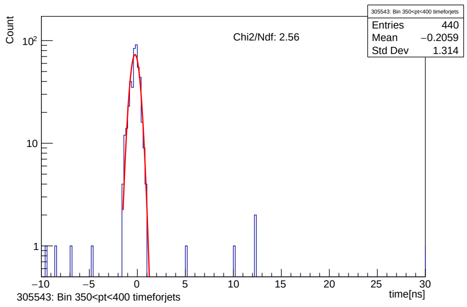

(c) Time distribution of bin $350\,\text{GeV} < p_T < 400\,\text{GeV}$ for offline sample.

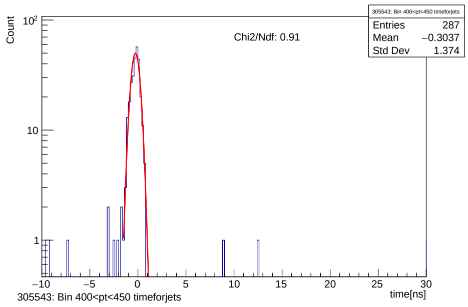

(d) Time distribution of bin $400\,\text{GeV} < p_T < 450\,\text{GeV}$ for offline sample.

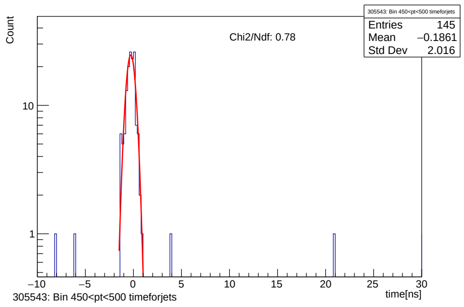

(e) Time distribution of bin $450\,\text{GeV} < p_T < 500\,\text{GeV}$ for offline sample.

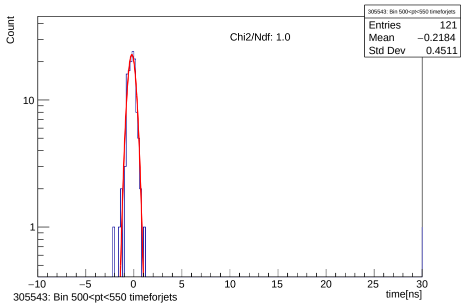

(f) Time distribution of bin $500\,\text{GeV} < p_T < 550\,\text{GeV}$ for offline sample.

Transverse momentum distributions

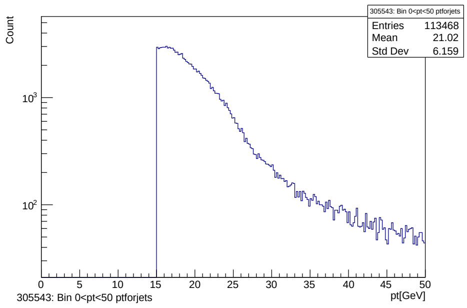

(a) p_T distribution of bin $0\,\text{GeV} < p_T < 50\,\text{GeV}$ for offline sample.

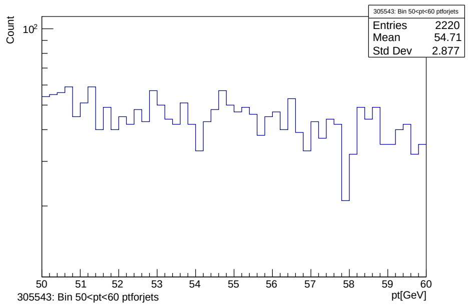

(b) p_T distribution of bin $50\,\text{GeV} < p_T < 60\,\text{GeV}$ for offline sample.

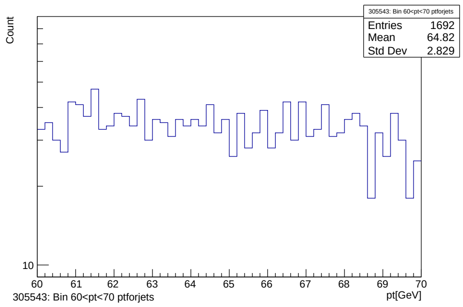

(c) p_T distribution of bin $60\,\text{GeV} < p_T < 70\,\text{GeV}$ for offline sample.

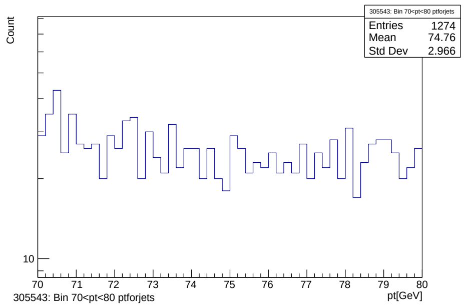

(d) p_T distribution of bin $70\,\text{GeV} < p_T < 80\,\text{GeV}$ for offline sample.

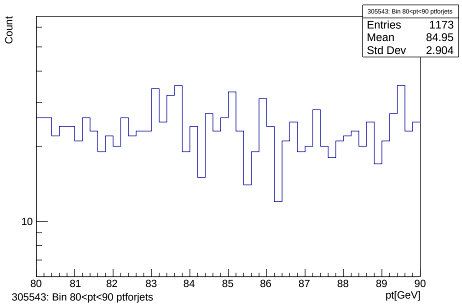

(a) p_T distribution of bin $80\,\mathrm{GeV} < p_T < 90\,\mathrm{GeV}$ for offline sample.

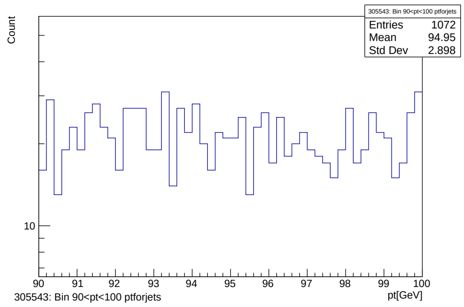

(b) p_T distribution of bin $90\,\mathrm{GeV} < p_T < 100\,\mathrm{GeV}$ for offline sample.

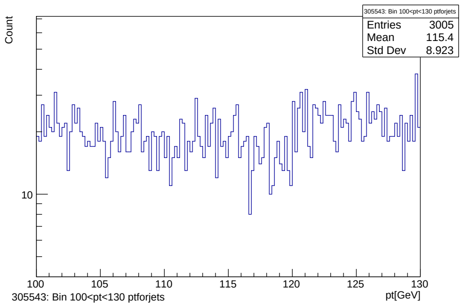

(c) p_T distribution of bin $100\,\mathrm{GeV} < p_T < 130\,\mathrm{GeV}$ for offline sample.

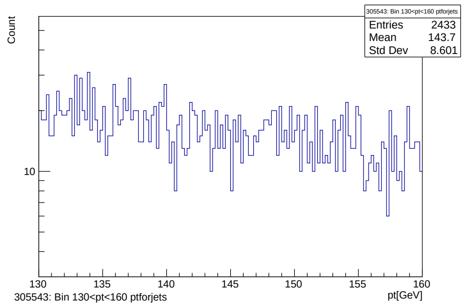

(d) p_T distribution of bin $130\,\mathrm{GeV} < p_T < 160\,\mathrm{GeV}$ for offline sample.

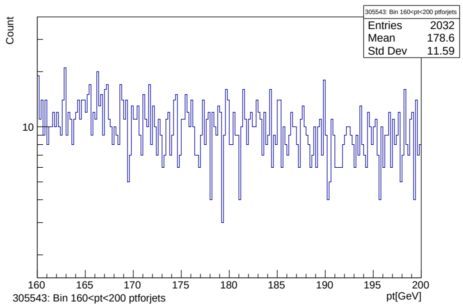

(e) p_T distribution of bin $160\,\mathrm{GeV} < p_T < 200\,\mathrm{GeV}$ for offline sample.

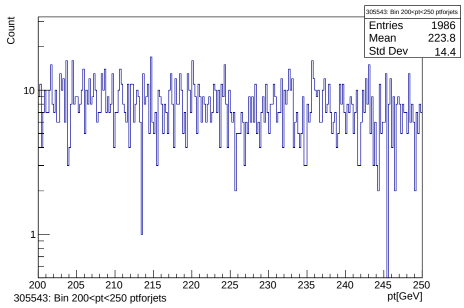

(f) p_T distribution of bin $200\,\mathrm{GeV} < p_T < 250\,\mathrm{GeV}$ for offline sample.

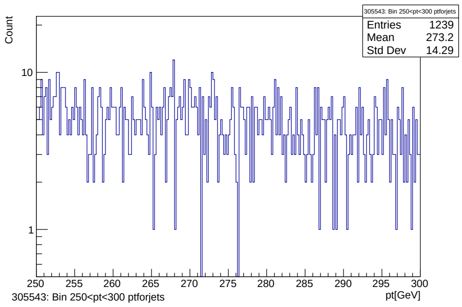

(a) p_T distribution of bin $250\,\text{GeV} < p_T < 300\,\text{GeV}$ for offline sample.

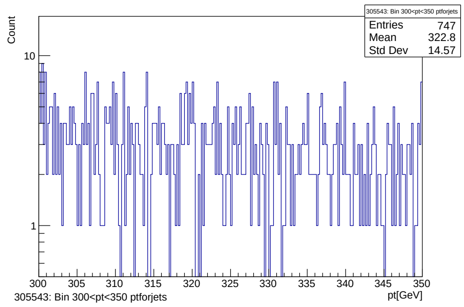

(b) p_T distribution of bin $300\,\text{GeV} < p_T < 350\,\text{GeV}$ for offline sample.

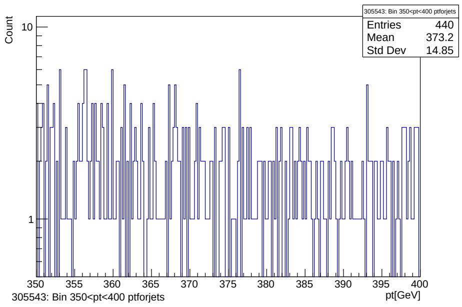

(c) p_T distribution of bin $350\,\text{GeV} < p_T < 400\,\text{GeV}$ for offline sample.

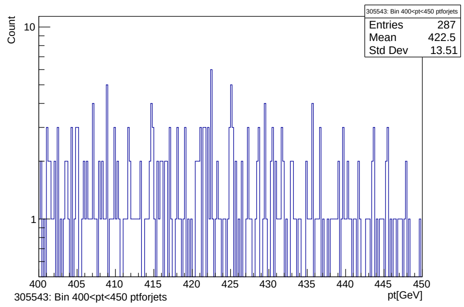

(d) p_T distribution of bin $400\,\text{GeV} < p_T < 450\,\text{GeV}$ for offline sample.

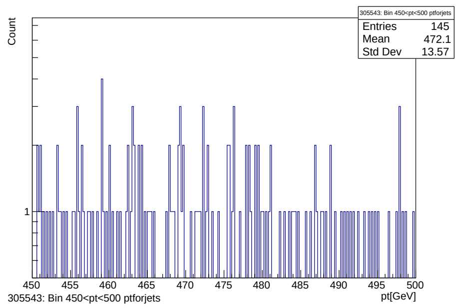

(e) p_T distribution of bin $450\,\text{GeV} < p_T < 500\,\text{GeV}$ for offline sample.

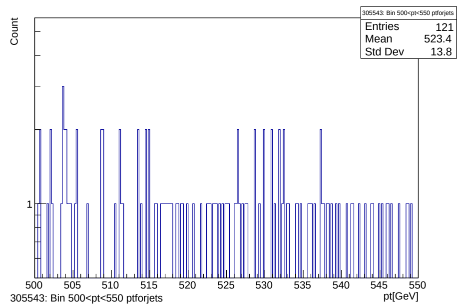

(f) p_T distribution of bin $500\,\text{GeV} < p_T < 550\,\text{GeV}$ for offline sample.

B.1.3. Measured and online reconstructed jets

Time distributions

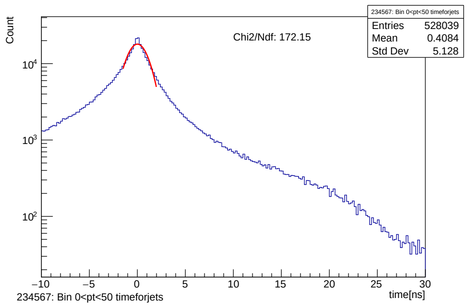

(a) Time distribution of bin $0\,\mathrm{GeV} < p_T < 50\,\mathrm{GeV}$ for online sample.

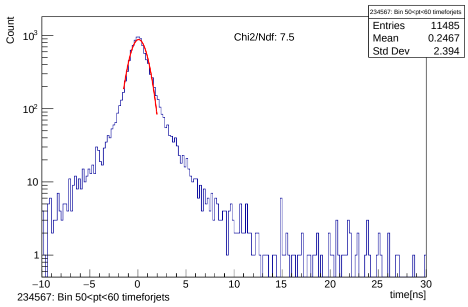

(b) Time distribution of bin $50\,\mathrm{GeV} < p_T < 60\,\mathrm{GeV}$ for online sample.

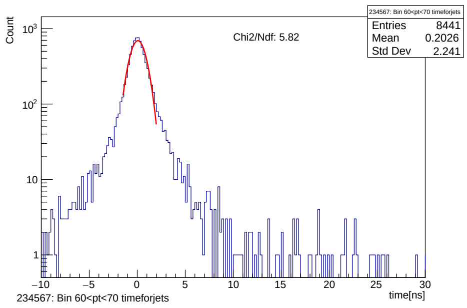

(c) Time distribution of bin $60\,\mathrm{GeV} < p_T < 70\,\mathrm{GeV}$ for online sample.

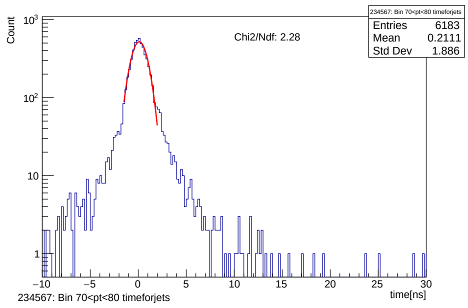

(d) Time distribution of bin $70\,\mathrm{GeV} < p_T < 80\,\mathrm{GeV}$ for online sample.

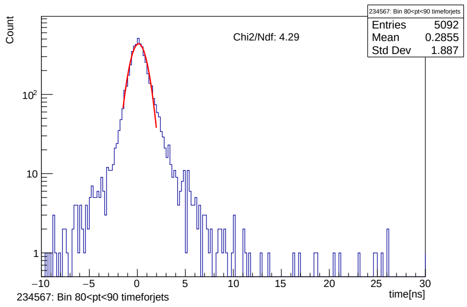

(a) Time distribution of bin $80\,\mathrm{GeV} < p_T < 90\,\mathrm{GeV}$ for online sample.

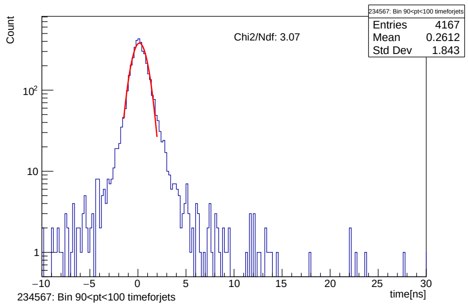

(b) Time distribution of bin $90\,\mathrm{GeV} < p_T < 100\,\mathrm{GeV}$ for online sample.

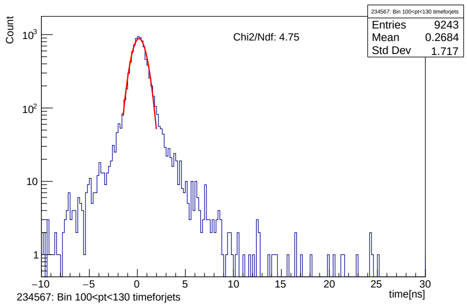

(c) Time distribution of bin $100\,\mathrm{GeV} < p_T < 130\,\mathrm{GeV}$ for online sample.

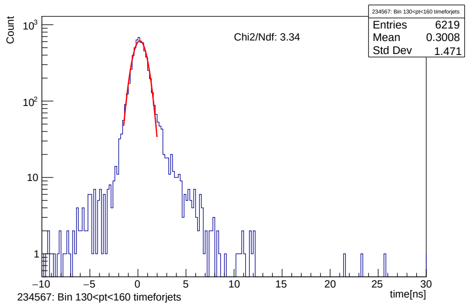

(d) Time distribution of bin $130\,\mathrm{GeV} < p_T < 160\,\mathrm{GeV}$ for online sample.

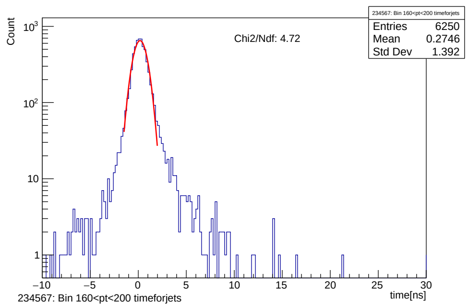

(e) Time distribution of bin $160\,\mathrm{GeV} < p_T < 200\,\mathrm{GeV}$ for online sample.

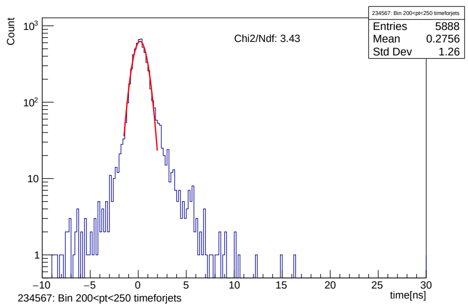

(f) Time distribution of bin $200\,\mathrm{GeV} < p_T < 250\,\mathrm{GeV}$ for online sample.

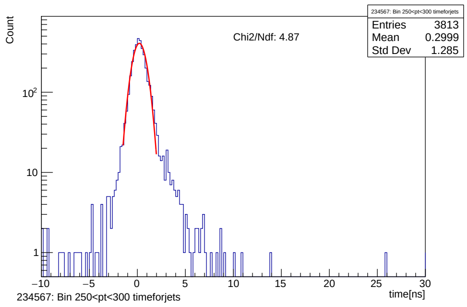

(a) Time distribution of bin $250\,\text{GeV} < p_T < 300\,\text{GeV}$ for online sample.

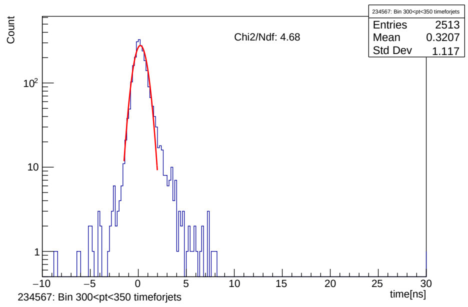

(b) Time distribution of bin $300\,\text{GeV} < p_T < 350\,\text{GeV}$ for online sample.

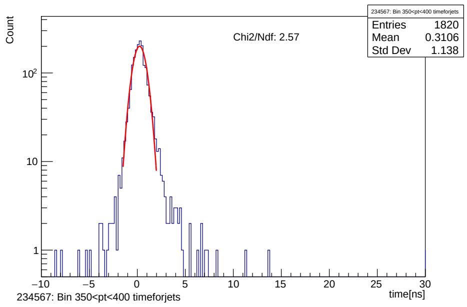

(c) Time distribution of bin $350\,\text{GeV} < p_T < 400\,\text{GeV}$ for online sample.

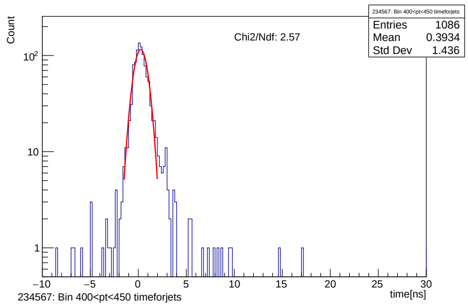

(d) Time distribution of bin $400\,\text{GeV} < p_T < 450\,\text{GeV}$ for online sample.

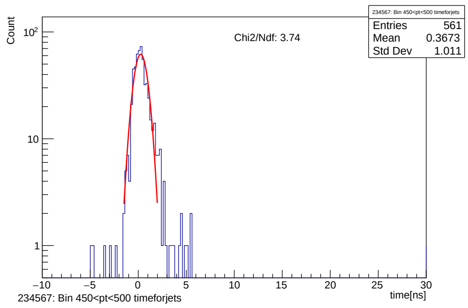

(e) Time distribution of bin $450\,\text{GeV} < p_T < 500\,\text{GeV}$ for online sample.

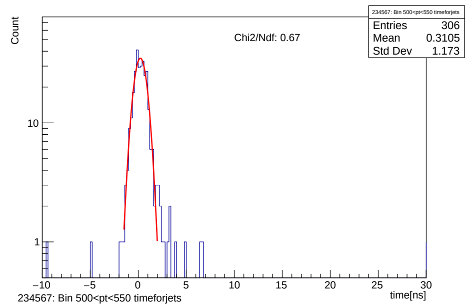

(f) Time distribution of bin $500\,\text{GeV} < p_T < 550\,\text{GeV}$ for online sample.

Transverse momentum distributions

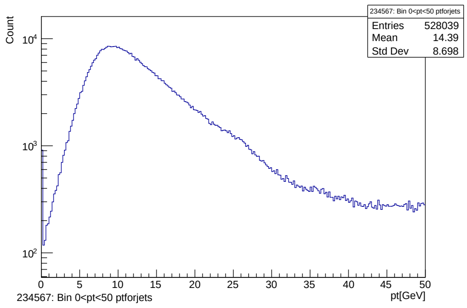

(a) p_T distribution of bin $0\,\text{GeV} < p_T < 50\,\text{GeV}$ for online sample.

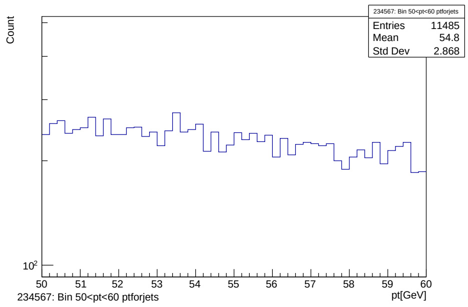

(b) p_T distribution of bin $50\,\text{GeV} < p_T < 60\,\text{GeV}$ for online sample.

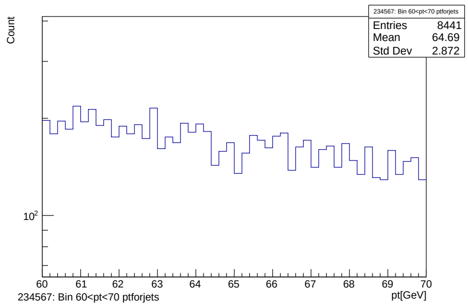

(c) p_T distribution of bin $60\,\text{GeV} < p_T < 70\,\text{GeV}$ for online sample.

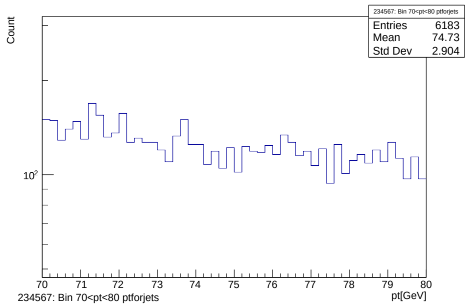

(d) p_T distribution of bin $70\,\text{GeV} < p_T < 80\,\text{GeV}$ for online sample.

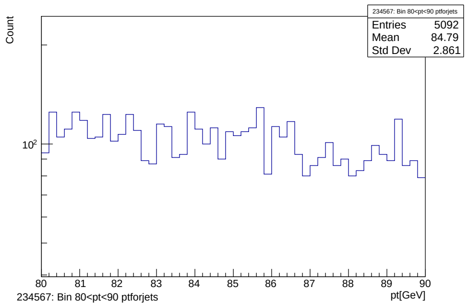

(a) p_T distribution of bin $80\,\text{GeV} < p_T < 90\,\text{GeV}$ for online sample.

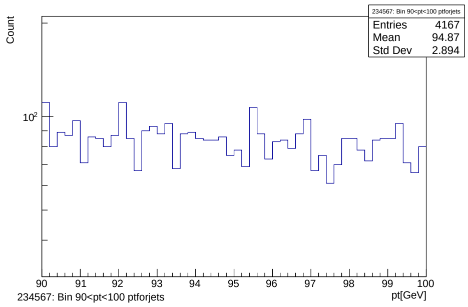

(b) p_T distribution of bin $90\,\text{GeV} < p_T < 100\,\text{GeV}$ for online sample.

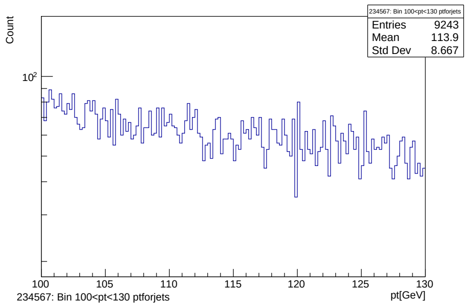

(c) p_T distribution of bin $100\,\text{GeV} < p_T < 130\,\text{GeV}$ for online sample.

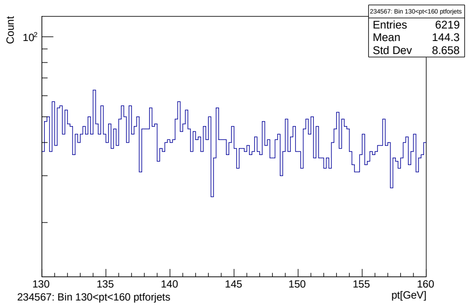

(d) p_T distribution of bin $130\,\text{GeV} < p_T < 160\,\text{GeV}$ for online sample.

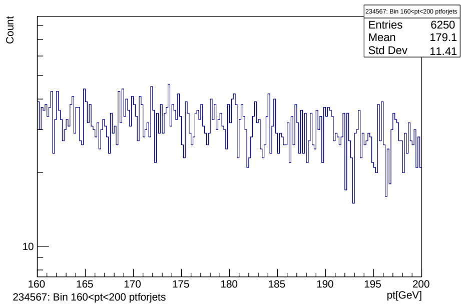

(e) p_T distribution of bin $160\,\text{GeV} < p_T < 200\,\text{GeV}$ for online sample.

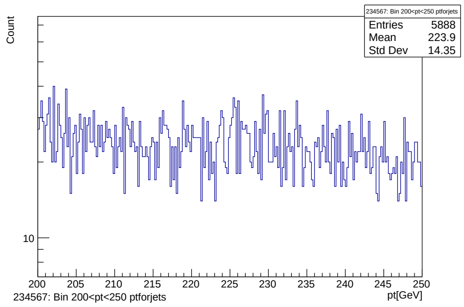

(f) p_T distribution of bin $200\,\text{GeV} < p_T < 250\,\text{GeV}$ for online sample.

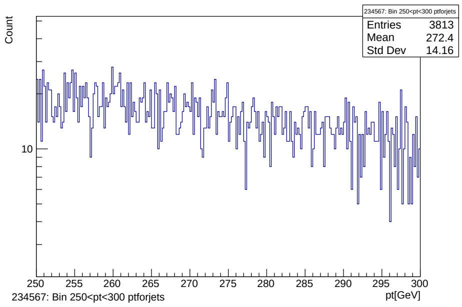

(a) p_T distribution of bin $250\,\mathrm{GeV} < p_T < 300\,\mathrm{GeV}$ for online sample.

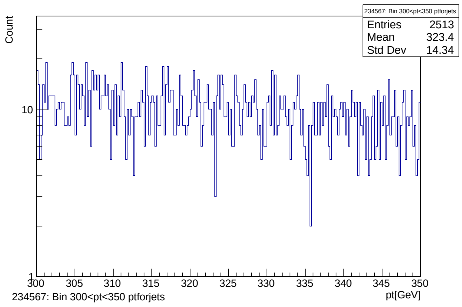

(b) p_T distribution of bin $300\,\mathrm{GeV} < p_T < 350\,\mathrm{GeV}$ for online sample.

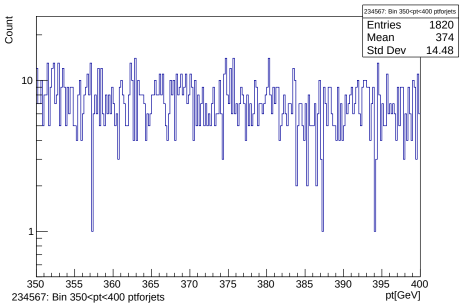

(c) p_T distribution of bin $350\,\mathrm{GeV} < p_T < 400\,\mathrm{GeV}$ for online sample.

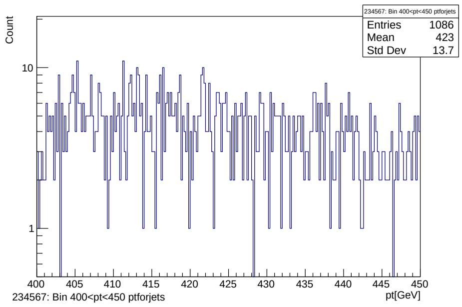

(d) p_T distribution of bin $400\,\mathrm{GeV} < p_T < 450\,\mathrm{GeV}$ for online sample.

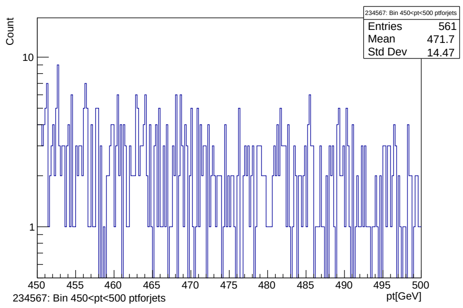

(e) p_T distribution of bin $450\,\mathrm{GeV} < p_T < 500\,\mathrm{GeV}$ for online sample.

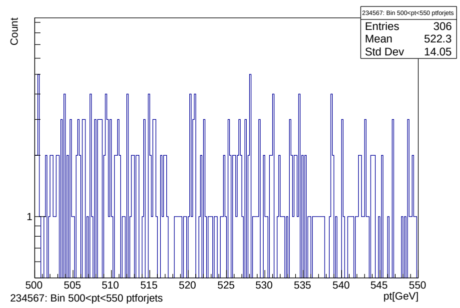

(f) p_T distribution of bin $500\,\mathrm{GeV} < p_T < 550\,\mathrm{GeV}$ for online sample.

B.2. Evaluation of selection rule performances

B.2.1. Selection efficiencies for Monte Carlo samples

Dijet sample

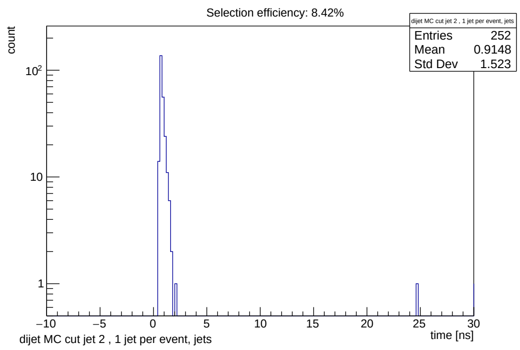

(a) Performance of selection rule with one jet of significance 2.

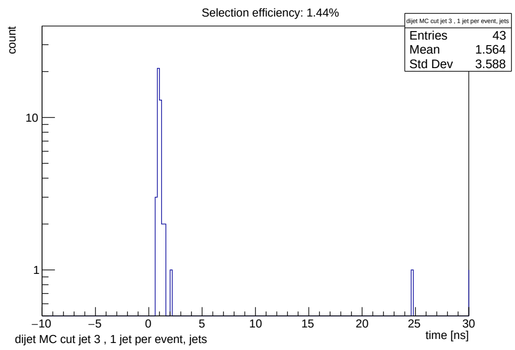

(b) Performance of selection rule with one jet of significance 3.

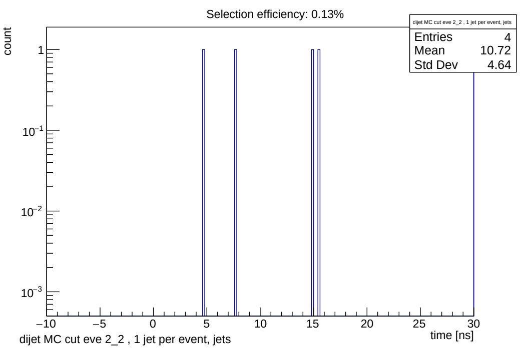

(c) Performance of selection rule with two jets of significance 2.

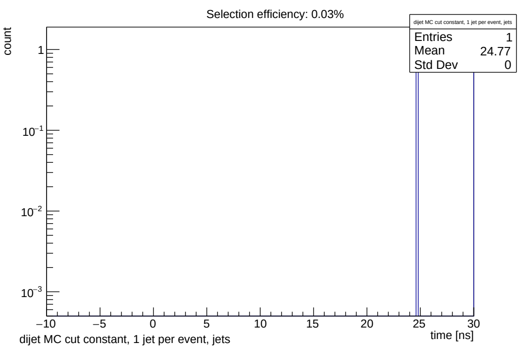

(d) Performance of selection rule with one jet with $p_T > 100\,\mathrm{GeV}$ and $t_{jet} > 3\,\mathrm{ns}$.

Figure B.19.: Dijet data. Each Plot shows the most significant jet per event. All not shown selection rules have no events passing.

LLP $0.01\,\mathrm{ns}$ sample

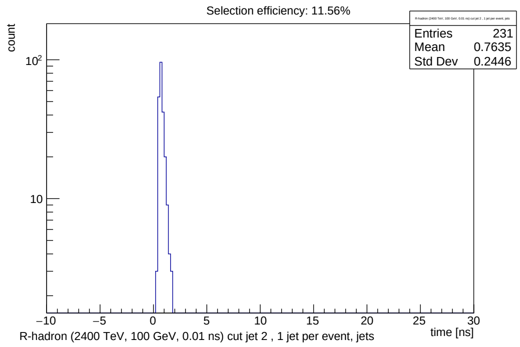

(a) Performance of selection rule with one jet of significance 2.

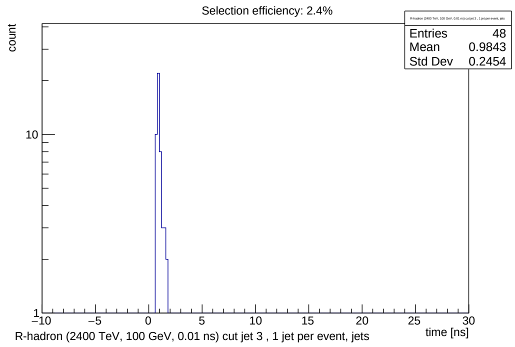

(b) Performance of selection rule with one jet of significance 3.

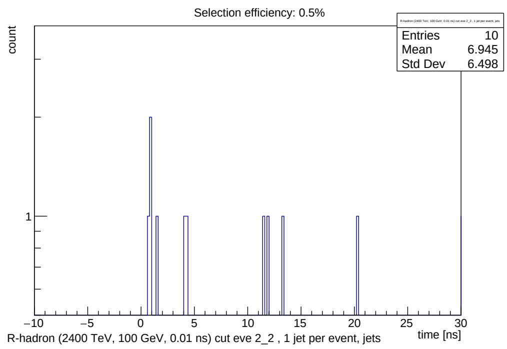

(c) Performance of selection rule with two jets of significance 2.

Figure B.20.: LLP $0.01\,\mathrm{ns}$ data. Each Plot shows the most significant jet per event. All not shown selection rules have no events passing.

LLP $3\,\mathrm{ns}$ sample

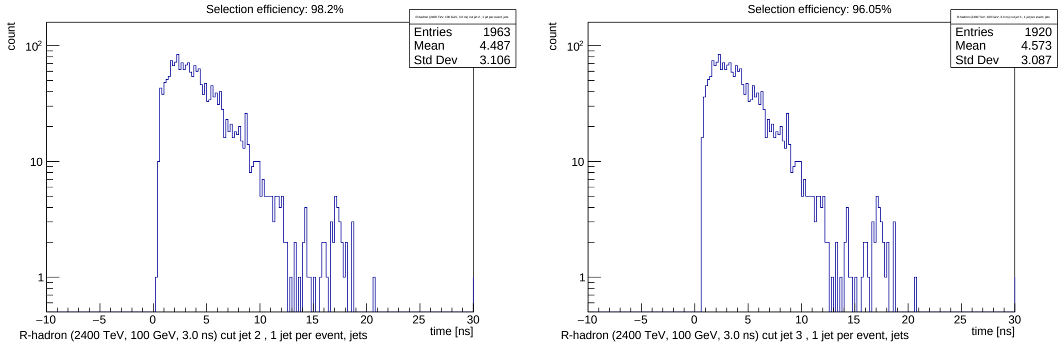

(a) Performance of selection rule with one jet of significance 2.

(b) Performance of selection rule with one jet of significance 3.

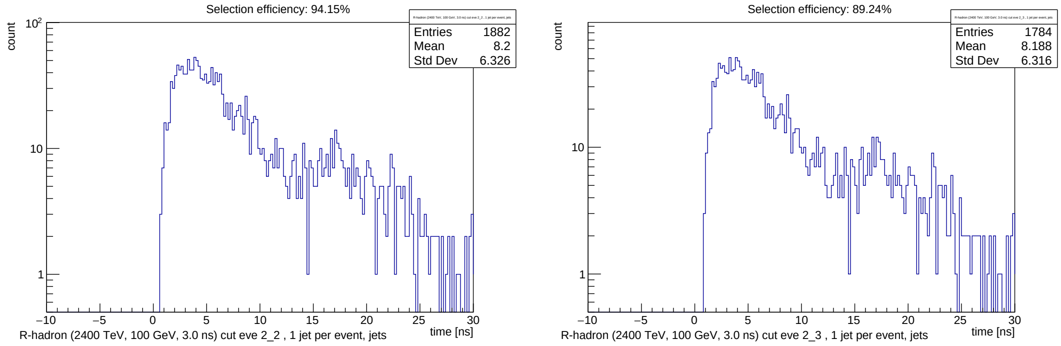

(c) Performance of selection rule with two jets of significance 2.

(d) Performance of selection rule with two jets of significance 3.

Figure B.21.: LLP $3\,\mathrm{ns}$ data. Each Plot shows the most significant jet per event.

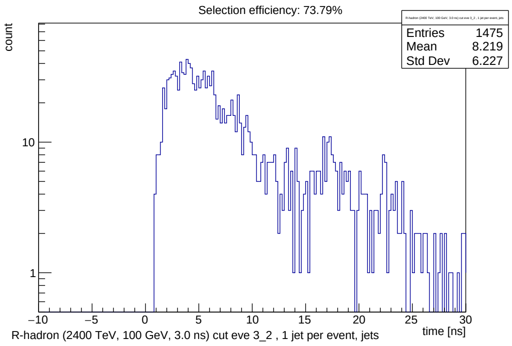

(a) Performance of selection rule with three jets of significance 3.

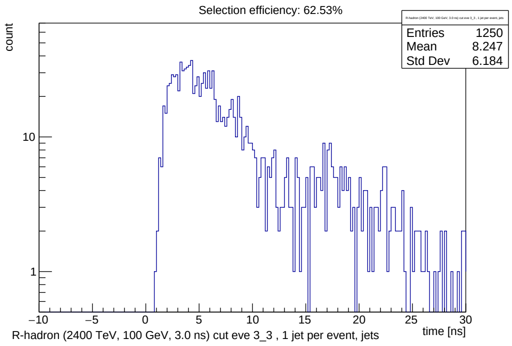

(b) Performance of selection rule with three jet of significance 3.

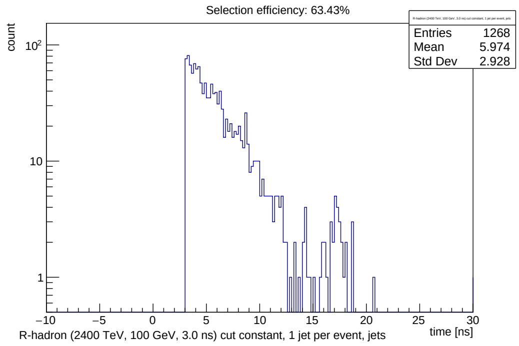

(c) Performance of selection rule with one jet with $p_T > 100\,\mathrm{GeV}$ and $t_{jet} > 3\,\mathrm{ns}$.

Figure B.22.: LLP $3\,\mathrm{ns}$ data. Each Plot shows the most significant jet per event.

LLP $10\,\mathrm{ns}$ sample

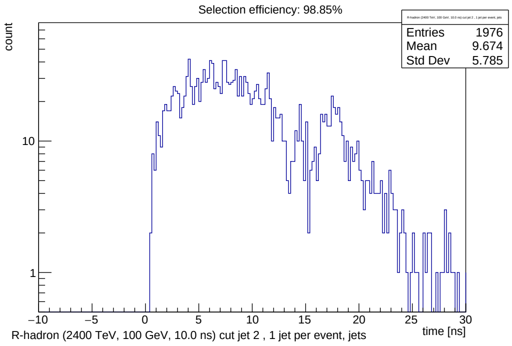

(a) Performance of selection rule with one jet of significance 2.

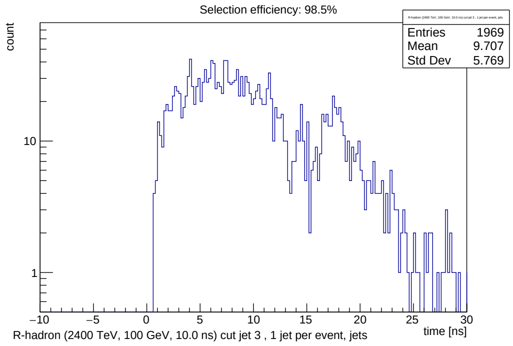

(b) Performance of selection rule with one jet of significance 3.

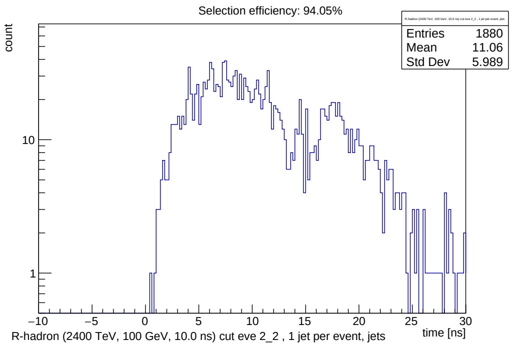

(c) Performance of selection rule with two jets of significance 2.

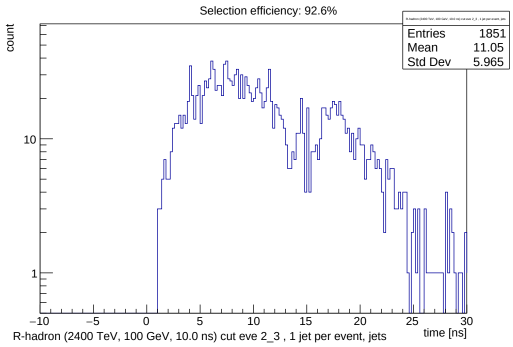

(d) Performance of selection rule with two jets of significance 3.

Figure B.23.: LLP $10\,\mathrm{ns}$ data. Each Plot shows the most significant jet per event.

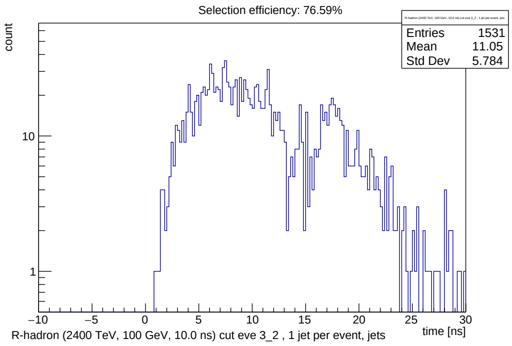

(a) Performance of selection rule with three jets of significance 3.

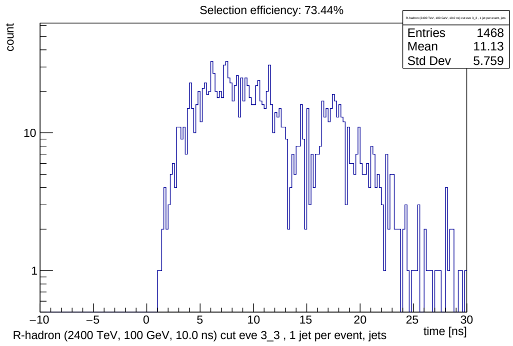

(b) Performance of selection rule with three jet of significance 3.

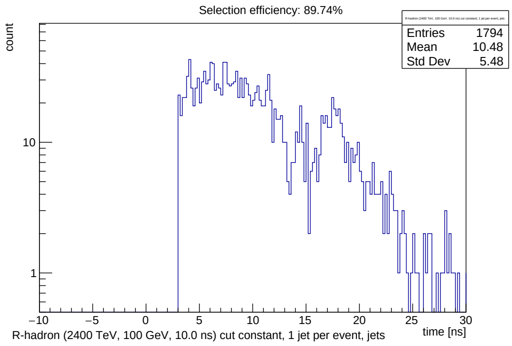

(c) Performance of selection rule with one jet with $p_T > 100\,\mathrm{GeV}$ and $t_{jet} > 3\,\mathrm{ns}$.

Figure B.24.: LLP $10\,\mathrm{ns}$ data. Each Plot shows the most significant jet per event.

LLP $30\,\mathrm{ns}$ sample

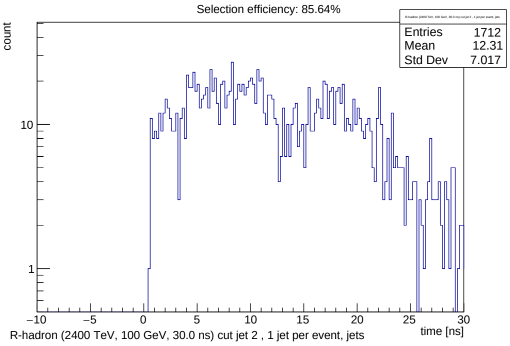

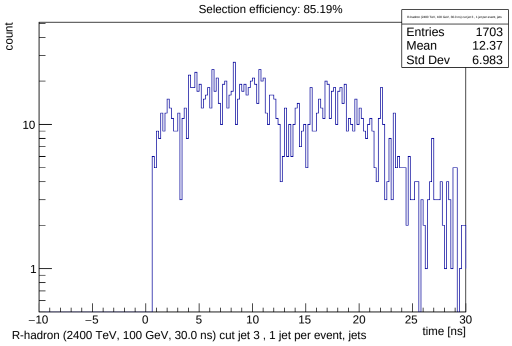

(a) Performance of selection rule with one jet of significance 2.

(b) Performance of selection rule with one jet of significance 3.

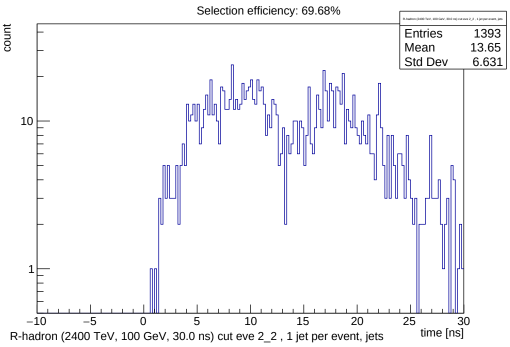

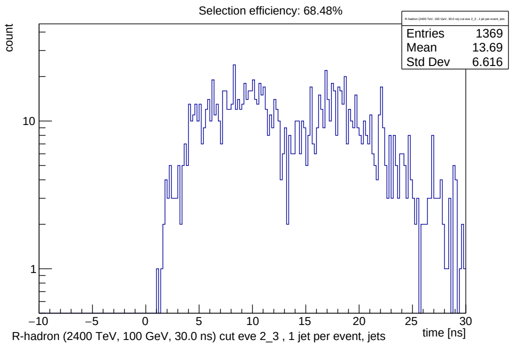

(c) Performance of selection rule with two jets of significance 2.

(d) Performance of selection rule with two jets of significance 3.

Figure B.25.: LLP $30\,\mathrm{ns}$ data. Each Plot shows the most significant jet per event.

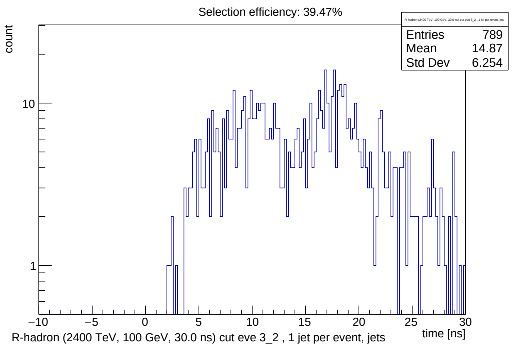

(a) Performance of selection rule with three jets of significance 3.

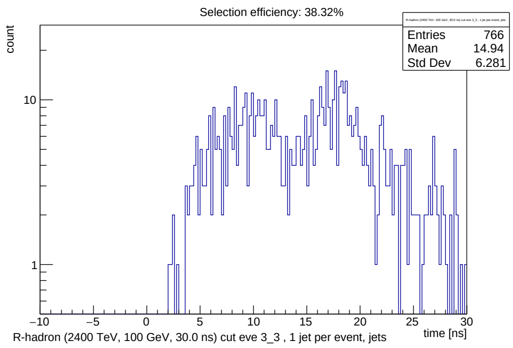

(b) Performance of selection rule with three jet of significance 3.

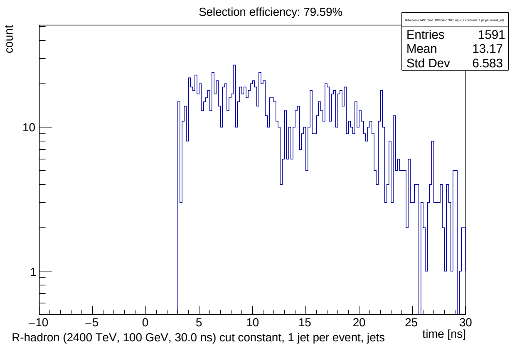

(c) Performance of selection rule with one jet with $p_T > 100\,\mathrm{GeV}$ and $t_{jet} > 3\,\mathrm{ns}$.

Figure B.26.: LLP $30\,\mathrm{ns}$ data. Each Plot shows the most significant jet per event.

B.2.2. Selection efficiencies for measured and offline reconstructed sample

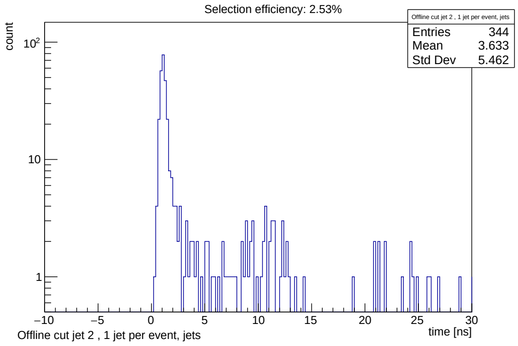

(a) Performance of selection rule with one jet of significance 2.

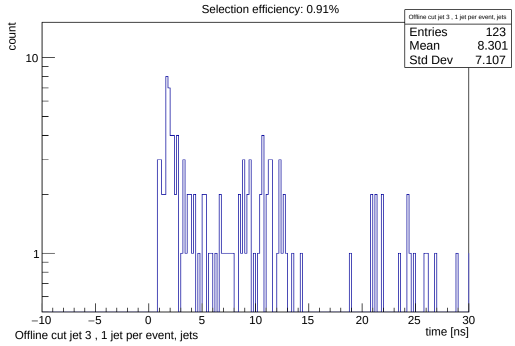

(b) Performance of selection rule with one jet of significance 3.

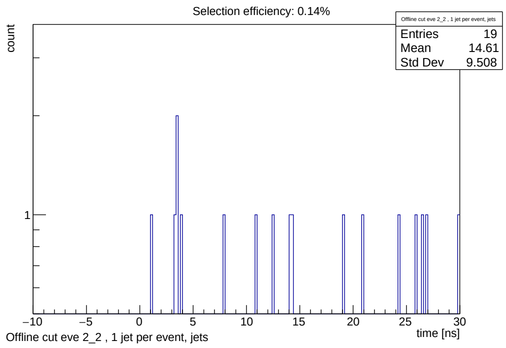

(c) Performance of selection rule with two jets of significance 2.

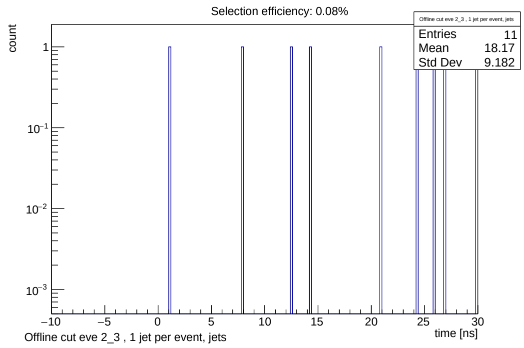

(d) Performance of selection rule with two jets of significance 3.

Figure B.27.: Measured and offline reconstructed data. Each Plot shows the most significant jet per event.

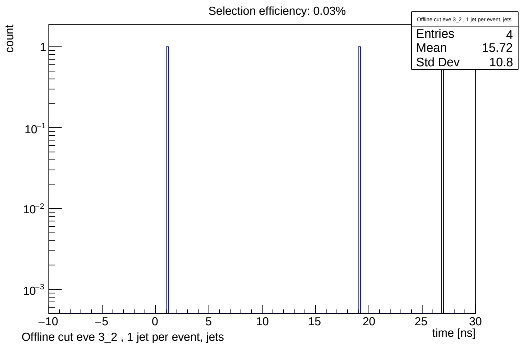

(a) Performance of selection rule with three jets of significance 3.

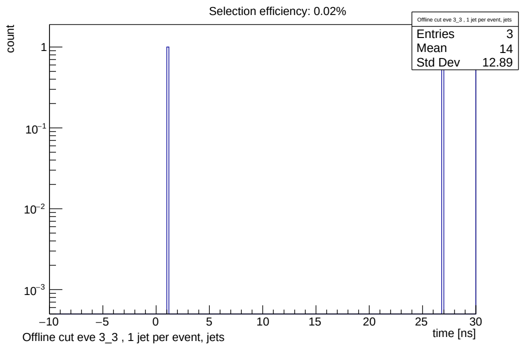

(b) Performance of selection rule with three jet of significance 3.

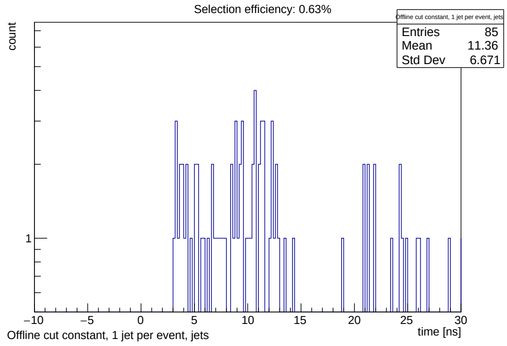

(c) Performance of selection rule with one jet with $p_T > 100\,\text{GeV}$ and $t_{jet} > 3\,\text{ns}$.

Figure B.28.: Measured and offline reconstructed data. Each Plot shows the most significant jet per event.

B.2.3. Selection efficiencies for measured and online reconstructed sample

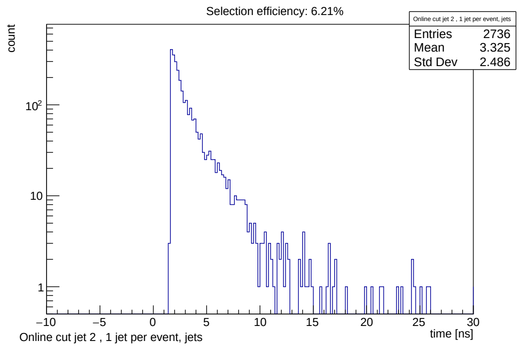

(a) Performance of selection rule with one jet of significance 2.

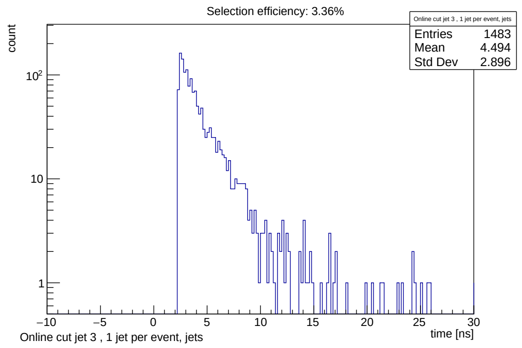

(b) Performance of selection rule with one jet of significance 3.

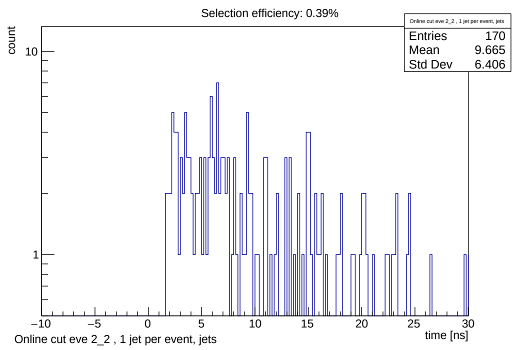

(c) Performance of selection rule with two jets of significance 2.

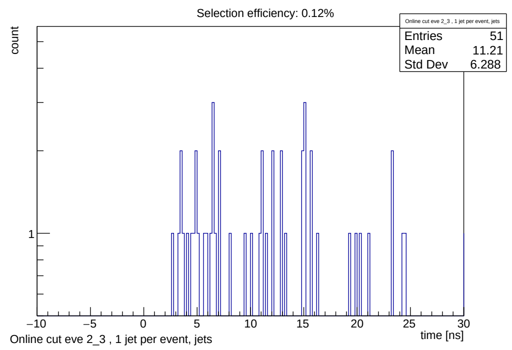

(d) Performance of selection rule with two jets of significance 3.

Figure B.29.: Measured and online reconstructed data. Each Plot shows the most significant jet per event.

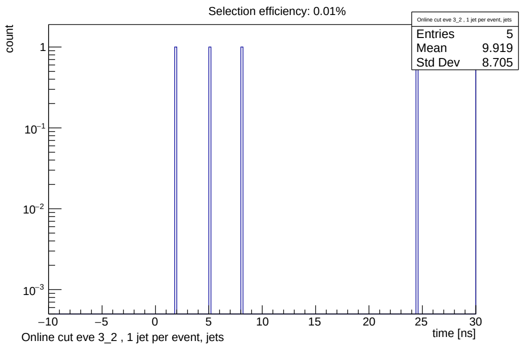

(a) Performance of selection rule with three jets of significance 3.

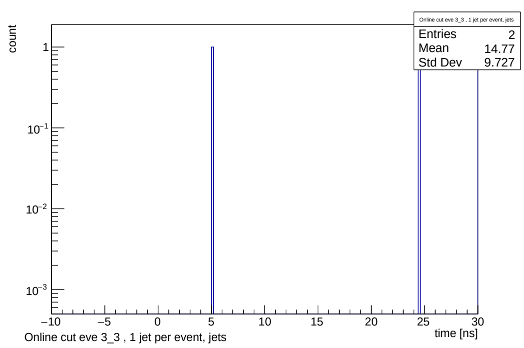

(b) Performance of selection rule with three jet of significance 3.

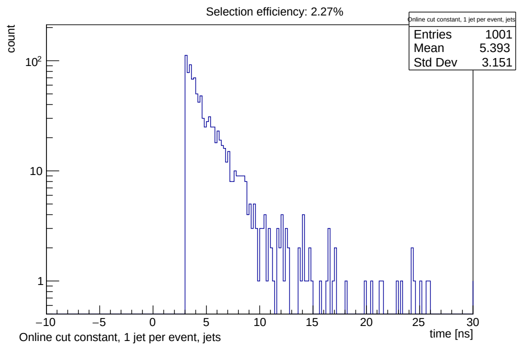

(c) Performance of selection rule with one jet with $p_T > 100\,\mathrm{GeV}$ and $t_{jet} > 3\,\mathrm{ns}$.

Figure B.30.: Measured and online reconstructed data. Each Plot shows the most significant jet per event.